Variable Hydraulic Transmissions for Passive Wearable Robots

A DISSERTATION
SUBMITTED TO THE FACULTY OF THE GRADUATE SCHOOL
OF THE UNIVERSITY OF MINNESOTA
BY

Saeed Hashemi

IN PARTIAL FULFILLMENT OF THE REQUIREMENTS
FOR THE DEGREE OF
DOCTOR OF PHILOSOPHY

William K. Durfee

July, 2021

Acknowledgements

First of all, I would like to thank my PhD advisor, Professor William Durfee, for the continuous support and guidance during my education at the University of Minnesota. I am grateful for the opportunity of working on multiple research projects at the Human/Machine Design Lab while learning technical skills every day. I would also like to thank my thesis committee, Professor James Van de Ven, Professor Tim Kowalewski, and Professor Andrew Hansen for their insightful comments and mentorship.

I would like to thank current and former Human/Machine Design Lab members, including Jonathan Nath, Yusra Ullah, Jeff Bies, and Toby Pan. I would also like to acknowledge the work of Andrew Kivi and Kimberly Gustafson during the projects. I want to thank Disney Research for the internship opportunity, the results of which are reported in Chapter 6.

This work was supported by the National Institutes of Health, grant number 5-R01EB019834-03. I also had the opportunity to receive the Mechanical Engineering Departmental Fellowship from 2014-2015, providing additional financial support for my graduate education.

I would like to thank my family, my parents, brothers, sisters, and friends for their unconditional love and support throughout my Ph.D. journey. Finally, I would like to thank my love, my fiance, Bita, who was always supportive, protective, and encouraging over these years and has been by my side throughout this path.

Abstract

Wearable robots are used to assist or perform human-like motions. A teleoperated robot is used to transmit the motion from a specific point to another. Teleportation can be delivered through a passive or active system. Body-powered wearable robots (BPWRs) use passive teleoperated manipulation to transmit the power between different limbs where the power transmission between limbs needs to be at the top speed and force efficiency. Rehabilitation is one of the applications of BPWRs since they promise a portable, low-power, and safe interface. The active rehabilitation robots suffer from poor patient engagement due to motor slacking, where the user relies mostly on the motor to accomplish the task. BPWR is a passive alternative to let the users feel more active by using their own bodies to power the system. BPWR can also be used for surgical, performance amplifying, and puppeteering purposes.

Hydraulics is a viable choice for wearable robots due to its high stiffness, light weight, and capability of having a variable transmission ratio. Hydraulic components usually operate inefficiently at low pressures due to viscous losses. Due to the safety concerns, low-pressure hydraulics is preferable in applications where the device has interaction with the human body. Efficient components and analytical models to describe their performance are needed to be incorporated in these systems.

In this work, I present highly efficient and consistent components to be used in a wearable device. Furthermore, I propose analytical models to facilitate a better understanding of the components. A variable hydraulic transmission design is presented to provide a high number of unique transmission ratios. The valves in the system set a configuration in actuators' connectivity and vary the transmission ratio between joints. The proposed design requires low energy to switch the transmission ratios in a compact and wearable embodiment. I introduce a model for losses across the transmission to allow system-level understanding of the system. A superposition of mechanical and hydraulic losses is used to find the loss in the system with a hydraulic analogy. Models described in this work are validated with experimental tests.

Soft robots are embodied to an antagonist transmission due to their conformity. A novel bone-inspired bending soft robot is introduced to be used in a teleoperated

antagonist transmission setup. Higher stiffness and natural frequency are achieved in the bone-inspired bending soft robots compared to traditional bending soft robots. I propose experimentally validated dynamic and geometrical models to understand the stiffness and natural frequency of the bending soft robots and to predict the robot's motion trajectory.

Contents

List of Tables

List of Figures

Chapter 1

Applications, Research Objectives, Prior Art

1.1 Introduction and Applications

Wearable robots assist individuals in making human-like movements. A body-powered wearable robot (BPWR) is a passive system in which an exoskeleton transmits the power of one or multiple body segments to other segments (Figure 1.1). The efficiency of the transmission needs to be maximized for BPWR. BPWR is targeted for performance increasing, surgical instruments, puppeteering devices, and rehabilitative applications. In a passive setup, the external energy depicted in Figure 1.1 is to supply power to electrical components like sensors. The concept of a body-powered wearable robot on the body for rehabilitation purposes is depicted in Figure 1.2.

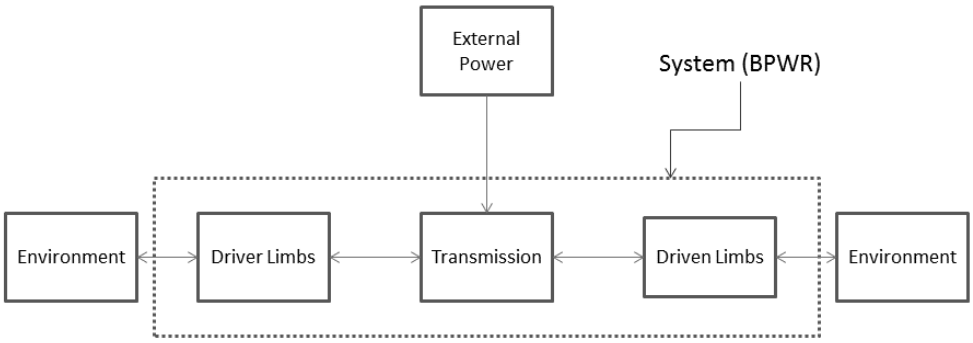

Figure 1.1: A body-powered wearable robot block schematic.

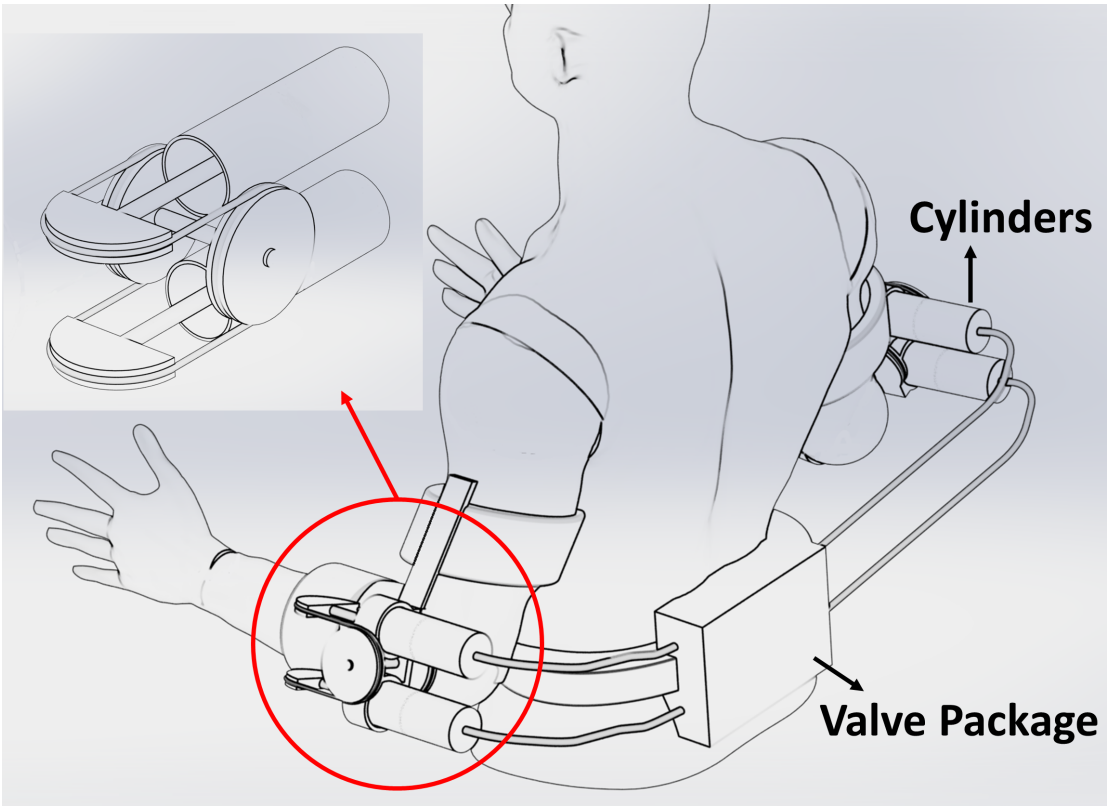

Figure 1.2: A body-powered wearable robot concept.

The human-robot interaction can be handled by an external force or an internal force system. In an external force system, the exoskeleton moves the human body and

the power transmission is between the limb, exoskeleton, and the environment (Figure 1.3 left). In an internal force system, body segment power is transmitted to the other segments by the exoskeleton (Figure 1.3 right). Power transmission is between the limbs and the exoskeleton in the internal force systems [7]. BPWR robots work on the internal force principle.

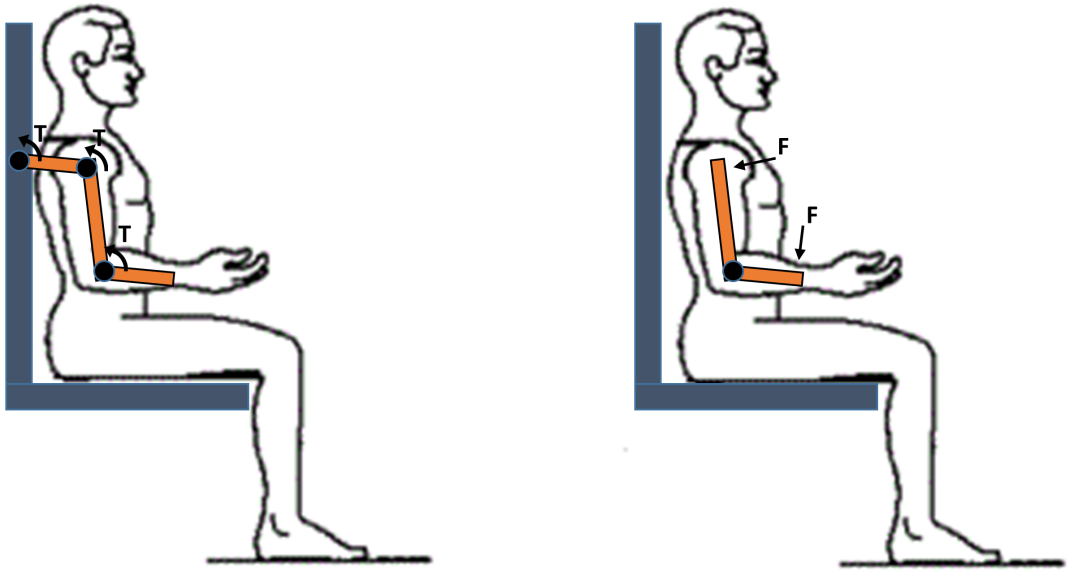

Figure 1.3: Schematic representation of external force (left) and internal force (right) exoskeletal systems.

1.2 Research Objectives

The objectives of this thesis were to:

1- Demonstrate through analytical modeling that variable hydraulic transmissions are sufficiently efficient to be used in a BPWR application.

2- Validate the results of objective 1 by experimental measurements in a testbed.

3- Demonstrate that a BPWR with a hydraulic transmission that contains soft robots is efficient enough for purposes required conformity.

For objective 1, I used hydraulic principles to mathematically model hydraulic components and hydraulic circuits to evaluate the variable hydraulic transmission for

BPWR.

For objective 2, I designed and built a benchtop hydraulic testbed with a hydraulic transmission connected to two lever arms as input and output. The hydraulic transmission was capable of providing 14 unique transmission ratios. I developed a new type of long-stroke rolling diaphragm (LSRD) cylinder that showed promise for this application. A digital valve with low pressure drop, low power consumption, high response time, and lightweight was designed to be used in this testbed.

For objective 3, I evaluated a passive hydraulic and pneumatic transmission with bending soft robots. Natural frequency, stiffness, and trajectory planning of the transmission were modeled and verified through experimental setups.

1.3 Prior Art

Wearable robots may operate alongside limbs, categorized as exoskeletons and orthoses, or as substitutes for missing limbs that are categorized as prostheses [7]. There is a power transmission between the exoskeleton and body in wearable robots.

Some examples of wearable robots are shown in Figure (1.4). Sankai and his team developed (HAL)-5, an exoskeleton concept aimed at both performance increasing and rehabilitative purposes [8, 9]. The flexion-extension in each joint was powered by a DC motor placed at the joint [10] (Figure 1.4 middle). Hydraulics power-to-weight density advantage was used in the Hydraulic Ankle-Foot Orthosis at University of Minnesota [3]. With the power supply worn at the waist and the hydraulic cylinders at the ankles, high force was being transmitted to the ankles to allow a smooth walking cycle (Figure 1.4 right) [11]. One of the earliest BPWR was discribed in a U.S. patent granted in 1890 to Yagn (Figure 1.4 left) [1]. Two long bow springs were used to operate in parallel to the legs to enhance running and jumping [10].

Figure 1.4: Some examples of wearable robots; Yagn's running aid (left) (Image from [1]), HAL-5 exoskeleton (middle) (Image from [2], and hydraulic ankle-foot orthosis (right) (Image from [3])

Body-powered exoskeletons were used in different upper and lower limb rehabilitation applications [12, 13]. Bowden cables were used in an upper limb body-powered robot for people with limited power in arms [14, 15] (Figure 1.5a). Soft McKibben muscles were used in an upper limb rehabilitation robot to increase conformity [16] (Figure 1.5b).

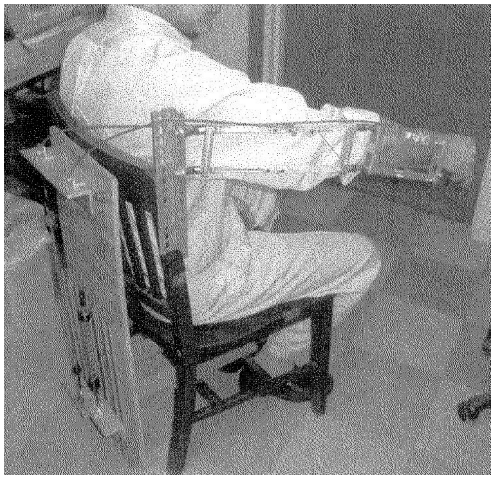

(a) Image from [14].

(b) Image from [16].

Figure 1.5: Some examples of upper-limb wearable robots. (a) body-powered robot using Bowden cables to transmit power. (b) A wearable robot using soft robotic McKibben muscles.

The body-powered rehabilitation devices and externally powered ones were evaluated in multiple studies [17, 18, 19]. In one study, the subjects had higher muscle activation levels in a body-powered device than an externally powered robot due to reduced motor slacking . Motor slacking happens when the human motor system reduces the activation level, and in this case, the human motor system relies on the external power [20]. Passive servo brakes were evaluated in a passive human-robot interaction setup for rehabilitation [21].

Hydraulic transmission is a viable choice for wearable robots because of its high stiffness, lightweight, capability of having a variable transmission ratio, and the fact that the power can be transmitted through small and flexible conduits. A variable transmission enables the system to have a wide range of speed or flowrate and to operate close to the peak power and efficiency.

Several actuation types have been used in wearable robots, from hydraulics to electrical [22, 23]. The current actuation modes in rehabilitation robots are hydraulics, pneumatics, motor, and SEA (series elastic actuator) . Linear and rotary hydraulic actuators have been used on joints in multiple exoskeletons [24, 25, 26]. Rotary hydraulic

actuators with higher leakage and friction compared to the linear actuators were used in a wearable robot [2, 27, 28].

Hydraulic actuation with an electrical hydraulic power supply was used in BLEEX exoskeleton (Figure 1.6) to support up to 75 Kg of load with a walking speed of 0.9 m/s [4, 29, 30].

Figure 1.6: Design of the BLEEX exoskeleton. Image from [4].

Antagonist passive leader-follower transmissions have been used in needle insertion in MRI-compatible devices [31, 32]. Active actuation (hydraulic or electric) requires a motor or pump, and force and position sensors for haptic feedback to the user [33, 34, 35]. In this case timely techniques are required for real-time position tracking [36]. Another active pneumatic actuation with long transmission lines was used for needle driving [37]. Another study compared hydrodynamic and pneumatic actuation in MRI-compatible teleoperated robots and found smoother movement and better position control with hydrodynamic actuation [38]. High efficiency actuators like rolling diaphragm hydraulic

cylinders were proposed to increase the haptic feedback [39, 36]. A low-friction passive hydrostatic transmission equipped with rolling diaphragm cylinders had high bandwidth (>300 Hz) and forces as low as 0.1 N were detectable through the transmission [40, 41].

Teleoperated robots can also be used in human-robot interaction [42, 43]. The passive and active mechanisms were used for that purpose. A parallel rigid mechanism to provide a leader-follower movement was suggested in a study [44]. A low-friction hydraulic transmission with rolling diaphragm cylinders was used to statically balance a serial robot with remote counterweights [45]. An antagonist hybrid transmission was used in a teleoperated robot for human-robot interaction through puppeteering [5] (Figure 1.7). Furthermore, the biological similarities of the soft robots and their conformity, compliance, and safety make them a viable option to be used in human-robot interaction [46].

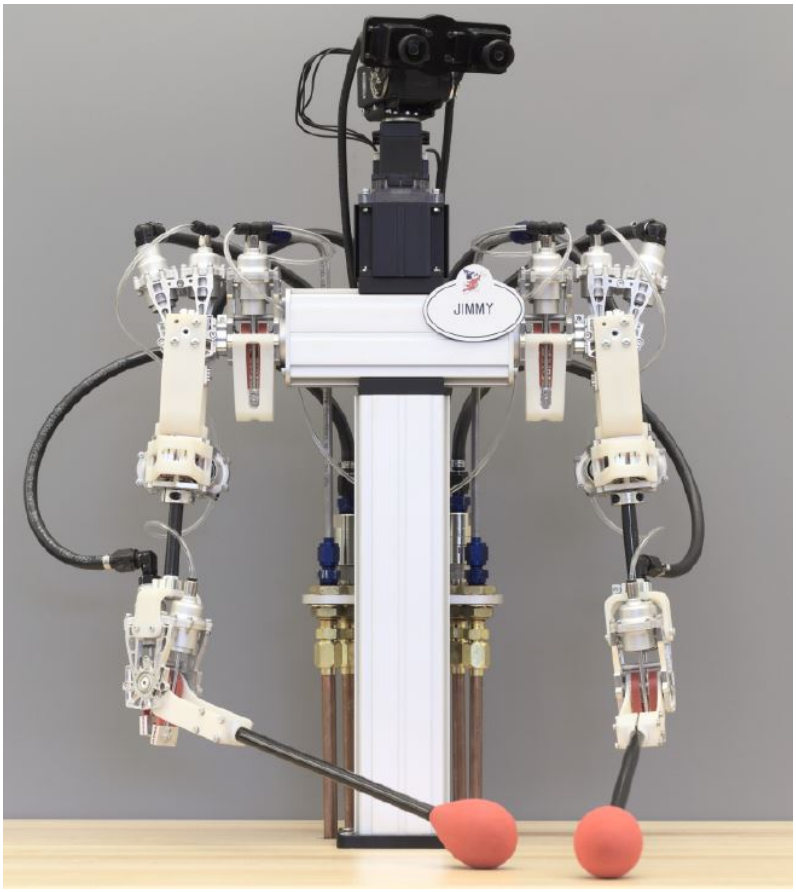

Figure 1.7: A haptic teleoperated robot using a low-friction hybrid transmission. Image from [5]

Chapter 2

Properties of Small-Scale Hydraulic Components

2.1 Hydraulic Actuator

2.1.1 Introduction

Portions of this chapter were published in Hashemi and Durfee, Low friction, long-stroke rolling diaphragm cylinder for passive hydraulic rehabilitation robots. In Frontiers in Biomedical Devices (Vol. 40672, p. V001T05A016). American Society of Mechanical Engineers. April 2017, Hashemi and Durfee. U.S. Patent Application No. 16/551,330. 2020, and Hashemi, Mitchell, and Durfee. Experimentally Validated Models for Switching Energy of Low Pressure Drop Digital Valves for Lightweight Portable Hydraulic Robots. In Fluid Power Systems Technology (Vol. 59339, p. V001T01A023). American Society of Mechanical Engineers. October 2019.

Hydraulic fluid power systems are known for their high power density. Hydraulic actuators are commonly used in mechanical systems, and actuator efficiency is one of the most significant factors in these systems [47]. Hydraulic actuators have high stiffness and small position error. A hydraulic cylinder converts hydraulic power to mechanical power and is the most common actuator for hydraulic systems. Friction and leakage of the cylinders are the most important factors in determining force and volume efficiencies of hydraulic systems. Efficient cylinders designed for low-pressure hydraulics are being

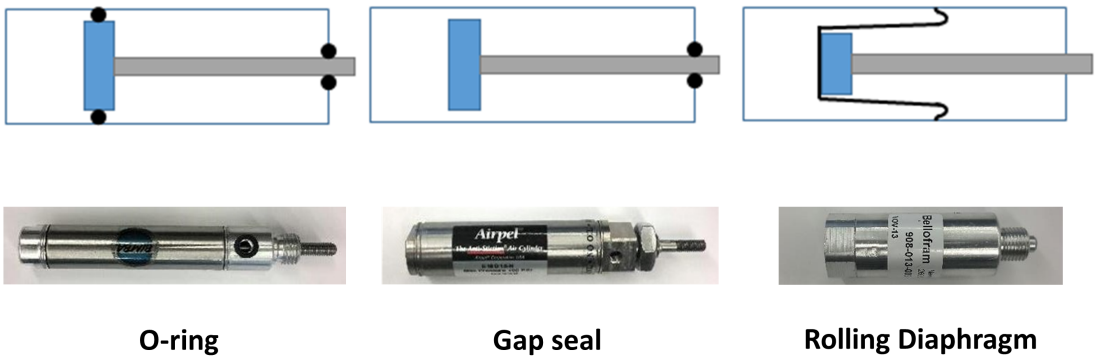

Figure 2.1: Three common cylinder types a) O-ring b) gap seal c) rolling diaphragm.

utilized in various applications, from rehabilitation robotics [48, 49] and puppeteering [50] to remote MRI needle insertion [41].

Wearable rehabilitation robotics is one of the hydraulic actuators applications. In our variable hydraulic transmission, hydraulic cylinders deliver the power extracted from the driver joint to the driven joint (Figure 1.2).

O-ring seal, rolling diaphragm, and gap seal cylinders are three technologies that have been used in hydraulic systems. O-ring cylinders use an O-ring seal between the piston and cylinder. Rolling diaphragm actuators have a diaphragm between the cylinder and piston, which rolls back and forth (Figure 2.2). In gap seal cylinders, there is a tiny gap between the piston and cylinder. There is a trade-off between leakage and friction in these cylinders. Therefore, leakage between the two chambers is tolerated to reduce friction (Figure 2.1).

One study examined low-friction cylinders in a low-pressure hydraulic transmission [50]. In this study, rolling diaphragm cylinders were used in the transmission; however, the restriction on the stroke length of these cylinders was a problem that needed to be solved. Commercial rolling diaphragms are manufactured using compression molding of a sheet rubber and woven fabric [50]. A manufacturing method that limits the stroke length to no more than the bore of the cylinder. Rolling diaphragm cylinders with higher stroke-to-bore ratios can multiply the work per cycle of the system [50]. Furthermore, there are limitations of using short-stroke rolling diaphragm cylinders [51, 45]. A manufacturing method for long-stroke rolling diaphragm cylinders was described

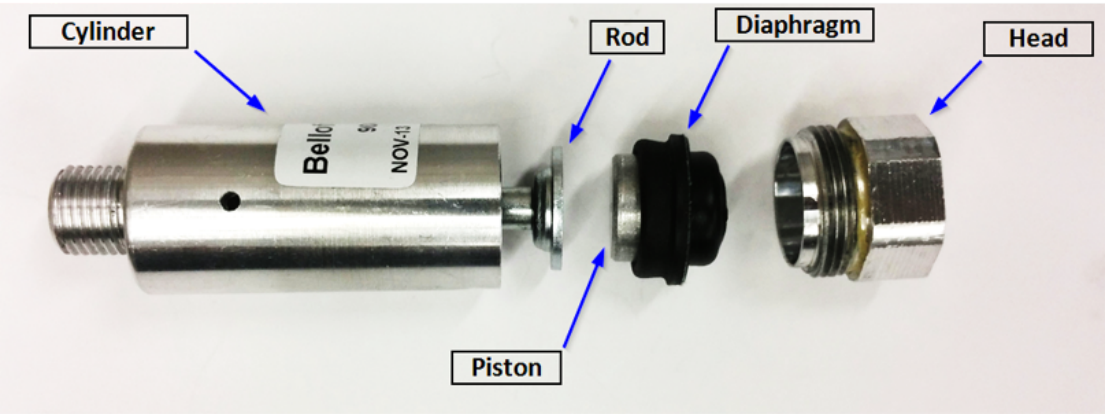

Figure 2.2: Rolling diaphragm cylinder exploded view.

in previous studies, which had a silicone molding process to build a diaphragm in any geometry [52]. In this method, the burst pressure of the diaphragm was 240 kPa (35 psi). Developing low friction, leakage-free cylinder with high pressure capabilities and without stroke limitations is needed for small hydraulics. A more thorough friction evaluation of various cylinder types is needed to determine which technology has the lowest friction and is the most appropriate for low-pressure hydraulic systems like rehabilitation robots.

In this chapter, the manufacturing process of making the long-stroke rolling diaphragm cylinder is described. Using an experimental test, we measured the resistance forces in three types of cylinders: O-ring, gap seal, and rolling diaphragm. The cylinders were tested at low pressure (up to 690 kPa (100 psi)) and with mineral oil to determine the cylinder with the lowest friction. The same friction test was performed in a novel, long-stroke, rolling diaphragm cylinder (LSRD) to compare it in two different thicknesses with commercial cylinders.

The effective area of the rolling diaphragm cylinders was reported to be an average of the piston and cylinder area [53]. In the tapered rolling diaphragm cylinder, the effective area decreases with the stroke due to the tapered shape of the diaphragm (Figure 2.3). Higher stroke length in long-stroke rolling diaphragms makes this phenomenon more dramatic. The variance in the effective area causes the cylinder performance to be dependent on the piston's position. This chapter describes a cylinder design method that minimizes the change in force with piston position.

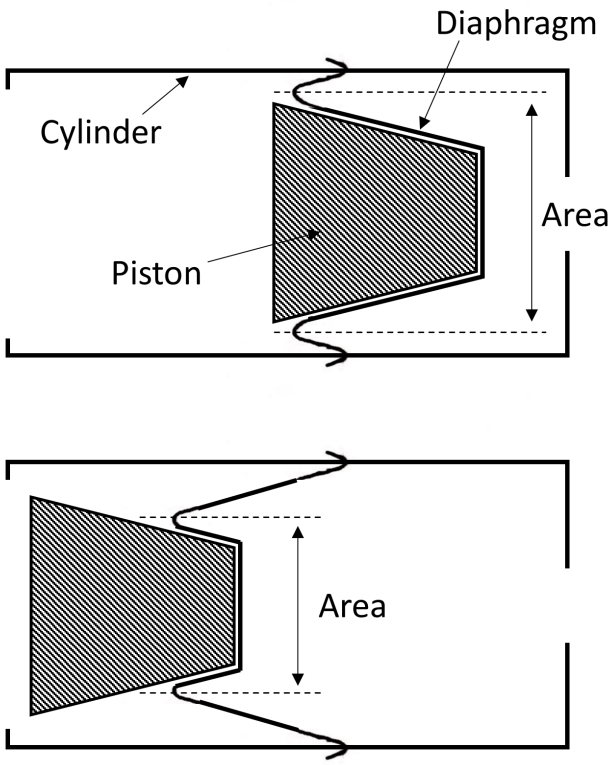

Figure 2.3: Effective area changes with piston position.

2.1.2 Method

Fabrication of the Long-Stroke Rolling Diaphragm (LSRD) Cylinder

A new manufacturing method was used for the long-stroke rolling diaphragm (LSRD) that provides a high stroke length. (Figure 2.4). The mold has an outer geometry equal to the desired inner geometry of the diaphragm (Step 1). We used 3D printing to make the mold.

A sheet of polyurethane base material was wrapped tightly around the mold and kept in place using the tape (Step 2). An impulse heat sealer was used to melt the rubber sheet and form a seal (Step 3). A hot knife can also be used to melt the seal. A polytetrafluoroethylene (PTFE or Teflon) protective sheet was placed between the material and the heat source to protect the base material from excessive heat and provide a uniform heat application. After sealing the seam, the tape was removed, and

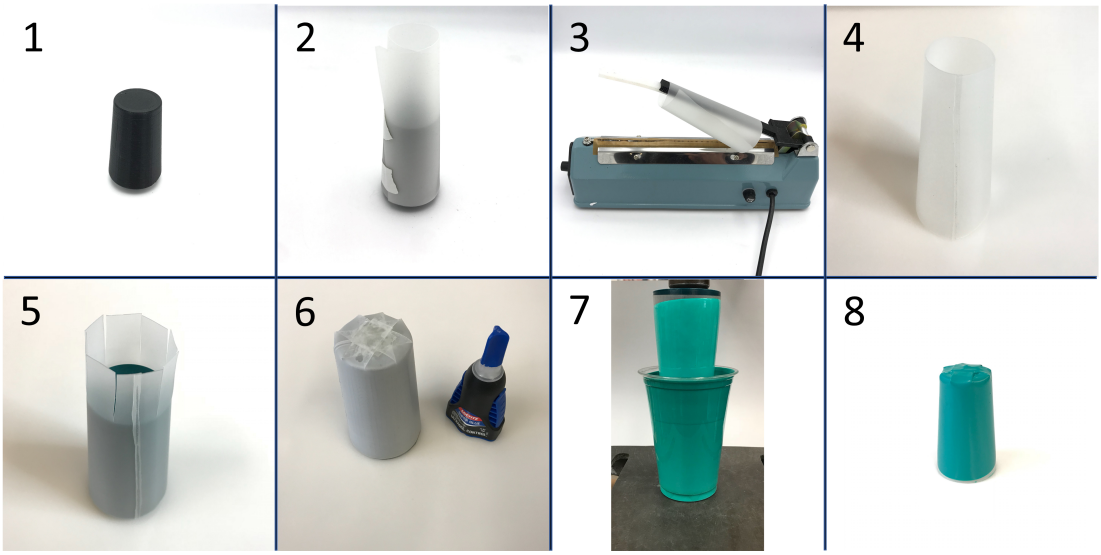

Figure 2.4: Long-stroke rolling diaphragm manufacturing method.

excess base material proximate to the seal was trimmed (Step 4). After these processes, the base material was in a cylindrical configuration having first and second ends. Cuts were formed on the first end of the base material, divided the first end into a plurality of flaps, folded toward a center axis of the cylindrically wrapped base material to form a closed first end (Step 5). Next, cyanoacrylate adhesive was applied to each of the plurality of flaps to secure them in an inwardly folded position (Step 6). In essence, the first end was closed off with the flaps. Afterward, the base material was deep coated in an elastomer, such as polychloroprene for using mineral oil or Plasti Dip for using water (Step 7). Plasti Dip and polychloroprene can be thinned with VM&P Naphtha and water, respectively. The elastomer coated material was left to be cured. In the case of using polychloroprene for mineral oil, the elastomer was cured in an oven at approximately 80 to 85 degrees F for 8 to 12 hours. Alternatively, when using the Plasti Dip for water, other curing methods such as air-drying may be used for an extended period (about 6 hours). Once the elastomer was cured, epoxy was poured into the diaphragm to seal the first end. The epoxy was left to dry for at least 24 hours. Finally, the diaphragm was ready to be placed into the cylinder body (Step 8).

To increase the stiffness and strength of the diaphragm, a fiber-reinforced tape with the thickness of 0.15 mm can be placed on the inside of the diaphragm between steps 6

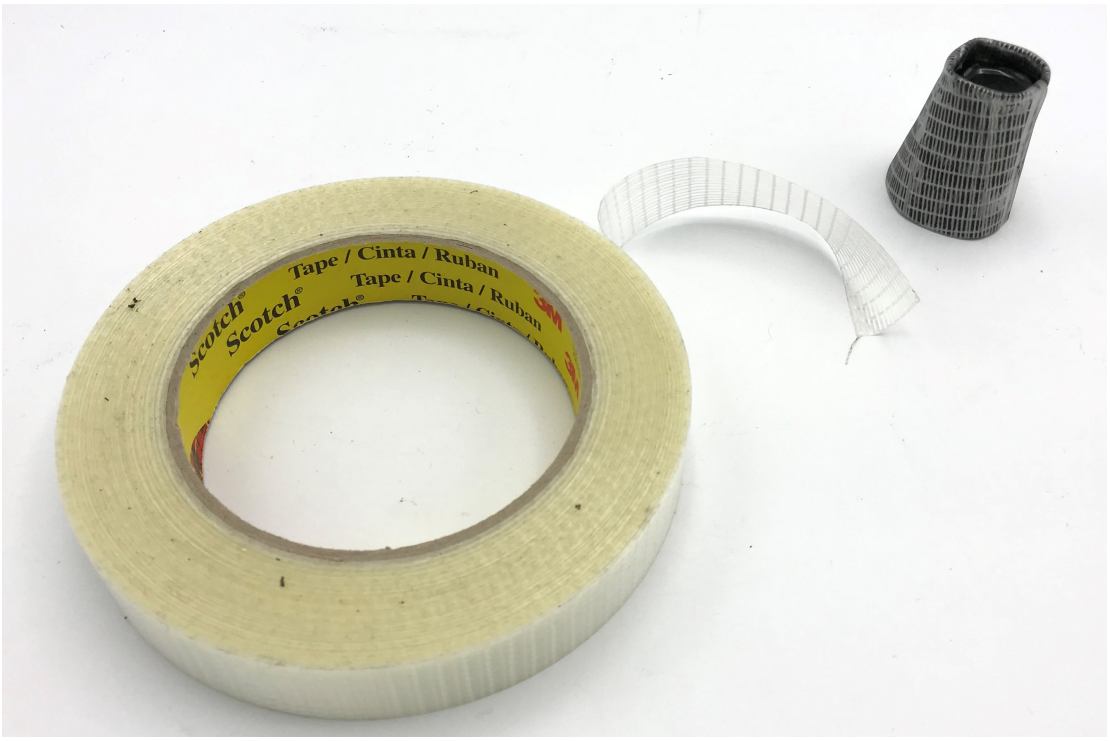

Figure 2.5: Fiber-reinforced long-stroke rolling diaphragm.

and 7 (Figure 2.5). This polypropylene plastic tape with fiberglass fibers ensured higher stiffness at the expense of higher friction in the rolling action.

In an alternate method, largely similar to that described above, the base material can be made of fabric and can be secured into a cylindrical configuration with fabric glue instead of heat sealing via the hot knife. Fabrics that work best are those that do not wrinkle easily. Cotton fabric is one suitable example. The method can be the same as that described above in all other respects. Two challenges with using fabric in this manufacturing method are a defective seal on fabric and the tendency of the fabric to wrinkle.

Two long-stroke rolling diaphragms were made for the friction test with the diaphragm thicknesses of 0.33 and 0.58 mm. The thickness of the elastomer controlled the variance in the thickness of the long-stroke rolling diaphragms. Each long-stroke rolling diaphragm that was tested for the friction had a 2:1 stroke-bore ratio.

A burst pressure limit test was performed on the LSRD by pumping fluid into the

cylinder while measuring the pressure until the diaphragm broke.

The LSRD cylinder design with the clear plastic tube and aluminum is illustrated in Figure 2.6. The diaphragm was clamped between two cylindrical tubes. A fitting cap with a gasket were on the fluid side, and a ring was on the unpressurized side. Four steel threaded rods were used to clamp the two caps, two tubes, and the diaphragm. For cylinder bore larger than 50 mm, eight clamping rods were used.

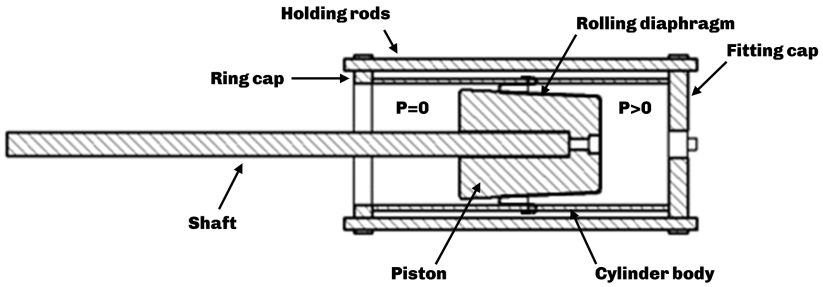

(a) LSRD cylinder design.

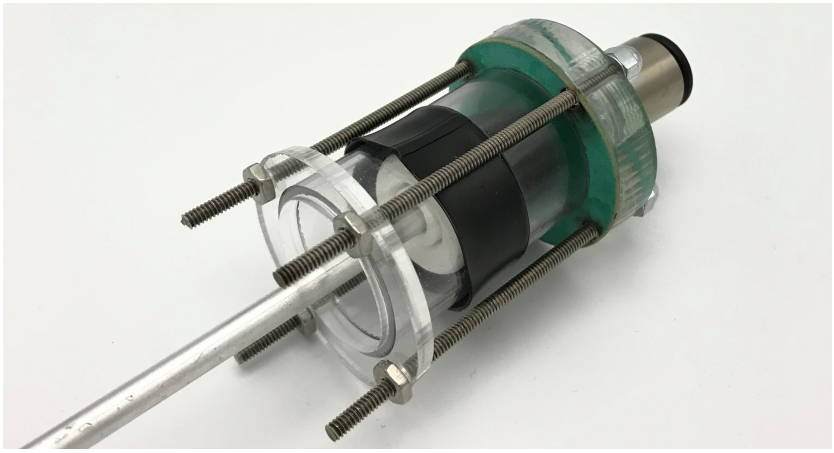

(b) LSRD cylinder with plastic tubes and Plasti Dip elastomer to be used with water.

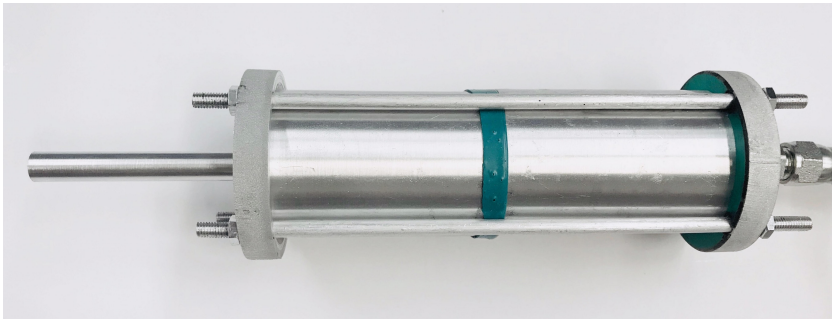

(c) LSRD cylinder with aluminum tubes and polychloroprene elastomer to be used with oil.

Figure 2.6: LSRD cylinders

Friction Test Apparatus

The apparatus shown in Figure 2.7 was used to test the cylinders at different velocities and loads. The force equilibrium for the piston is

$$Mg = PA + F_r \tag{2.1}$$

where M is the weight hanging from the piston, g is the gravitational acceleration, P is the pressure at the outlet, A is the piston rod side area, and F_r is the friction force. A needle valve was used to adjust the velocity of the piston and maintain a constant velocity. The friction was calculated by finding the pressure at the outlet. A non-contacting position sensor (laser distance sensor) measured the rod velocity to ensure that the velocity was constant and the force equilibrium was valid.

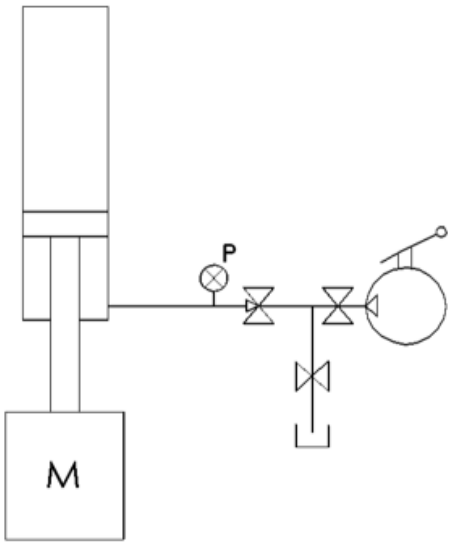

Figure 2.7: Friction test apparatus.

Friction Test protocol

Cylinders with bores in the range of 14 to 22 mm were chosen for the test. The O-ring, gap seal, rolling diaphragm, and LSRD cylinders had bores of 14.33, 15.88, 17.76, and 21.03 mm respectively. With respect to the pressure limit of each cylinder and the maximum force which was needed for future studies, four loads and velocities were

chosen. The hand pump was used to fill the cylinder and lift the weight. The needle valve was set, and the valve to the tank was opened. The weight was moving down with the specific velocity while the fluid passed into the tank. The test was repeated three times for each configuration.

Effective Area Test Apparatus

A hand pump was used to infill the LSRD cylinder with water and press the piston against a force gauge attached to a universal test machine (Figure 2.8). The position of the piston was recorded using the position gauge on the test machine. A pressure transducer was used to measure the fluid pressure.

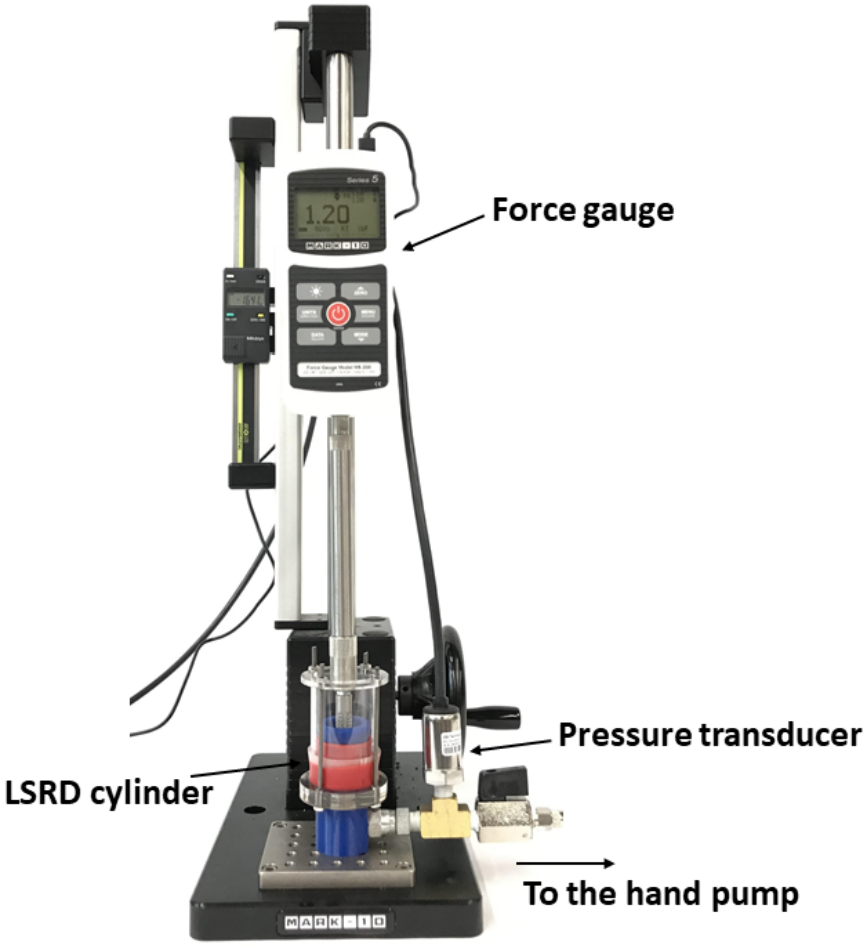

Figure 2.8: Effective area test apparatus.

Effective Area Test Protocol

The LSRD cylinder was filled with water, and the valve between the cylinder and the pump was closed. The pressure was recorded using the pressure gauge while lifting the force gauge. Force and pressure dropped by raising the force gauge, resulting in a relationship between the force and pressure along the stroke. The friction test showed that the friction in the LSRD cylinders is between 2 to 5 percent of the load. The friction in the cylinder was ignored to find the effective area as a proportional relationship

between force and pressure (Equation 2.2)

$$A_{effective} = \frac{Force}{Pressure} \tag{2.2}$$

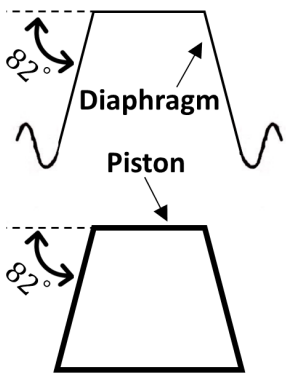

(a) 8 degrees taper angle for D and P.

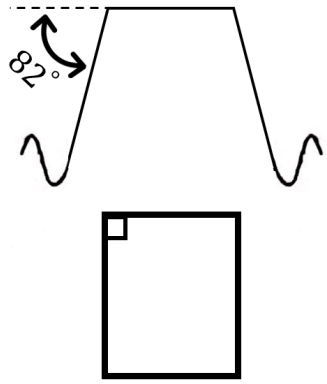

(b) 8 degrees taper angle for D and 0 for P.

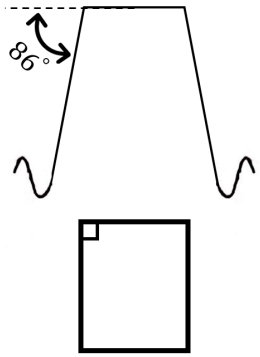

(c) 4 degrees taper angle for D and 0 for P.

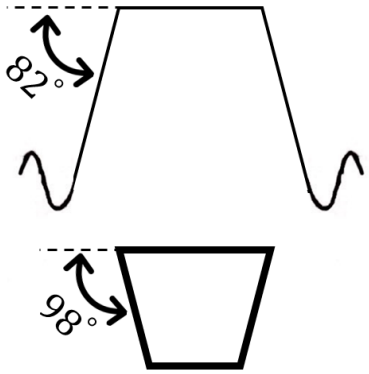

(d) 8 degrees taper angle for D and -8 for P.

Figure 2.9: Diaphragm (D) and piston (P) shape combinations.

To evaluate the effect of piston geometry on the consistency of the effective area along the stroke, several combinations of the diaphragm and piston geometries were tested (Figure 2.9). The diameter of the cylinder and the top diameter of the piston were kept the same in all cases. Under pressure, the diaphragm conformed to the shape of the piston.

Accumulator Design

In an embodiment of the variable hydraulic transmission, an accumulator can be used to hold the pressure in a closed manifold for a nonzero flowrate. Two similar LSRDs were used to make a double-acting cylinder. One side of the cylinder was connected to the hydraulic system and the other diaphragm was pressurized with air (Figure 2.10). Both sides of the piston had the same pressure since both diaphragms were identical. A high volume of pressurized air would let the cylinder work as an accumulator for the hydraulic system. This cylinder can also be used as a hand pump to fill the system with water. Moreover, instead of having a water reservoir, an air hand pump can be used to pressurize the right side of the cylinder and, consequently, the hydraulic system.

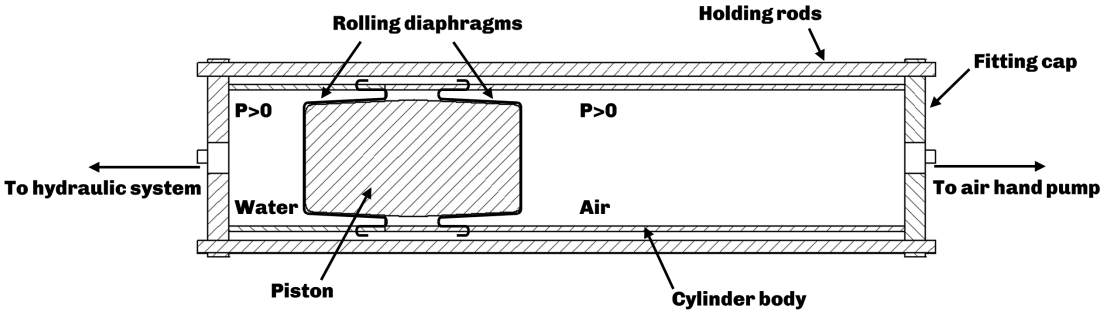

Figure 2.10: Accumulator design using two long-stroke rolling diaphragms.

2.1.3 Results

Friction

Figure 2.11 shows the cylinder friction force as a function of the load for the velocity of 0.5, 1, 1.5, and 2 mm/s. While the friction force elevated as the chamber pressure increased, this figure shows a substantial difference between the various cylinders. In all cases, O-ring cylinders had substantially more friction than gap seal and rolling diaphragm cylinders.

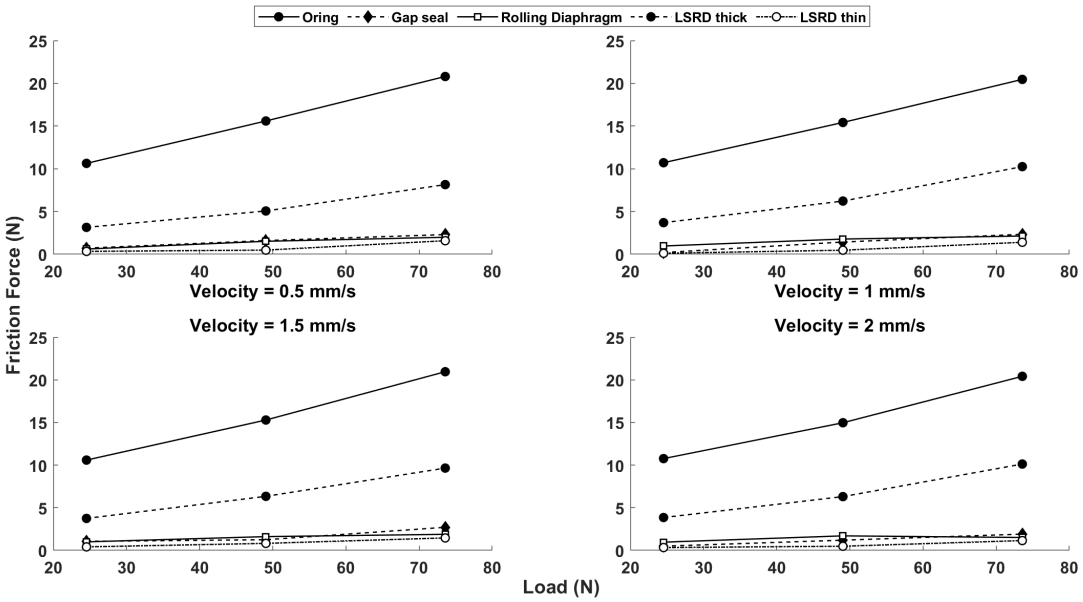

Figure 2.11: Friction force of cylinders as a function of load.

Figure 2.12 compares friction in different cylinders as a function of velocity for various loads. Friction did not change with velocity for all cylinders.

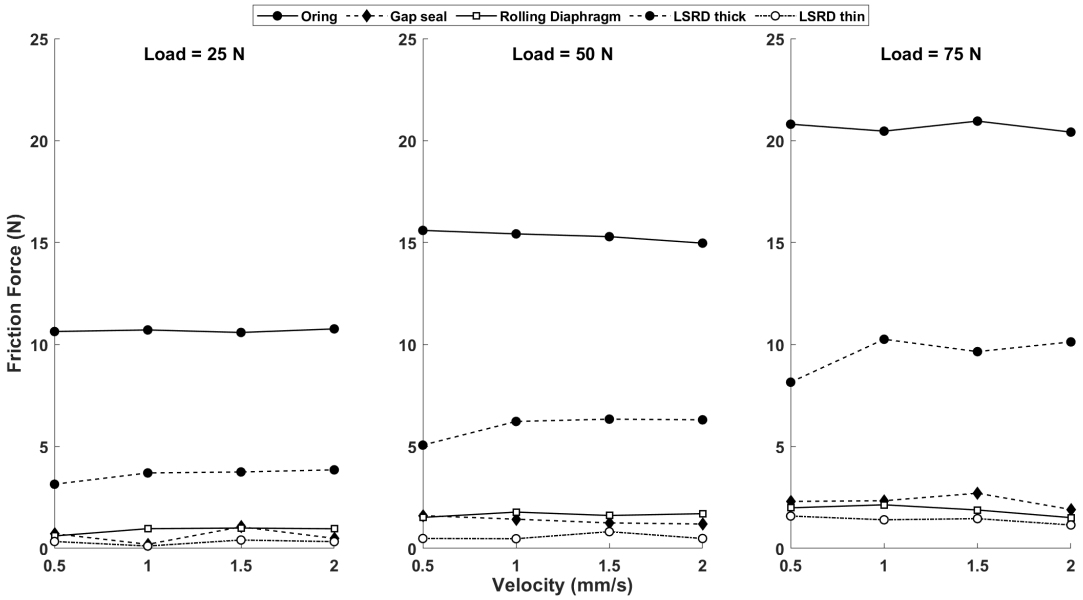

Figure 2.12: Friction force of cylinders as a function of velocity.

Effective Area

An example of the results for force and pressure for the cylinder effective area tests is shown in Figure 2.13. The effective area was then calculated from the experimental results in this figure.

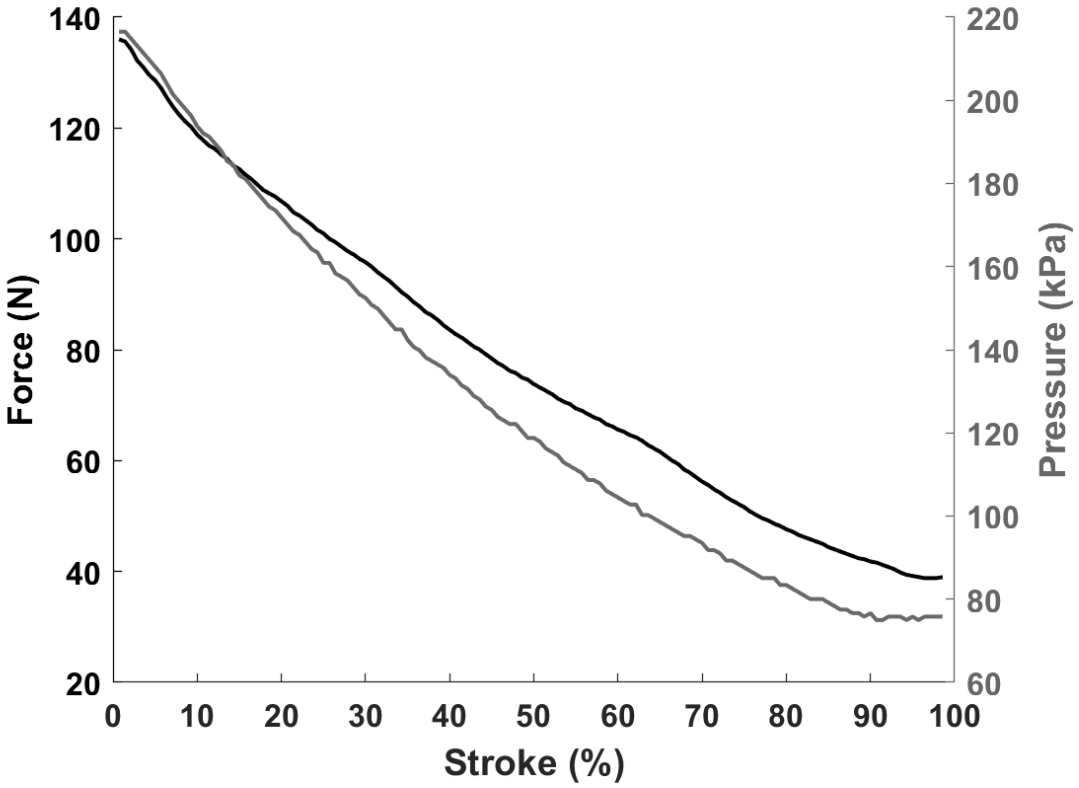

Figure 2.13: An example of the force and pressure data acquired during the effective area test. Force is illustrated in black and pressure in grey.

The effective area of the cylinder with the piston and diaphragm taper angle of 8 degrees dropped moving along the stroke (Figure 2.14).

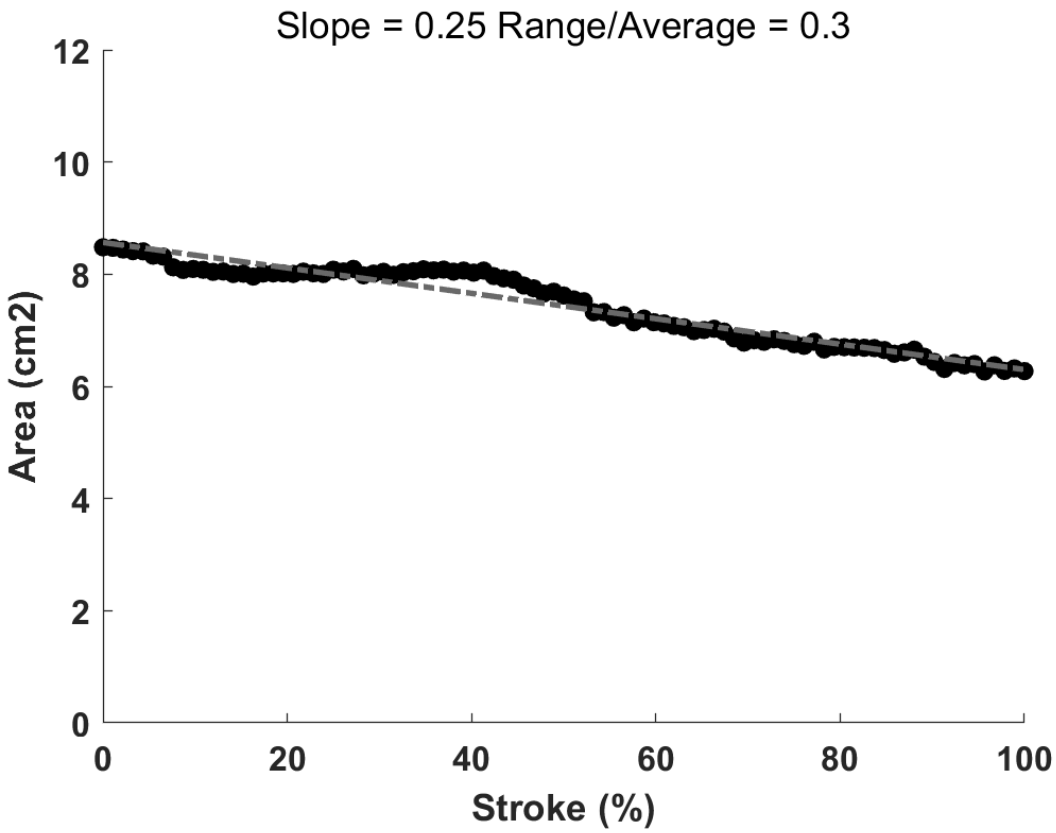

Figure 2.14: The effective area along the stroke for 8 degrees taper angle for diaphragm and piston. The black dots are calculated from experimental data. The gray dashed line is the fit to the experimental data.

The drop in effective area by going through the stroke can be adjusted by making an untapered piston. The experimentally calculated effective area for the piston's position with an LSRD with the mold taper angle of 8 degrees and a perpendicular piston is shown in Figure 2.15.

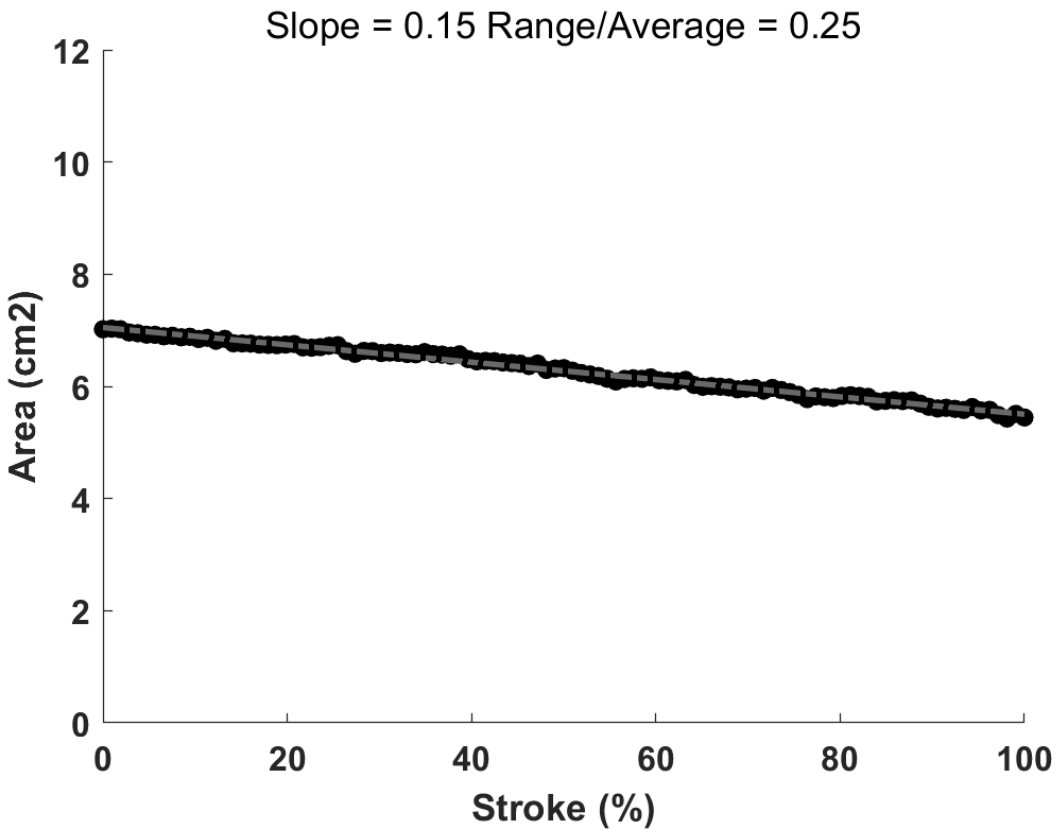

Figure 2.15: The effective area along the stroke for 8 degrees taper angle for diphragm and 0 for piston

The effective area remained more consistent by reducing the diaphragm taper to 4 degrees (Figure 2.16). However, a low-tapered molded diaphragm increases the friction in the rolling action due to higher wear on the folded diaphragm wall.

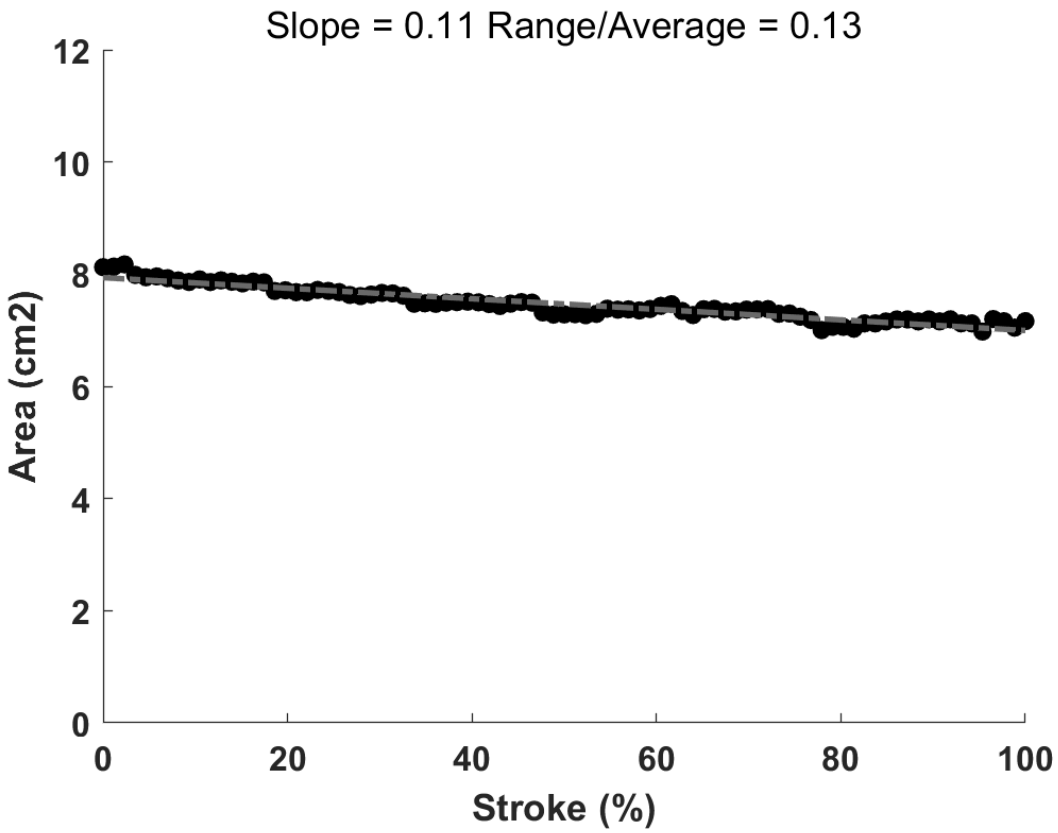

Figure 2.16: The effective area along the stroke for 4 degrees taper angle for diaphragm and 0 for piston.

Keeping the LSRD mold taper angle at 8 degrees assured low friction in the rolling action. To compensate for the area reduction, the piston can be shaped with a reverse taper to provide the opposite force by letting the diaphragm conform to the shape of the piston. Figure 2.17 shows how this combination results in a constant effective area with piston position.

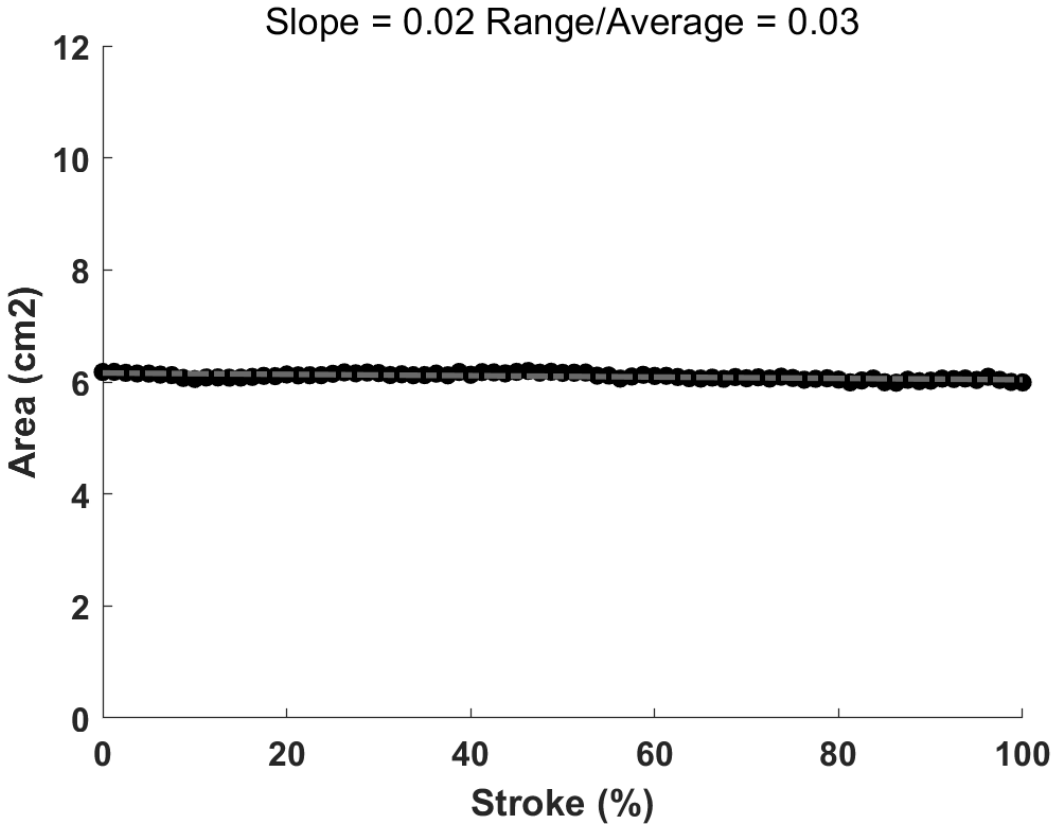

Figure 2.17: The effective area along the stroke for 8 degrees taper angle for diaphragm and -8 for piston.

The effective areas for a small and a large cylinder are shown in Figure 2.18. The cylinder bore, piston diameter, the average of the cylinder and piston areas, and the effective area using the piston shape shown in Figure 2.17 are reported in Table 2.1. These two cylinders were chosen to be used in the variable hydraulic transmission discussed in the next chapters and the exact effective area had to be found for the transmission ratios to be predicted.

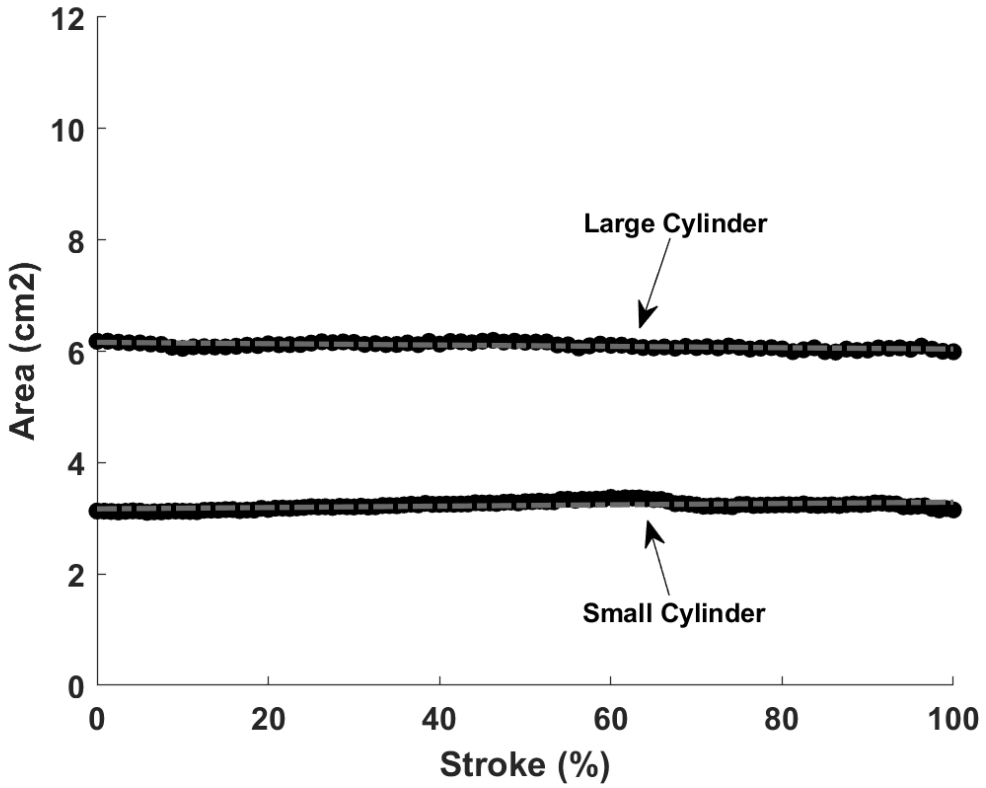

Figure 2.18: Effective area along the stroke for a 3.5 cm and a 2.5 cm bore cylinders using the tapers shown in Figure 2.9d

Table 2.1: Dimensional data for large and small bore cylinders.

	$A_{cyl}(cm^2)$	$A_{pis}(cm^2)$	$A_{average}(cm^2)$	$A_{effective}(cm^2)$
Large cylinder (3.5 cm bore)	9.58	4.1	6.84	6.16
Small cylinder (2.5 cm bore)	5.07	2.16	3.62	3.17

2.1.4 Discussion

Force and Volume Efficiency

The experimental results demonstrate that friction for all types of cylinders increases with load. However, system efficiency generally increases with higher pressures [47] .The results from the test show that friction is independent of velocity for all the cylinders in this range of speed (less than 2 mm/s). However, there is a possibility of friction and velocity dependency at higher velocities.

The results show a 28 to 40 percent of friction to load for O-ring cylinders. Therefore, this type of cylinders is not recommended for low-pressure, passive hydraulic devices that must operate at high efficiency. The results indicate two to five percent friction force to load for gap seal and rolling diaphragm cylinders. As shown in Figure 2.11, the friction for these two cylinder types is almost the same. Passive hydraulic devices need a force and volume efficient actuator with lower leakage than the gap seal and a longer stroke length than the current diaphragm technologies. Hysteresis is the only factor creating friction force against the movement in rolling diaphragms, and it is higher in thicker diaphragms. The friction is about 12 percent of the load for thicker diaphragms. The results show that friction in a thin LSRD is the same as the commercial rolling diaphragm and gap seal cylinders. LSRDs can have higher stroke-to-bore ratios, whereas all commercial rolling diaphragms have stroke-to-bore ratios of 1 or less. The high stiffness of the polyurethane sheet allows for a smooth rolling action and high enough stiffness to prevent bulging. There is a trade-off for thinning the elastomer to be used for the coating. Thinner elastomer assures lower friction in rolling movement, while thicker elastomer acts as a backup seal in the diaphragm.

The LSRD cylinder constructed for this study weighed about 67g. It is noted that the long-stroke diaphragm's weight is negligible compared to the total weight of the LSRD cylinder. Therefore, the LSRD cylinder tested is a good alternative for gap seal cylinders or for cylinders having traditional rolling diaphragms, since they have a leakage problem and stroke limitations respectively.

Stroke Length

The stroke length versus cylinder bore size is shown in Figure 2.19. The black dots represent commercial diaphragm cylinders and the square represents the new LSRD cylinder. The gray region is for the commercial rolling diaphragm cylinder and the region bounded by dashed lines is for the new LSRD cylinder. Since the target application of these cylinders is small hydraulics, the figure shows bore sizes only up to 120 mm.

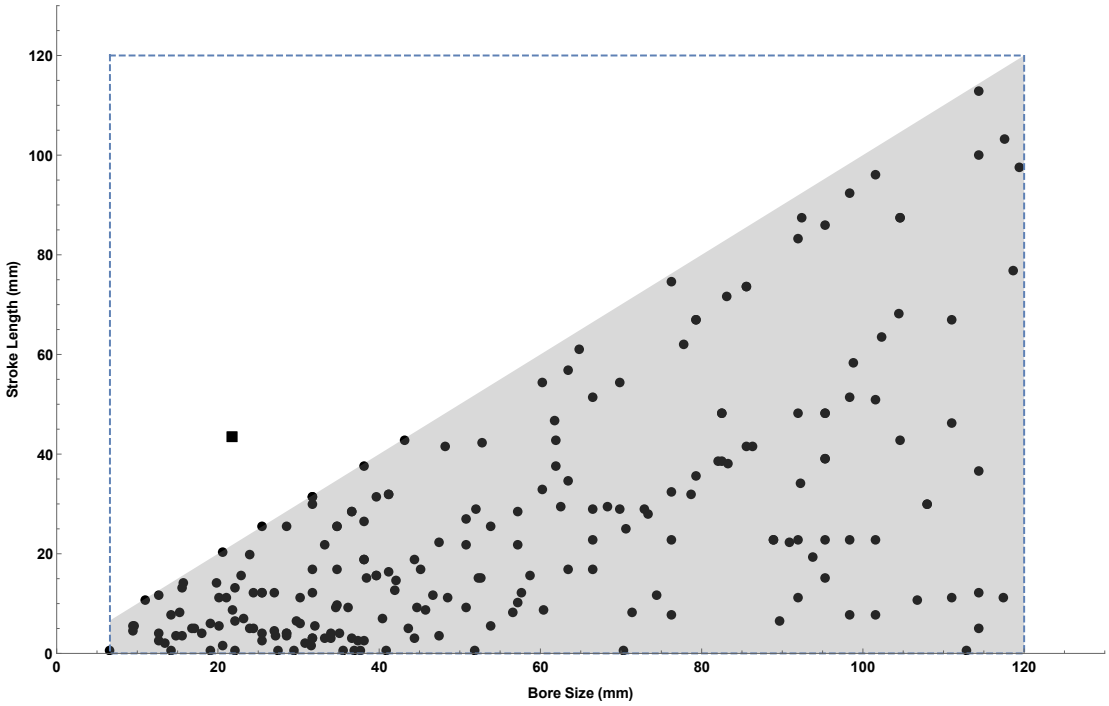

Figure 2.19: Stroke length of rolling diaphragms as a function of bore size. Light gray area indicates stroke-bore capability of commercial diaphragm and region bounded by dashed line indicates LSRD. Black dots are some of the commercial rolling diaphragm samples and the black square is the LSRD tested in this study.

A fatigue test of 1000 cycles was performed on the thinner diaphragm, and a burst pressure of 2400 kPa (350 psi) was measured.

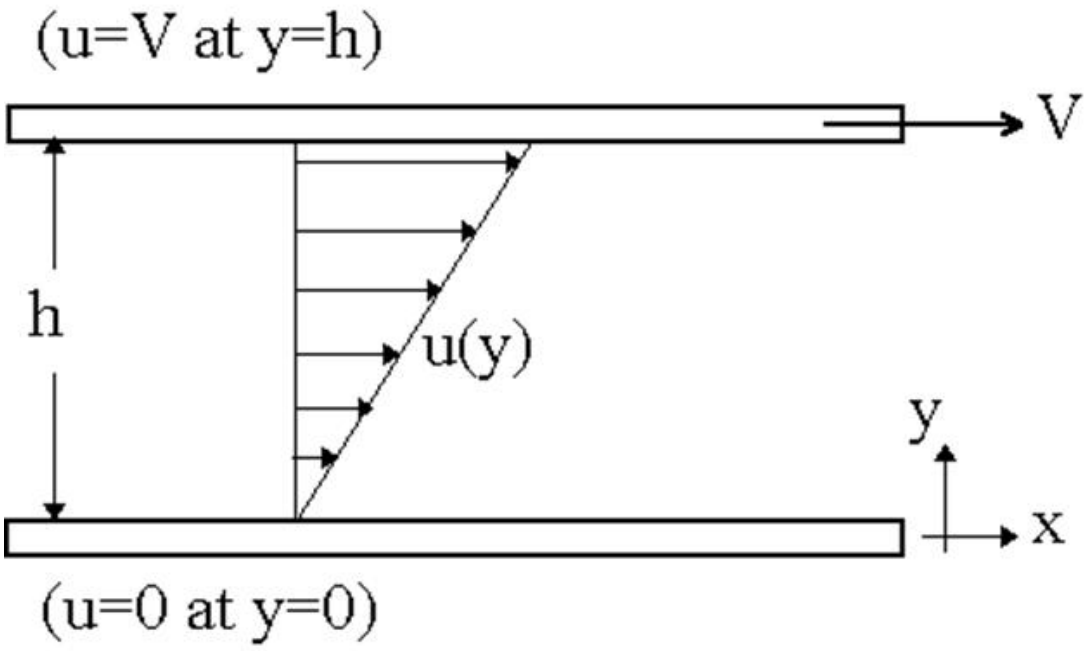

Figure 2.20: Fluid streamline in a two parallel sheets, with the top sheet moving and bottom sheet stationary.

Friction Dependency on Pressure

The thin layer of fluid between cylinder and piston in the gap seal cylinder can be modeled as shown in Figure 2.21. The upper wall is similar to the piston in Figure 2.1 which is moving with specific velocity. The lower one is similar to the cylinder wall, which is at rest. The relationship for shear stress for the parallel motion of streamlines in a moving fluid is

$$\tau = \mu \frac{du}{dy} \tag{2.3}$$

where μ is the dynamic viscosity and du/dy is the rate of velocity change.

The frictional force equals

$$F_r = \tau A \tag{2.4}$$

where A is the area of each sheets [54, 55]. When only one side of the piston is pressurized, a pressure gradient develops, allowing leakage to occur through the gap. The

piston moves with gravity, the motion of the upper plate is downward same as the pressure gradient in our test, when the pressure increases in the direction of the upper plate motion adverse pressure gradient happens and backflow may occur.

When the cylinder is sitting vertical, the piston is traveling downward. The fluid in the gap is going upward in relation to the piston, causing the du/dy value to increase, implying that there will be more friction force in the gap than if the pressure gradient is favorable. As we increase the load in the test, the working pressure would be increased, and we would have more leakage with higher relative velocity. It makes the du/dy value and the friction force larger. That is why the load and the friction force are dependent on the gap seal cylinders.

In the O-ring cylinders, the friction force is caused by the contact of the O-rings and the cylinder. The friction caused by this type of sealing depends primarily on seal compression, fluid pressure, and projected seal area exposed to pressure. The effects of materials, surfaces, fluids, and speeds of motion are normally of secondary importance. Friction in the O-rings (it can be used for both of the rod and piston frictions) is

$$F_C = f_c L_p \tag{2.5}$$

$$F_H = f_h A_p \tag{2.6}$$

$$F_r = F_C + F_H \tag{2.7}$$

Where

A_p: Projected area of seal for piston/rod groove applications.

L_p: Length of seal rubbing surface in inches for piston/rod groove applications.

f_c: Friction due to O-ring compression obtained from Figure 2.22

f_h: Friction due to fluid pressure obtained from Figure 2.23.

F_C: Total friction due to seal compression.

F_H: Total friction due to hydraulic pressure on the seal.

F_r: Total seal friction.

f_c and f_h can be found from Figure 2.22 and 2.23. As it is shown, friction force in the O-rings depends on fluid pressure. The reason for this is that pressure will distort the

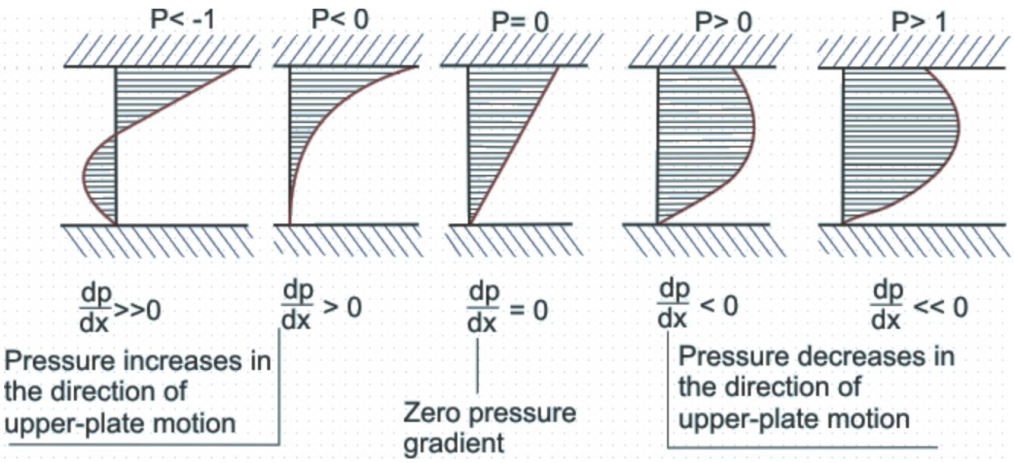

Figure 2.21: Adverse and favorable pressure gradient.[1]

O-ring in the groove, changing the area of contact between the O-ring and the wall. As the load in the test is increased, the fluid pressure rises, causing the f_h to rise, resulting in increased friction in the O-rings. That is why the friction depends on the load in O-ring seal type of cylinders [6]. Friction increases with pressure (load) and remains nearly constant when velocity changes, as reported in this study. Furthermore, a recent study indicated that the force efficiency increases with pressure [47]. The friction and actuation forces depend on the pressure in the chamber; however, the actuation force elevates at a faster rate than the friction. Therefore, the efficiency will rise with the increasing the pressure.

In the rolling diaphragm cylinders hysteresis due to bending and unbending of the rubber causes the friction. As thicker diaphragms have higher hysteresis, they need more force for rolling action. Hysteresis is calculated in [50] in different working pressures and it is shown that hysteresis is higher if the working pressure in the cylinder is increased.

Effective Area

The effective area of the LSRD varies through the stroke due to the tapered shape of the diaphragm (Figure 2.9a). In this case, the range of the area over the average of the area is 0.3. Having a consistent effective area enables the cylinder to provide

[1] image from $(http://www.nptel.ac.in/courses/112104118/lecture-26/26-1_couette_6low.htm)$

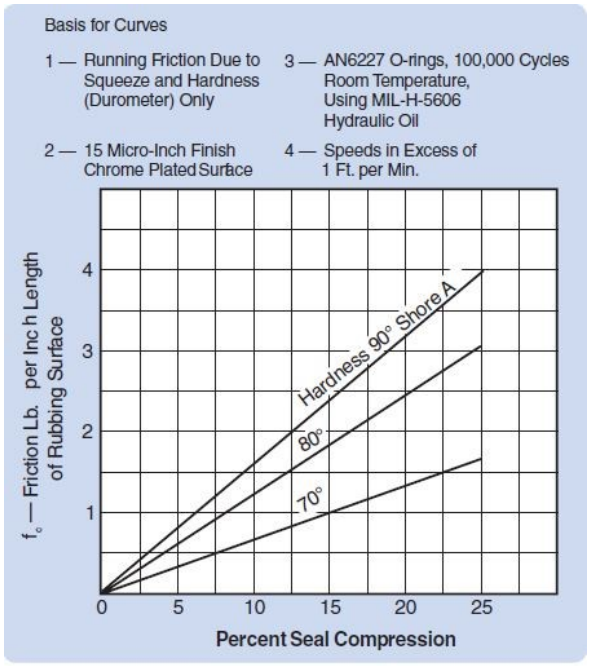

Figure 2.22: Friction due to O-ring compression (image from [6])

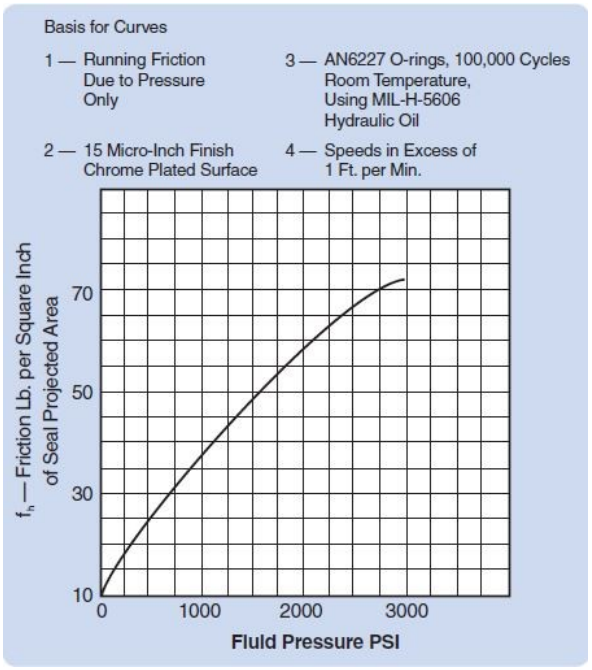

Figure 2.23: Friction due to fluid pressure (image from [6])

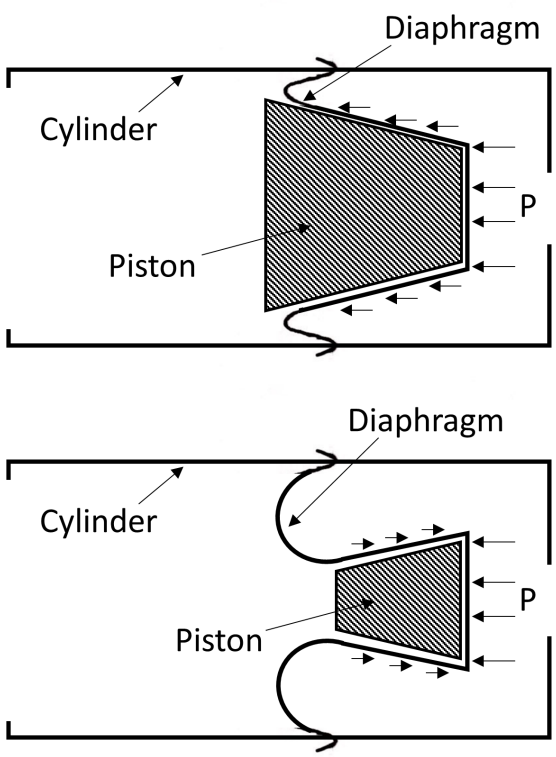

Figure 2.24: Forces on a tapered piston vs. a reverse tapered piston.

consistent mechanical performance. A flexible diaphragm can reshape to the shape of the piston, and using a perpendicular piston decreases the effect of the tapered diaphragm (range/average of 0.25). Increasing the diaphragm mold angle (straighter) decreases the variance in the effective area (range/average of 0.13) (Figure 2.16). To keep the friction low in the rolling movement, the diaphragm with 8 degrees taper angle was chosen. To compensate for the variance in the area, the reverse tapered piston was selected that provides a backward force to compensate along the stroke since the diaphragm would wear the piston's shape, and the pressure of the fluid would reach the taper wall of the piston (Figure 2.24). The reverse tapered piston flattens the effective area; however, it reduces the cylinder's net force (Figure 2.17) Table 2.1 illustrates this because the effective area in this method is lower than the average area of the piston and the cylinder. The lower average effective area is the expense for consistent force efficiency along the stroke (range/average of 0.03).

2.1.5 Conclusion

In this chapter, a manufacturing method for a long-stroke rolling diaphragm cylinder was presented. An experimental test was performed on three different commercial technologies and two long-stroke rolling diaphragms with different thicknesses. The results showed that friction is dependent on pressure and it rises with increasing pressure. Further, the results demonstrated high friction for O-ring seal cylinders, and the same low range of friction for gap seal, rolling diaphragm, and thin long-stroke rolling diaphragm cylinders. Higher friction in the thicker long-stroke rolling diaphragm compared to the thinner one results from the higher hysteresis and resistance forces for thicker elastomer. A thin rolling diaphragm with high stroke capabilities is a good choice for a high-efficiency, low pressure hydraulic system compared to gap seal cylinders or commercial rolling diaphragms, as they have leakage problems and stroke limitations respectively.

Due to the diaphragm's tapered shape, the effective area of the cylinder decreases as the diaphragm rolls forward. A higher taper angle for the diaphragm and piston intensifies this variance. Reducing this angle (straighter diaphragm) increases the friction due to the smaller gap in the rolling surfaces. To prevent additional friction, a taper angle of 8 degrees was chosen for the diaphragm. The long-stroke rolling diaphragm is capable of conforming to the shape of the piston. A reversed shape for the piston (taper angle of -8 degrees) resulted in a constant (but lower) effective area along the stroke. This refined long-stroke rolling diaphragm can be used in small hydraulic devices to achieve high force and volume efficiencies.

2.2 Valves

2.2.1 Introduction

Digital fluid power is the controlling of system output using hydraulic or pneumatic components that are coupled to the system with switching valves [56]. Hydraulic valves are required to control the hydraulic cylinders in a digital hydraulic system [57]. In one of the applications of digital fluid power, power is transmitted between several joints via a passive hydraulic transmission [58]. A similar embodiment is being incorporated in the variable hydraulic transmission described in this thesis with several hydraulic

cylinders placed on each joint and two switching valves used for each cylinder in the transmission to connect and disconnect cylinders from the system. The switching valves allow variable transmission ratios between the joints. As shown in Figure 1.2, the system is passive, and motors or pumps are not being used in the transmission; therefore, the hydraulic components must preserve the power. The most critical factors for hydraulic switching valves in the system are pressure drop, actuation energy, response time, size, and weight. Minimum hold power for digital valves is also required to reduce overall power consumption [56].

The advantages and disadvantages of various architectures of digital valves are shown in Figure 2.25. The valve analysis in this section is to find a low pressure drop architecture valve with minimum switching energy to be used in the hydraulic transmission. The orifice in a hydraulic valve creates a pressure drop across the valve that must be minimized. One can choose a switching valve architecture by considering the pressure drop inherent to each architecture. Poppet and spool valve architectures have a significant pressure drop due to the change in the flow direction and small orifice size [59, 60]. Ball, plug, choke, butterfly, and gate valves have minimal pressure drop because when they are fully open they present no obstruction to the flow of fluid. K factor for ball and butterfly valve pressure drop by CFD modeling and experimental methods is as low as 0.2 [61, 62, 63]. Using a K factor of 0.2, the pressure drop across these valves in the open position with mineral oil and flow velocity of 3 m/s is calculated to be as low as 720 Pa. These are the valve types suited for a high-efficiency digital hydraulic system.

The energy required to switch the valve state should be minimized to decrease the motor size and allow fast response time since fast and frequent switches are needed to control the output. The size and weight of the valves should be small to make the device portable. Analytical models can be used to determine which architecture is best suited for digital hydraulic transmission to be used in lightweight, portable applications. Of the many valve architectures, ball and butterfly valves are actuated rotationally and satisfy the minimum pressure drop requirement in the open position, and therefore, were chosen for further consideration. A cross-sectional view of a ball valve is depicted in Figure 2.26. The ball is seated between two O-rings to prevent leakage. A cross-sectional view of a butterfly valve is shown in Figure 2.27. An O-ring is seated on the disc to prevent leakage in the closed position. Using an O-ring model and an estimate

Rotational Valves

Ball Valve*

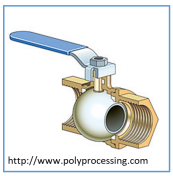

* That includes plug valve as well.

Advantages:
- No pressure drop
- Quick shut off

Disadvantages:
- Needs relatively high torque to rotate
- Size

Butterfly Valve

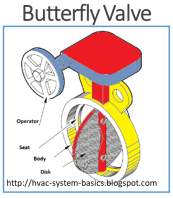

Advantages:
- Needs relatively low torque to rotate
- Quick shut off
- Good for low pressure
- Small pressure drop

Disc Valve

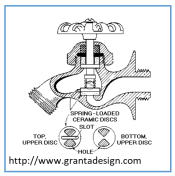

Advantages:
- Needs relatively low torque to rotate
- Quick shut off
- Size

Disadvantages:
- High pressure drop

Translational Valves

Choke Valve

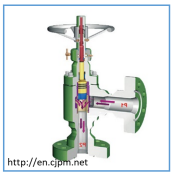

Advantages:
- No pressure drop
- Quick shut off

Disadvantages:
- High friction

Diaphragm Valve

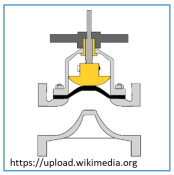

Advantages:
- Low leakage
- No pressure drop

Disadvantages:
- Needs high force to shut off

Gate Valve*

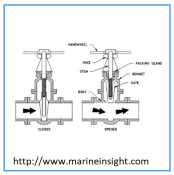

* That includes knife valve as well.

Advantages:
- No Pressure Drop

Disadvantages:
- Needs high force to shut off
- Slow shut off

Globe Valve*

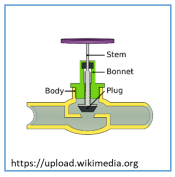

* That includes piston valve as well.

Advantages:
- No leakage

Disadvantages:
- Pressure drop
- Slow shut off

Needle Valve

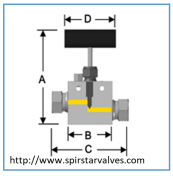

Advantages:
- Size

Disadvantages:
- Slow shut off
- Pressure drop

Pinch Valve

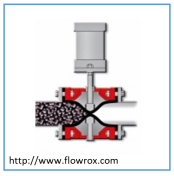

Advantages:
- Good for flexible hoses
- No pressure drop

Disadvantages:
- High spring energy

Solenoid Spool Valve

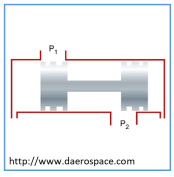

Advantages:
- No leakage

Disadvantages:
- Pressure drop
- Size

Solenoid Seat Valve

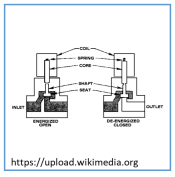

Advantages:
- Size
- Quick shut off

Disadvantages:
- Small pressure drop

Figure 2.25: Valve types that can be used in a BPWR hydraulic transmission.

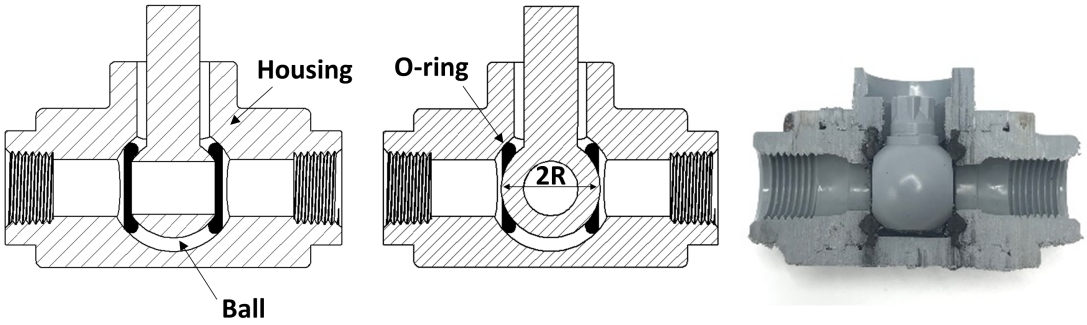

Figure 2.26: A cross-sectional view of a ball valve rendering in the open (left), closed (middle), and actual valve cut through the center (right).

of the inertia of the valve moving parts, the energy required to switch these valves can be estimated to provide specifications for the rotary actuator needed to turn the valve stem.

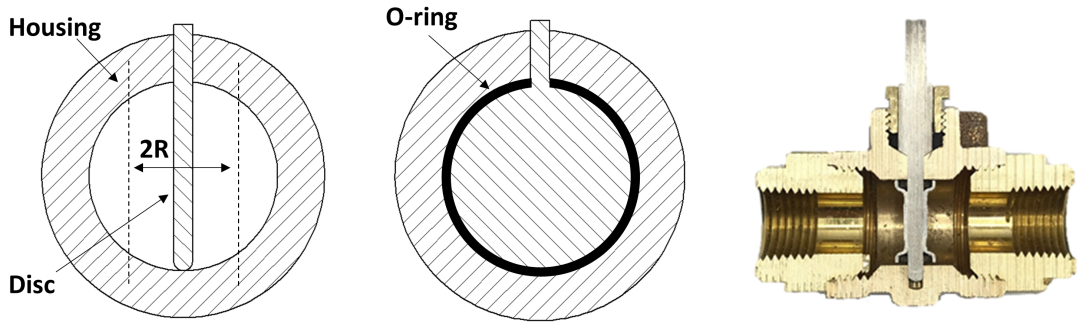

Figure 2.27: A cross-sectional view of a butterfly valve rendering in the open (left), closed (middle), and actual valve cut through the center (right).

Analytical models of O-ring friction were used to estimate the energy required to turn the valve. To validate the models, experiments were conducted to measure the torque required to turn the stem of several physical valves. The results were compared to what the model predicted for matching the geometry.

2.2.2 Methods

Actuation Energy

The energy needed to switch a rotational valve can be estimated by

$$E = \frac{1}{2} I\omega^2 + E_{friction} \tag{2.8}$$

The first term is the average rotational kinetic energy while the valve switches and the second term is the energy to overcome friction caused by the O-rings (or other sealing type). The first term turns out to be negligible compared to the friction term based on the numbers found in the results. The rotational kinetic energy was calculated for a stainless-steel block to rotate 90 degrees and it is less than 1 mJ. The primary source of energy required to switch the valve is therefore caused by friction, which can be split into two terms

$$E_{friction} = E_{preload\,friction} + E_{pressurized\,friction} \tag{2.9}$$

The preload friction energy is due to the friction force caused by the O-rings when there is no fluid pressure on either side of the closed valve while the second term is due to the additional friction force caused by fluid pressure on one or both sides of the valve. The following sections derive analytical estimates for the friction terms for ball and butterfly valves.

Friction Torque in Ball and Butterfly Valves

The friction force in the O-ring seal can be modeled by

$$F_{friction} = 2\pi\mu_f D_1 r E(1 - \frac{D_1 - d_2}{4r})\sqrt{(1 - \frac{(D_1 - d_2)^2}{16r^2})} \tag{2.10}$$

where μ_f is the friction coefficient, D_1 is the sealed surface diameter (housing diameter in the valve), d_2 is the inside diameter (ball diameter in ball valve and disc diameter in butterfly valve), E is the modulus of elasticity of the O-ring, and r is the radius of the O-Ring section as shown in Figure 2.28 [64, 47].

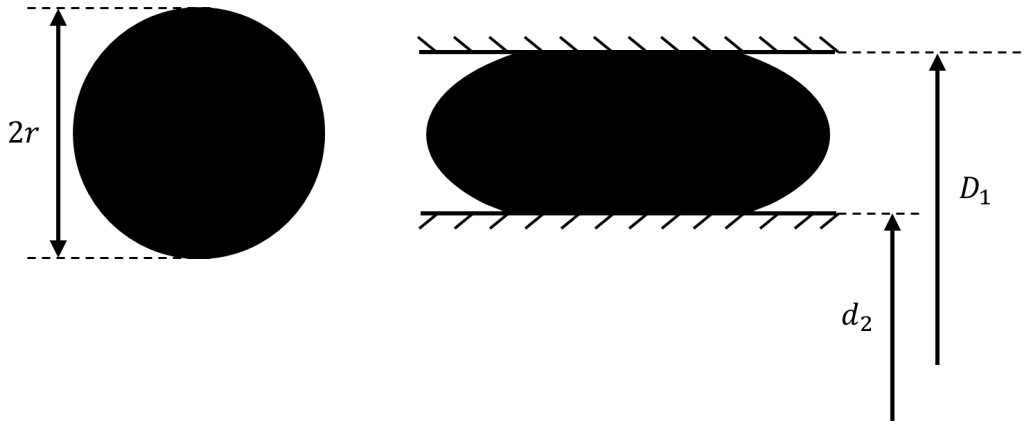

Figure 2.28: An O-ring seal dimension before and after contact.

The O-ring squeeze ratio is defined as

$$\epsilon = (1 - \frac{D_1 - d_2}{4r}) \tag{2.11}$$

The friction force is therefore

$$F_{friction} = 2\pi\mu_f D_1 r E \epsilon \sqrt{2\epsilon - \epsilon^2} \tag{2.12}$$

The friction force is converted to a valve actuation friction torque using the moment arm R shown in Figures 2.26 and 2.27. For the butterfly valve, the moment arm is estimated as the average distance from the O-ring to the stem. The friction torque is therefore

$$T_{friction} = 2\pi R\mu_f D_1 r E \epsilon \sqrt{2\epsilon - \epsilon^2} \tag{2.13}$$

To estimate the switching energy for the pressurized condition (the second term in Equation 2.9), two cases must be considered as shown in Figure 2.29. The first case (Figure 2.29 left) is when the pressure on both sides of the valve is the same. Here, the net force on the valve is zero, and the O-ring squeeze ratio for both O-rings will remain the same, and therefore the friction torque will be the same.

The second case (Figure 2.29, right) is when the pressure on one side of the blockage is higher than the other side. This term is always zero for the butterfly valve since the

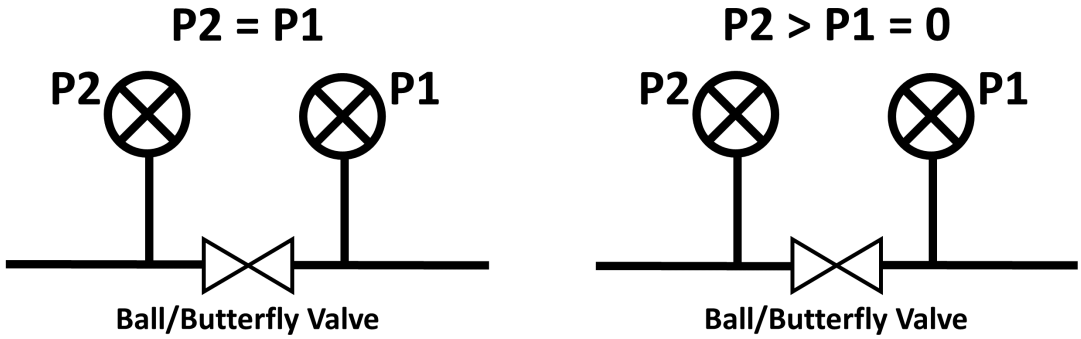

Figure 2.29: Pressure on both sides of the valve (left), pressure only on one side of the valve (right).

pressure on the disc is canceled out around the shaft and the squeeze ratio of the O-ring is not affected by the pressure. This term is not zero for the ball valve since the ball in the valve will be pushed against one of the O-rings while d_2 for the other O-ring will decrease. While there is a linear relationship between d_2 and squeeze ratio ϵ, the relationship between ϵ and friction force is not linear. Thus, the increased torques by the pushed O-ring and released one are not equal and the net torque will increase with pressure for this case.

To parameterize the model, two commercial ball valves and one commercial butterfly valve were chosen for experimental characterization. The valves were: (1) a high-pressure stainless-steel ball valve (G-SSMF-12NL) with PTFE O-ring and a maximum pressure of 7000 kPa, (2) a low-pressure ball valve (SMC 5742890) with PVC body and Buna-N O-ring for pressures up to 850 kPa, and (3) a butterfly valve with FKM O-ring a maximum pressure of 1200 kPa.

Equation 2.13 was used to model the torque required to switch the valve. The parameters for each ball valve are shown in Table 2.2. Since the highest torque was measured in model validation, μ_f was chosen to be 0.7. Two parameters were chosen to be estimated to fit the model to the experimental results for the ball valve. The first parameter was D_1 (housing diameter) since it is challenging to measure with high accuracy without a coordinate measuring machine. The second parameter was Δd_2 which is the displacement of the blockage inside the housing due to the differential pressure on it. This displacement was assumed to be an increase in d_2 (ball diameter)

for the pushed O-ring and a decrease in d_2 for the released O-ring. The torque equation can therefore be written as

$$T_{friction} = T_{pushed\,o-ring} + T_{released\,o-ring} \tag{2.14}$$

$$T_{pushed\,o-ring} = 2\pi R\mu_f D_1 r E(1 - \frac{D_1 - (d_2 + \Delta d_2)}{4r})\sqrt{1 - \frac{(D_1 - (d_2 + \Delta d_2)^2}{16r^2}} \tag{2.15}$$

$$T_{released\,o-ring} = 2\pi R\mu_f D_1 r E(1 - \frac{D_1 - (d_2 - \Delta d_2)}{4r})\sqrt{1 - \frac{(D_1 - (d_2 - \Delta d_2)^2}{16r^2}} \tag{2.16}$$

where Δd_2 is proportional to the pressure and the stiffness of the O-ring

$$\Delta d_2 = \frac{1}{\alpha} P \tag{2.17}$$

Parameter α in Equation 2.17 was obtained via fitting the model to the experimental results using the least squares method.

Table 2.2: Ball valves parameters.

	$E(MPa)$	μ_f	$d_2(mm)$	$r(mm)$	$R(mm)$
High-pressure Valve	500	0.7	13.97	1.143	5.334
Low-pressure Valve	10	0.7	13.97	1.27	5.842

The parameters for the butterfly valve are shown in Table 2.3. d_2 (disc diameter) was adjusted to fit the experimental data as it cannot be measured directly due to the uneven shape of the O-ring groove on the disc. As discussed above, the pressurized term in Equation 2.9 was zero for the butterfly valve.

Table 2.3: Butterfly valve parameters.

	$E(MPa)$	μ_f	$D_1(mm)$	$r(mm)$	$R(mm)$
Butterfly Valve	18.5	0.7	17.04	1.143	4.26

Friction Energy in Ball and Butterfly Valves

The energy required to turn the ball valve is mainly a function of the two O-rings acting on the ball and can be estimated by

$$E_{friction} = 2 \times \Delta S \times F_{friction} \tag{2.18}$$

where ΔS is the distance the ball travels on the O-rings. Since the ball travels 90 degrees during a switch, the distance is

$$\Delta S = R \times \frac{\pi}{2} \tag{2.19}$$

For the butterfly valve, there is no friction during most of the rotation until the O-ring mounted on the disc meets the housing just before the valve fully closes. The energy to switch a butterfly valve can, therefore, be estimated by

$$E_{friction} = 2 \times F_r \times t \tag{2.20}$$

where F_r is the friction force and t is the disc thickness. (The friction force acts on the housing in two areas.)

Valve Switching Time

A fast valve switching time is required to change the output of a digital hydraulic system. The maximum power required for the motor tasked with turning the valve is

$$P = \frac{E}{t} \tag{2.21}$$

where E is the maximum energy needed to switch the valve and t is the switching time. A motor with more power will reduce the switching time, but at the cost of increased weight and size.

Model Validation

Since the primary cause of the energy required to switch the valve is friction, the torque required to turn the valve at a slow speed can be measured experimentally to validate the model. The three valves listed in the last section were tested. For each valve, a

timing belt pulley was attached to the stem (Figure 2.30), and a timing belt ran between the pulley and a digital force gauge (with 0.005 lbf (0.02 N) resolution) so that pulling on the force gauge turned the valve.

Figure 2.30: Ball valve with the timing belt pulley used in experiments to turn the valve.

The hydraulic circuit shown in Figure 2.31 was used to pressurize the valve under test. The isolation valve connected or disconnected the distal side of the valve to the pump. The isolation valve was left open for the test case where both sides of the valve were at the same pressure. It was closed for the test case where only one side of the valve was subject to pressure. Figure 2.32 shows the entire apparatus used for the experiment.

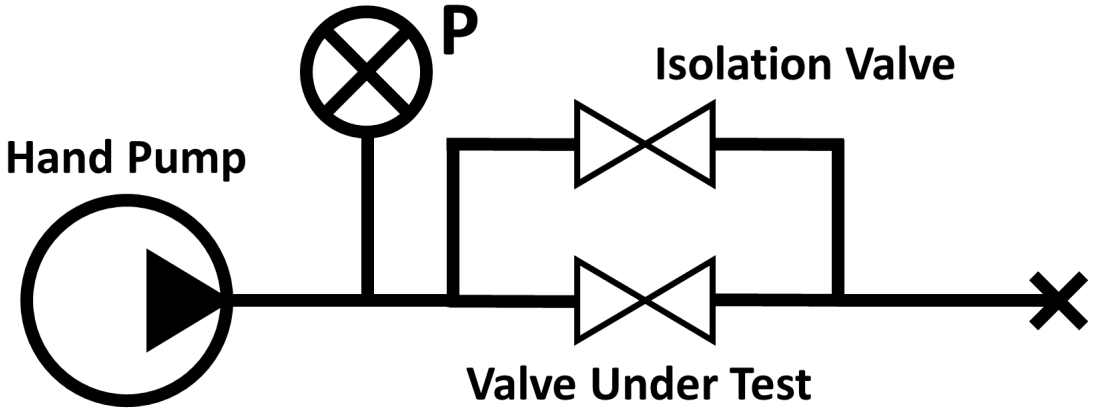

Figure 2.31: Experiment hydraulic circuit.

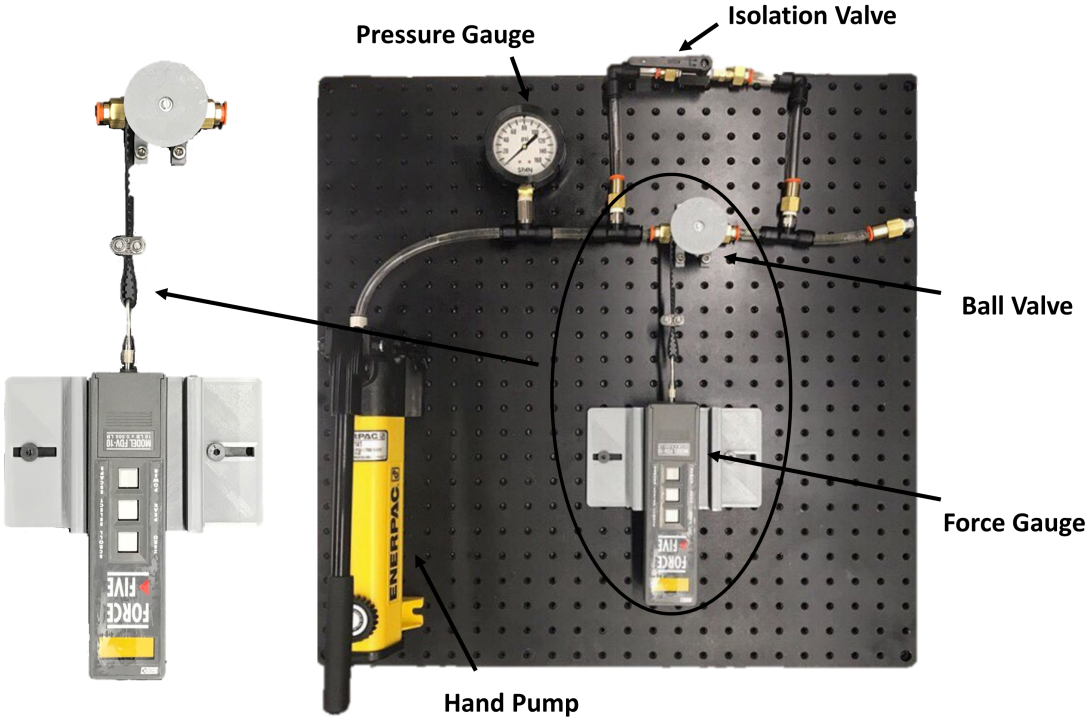

Figure 2.32: Experiment apparatus for the valve friction tests.

Mineral oil was used as the media, and torque was measured at five pressures (0 to 690 kPa) for the case when the valve was pressurized on both sides and the same five pressures when only one side of the valve was pressurized. Each test condition was repeated five times.

Friction Torque as a Function of Valve Position

The torque-angle relations for ball and butterfly valves were measured to determine the O-Ring friction effect on the switching torque. To measure the angle, reflective markers were placed on the pulley and its motion was captured with a video camera. Torque and angle were acquired for one ball and one butterfly valve and repeated four times for each case. The tests were conducted at 0 kPa with mineral oil on both sides of the valve.

Motorized Valve Design

A commercial plug valve shown in Figure 2.33 was used to construction a motorized switching valve prototype because of its low friction torque required to switch (Coleparmer EW-30600-00). This valve had zero leakage for pressures up to 275 kPa (40 psi).

Figure 2.33: Two-way valve. (Image from www.coleparmer.com)

Brushed micromotors were placed on each valve to actuate the valves automatically. The motor and controller for each valve are shown in Figure 2.34 (Pololu #3063 and #2999). The motors were nominally rated for 6 volts; however, 12 volts was used to increase the speed of the actuation. The motors were energized for less than a second and higher voltage can be used without any damage due to the high power. The valve actuator only needed to rotate 60 degrees to block the flow. Lower displacement in blockage decreases the response time and actuation time of the valves. Two mechanical stops were placed to limit the displacement of the blockage (Figure 2.35).

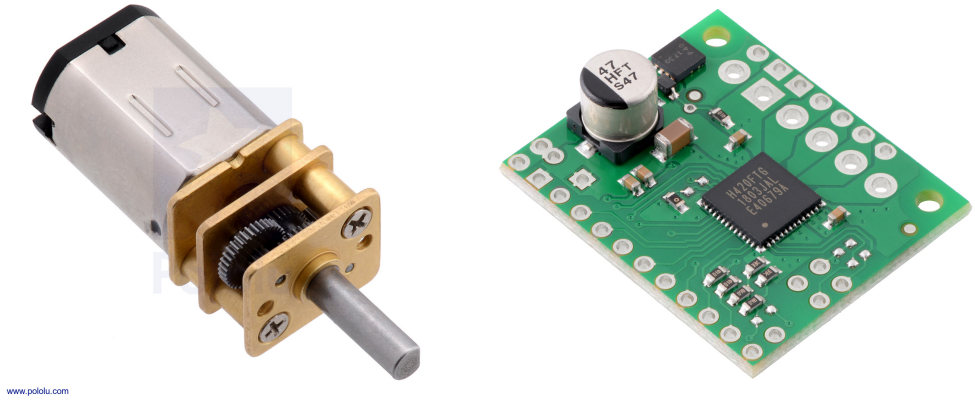

(a) Brushed micro motor. (b) Motor controller

Figure 2.34: Brushed motor placed on valves. (Images from www.pololu.com)

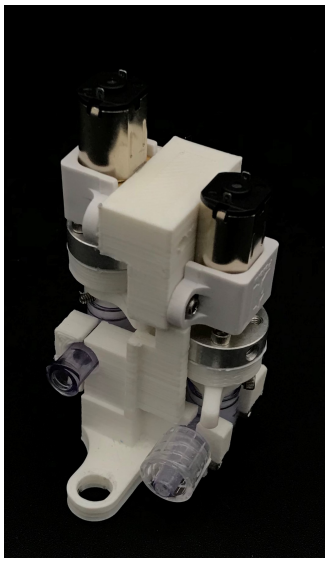

Figure 2.35: The prototype compact double-valve.

2.2.3 Results

The friction torque data for the low and high pressure ball valves having the same pressure on both sides of the valve are shown in Figure 2.36.

The torque required to turn the high-pressure valve was higher than the torque

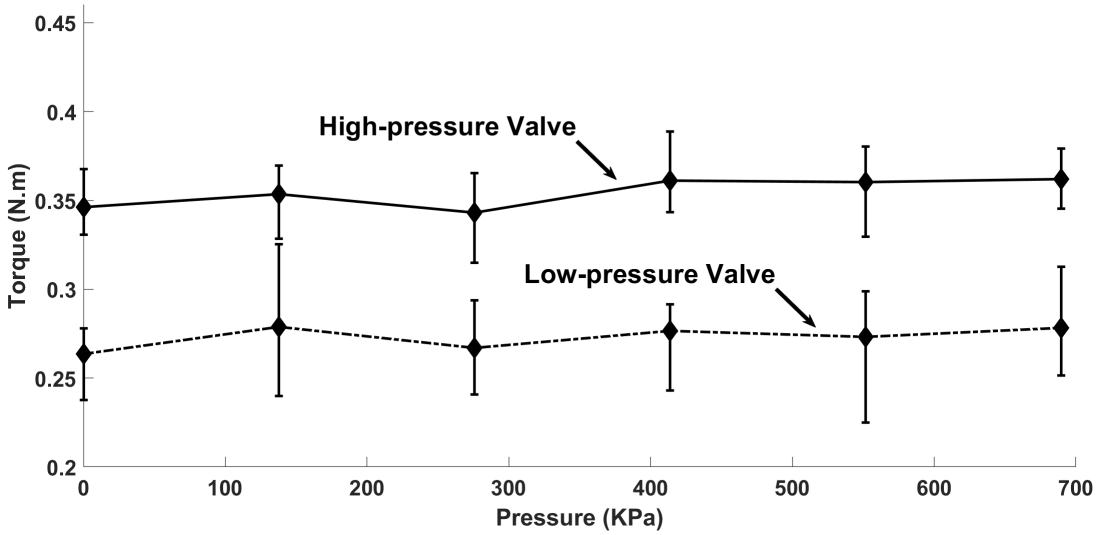

Figure 2.36: Torque required to turn the valve stem at different pressures for a high-pressure and low-pressure ball valve, when the pressure is the same on both sides of the valve. At each pressure, data is presented as the mean (markers) and the range (whiskers.)

required to switch the low-pressure valve. The torque was constant over the pressure since the force produced by the pressure cancels out.

The torque results for the ball valve when pressure was applied to only one side are shown in Figures 2.37 (low-pressure valve) and 2.38 (high-pressure valve). The torque increased with pressure because the ball is pushed against one of the O-rings.

Parameters, D_1 housing diameter and α O-ring stiffness, were used to fit the ball valve model to the experiment. Table 2.4 shows the results of this fitting.

Table 2.4: Estimated parameters using the least squares method to fit the data to the friction model shown in Equations 2.14 and 2.17.

	$D_1(mm)$	α
High-pressure valve	18.51	5.3×10^6
Low-pressure valve	18.73	5.3×10^5

The same experimental apparatus was used to test the butterfly valve. Figure 2.39

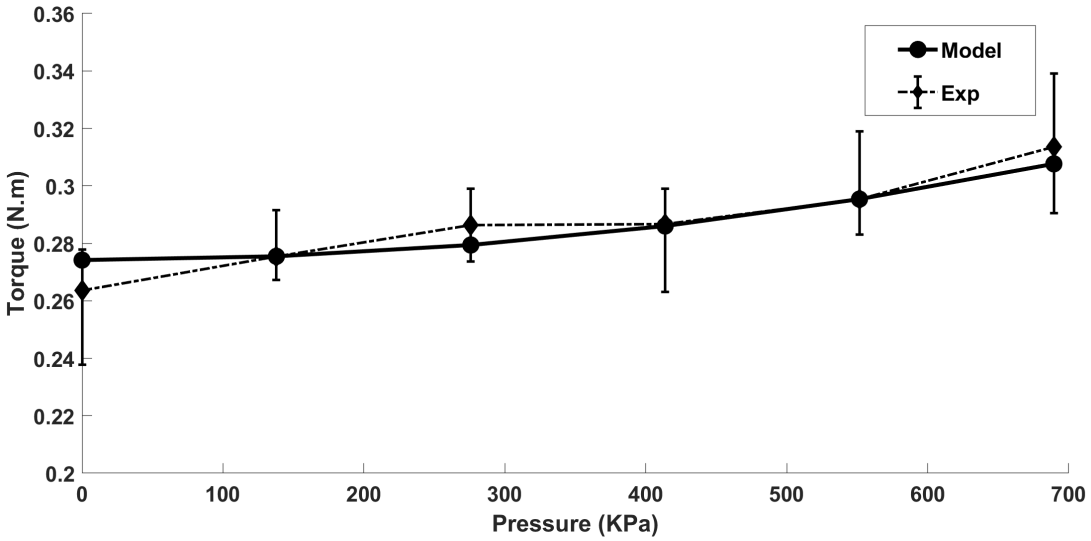

Figure 2.37: Torque for different pressures when the pressure only exists on one side of the low-pressure ball valve.

shows the torque required to switch the butterfly valve for the case of having the same pressure on both sides. Figure 2.40 shows the torque for the case of having pressure only on one side of the butterfly valve. The torque stayed consistent with pressure for both cases. The parameter d_2 (disc diameter) to be estimated for the butterfly valve, was found to be 12.86 mm.

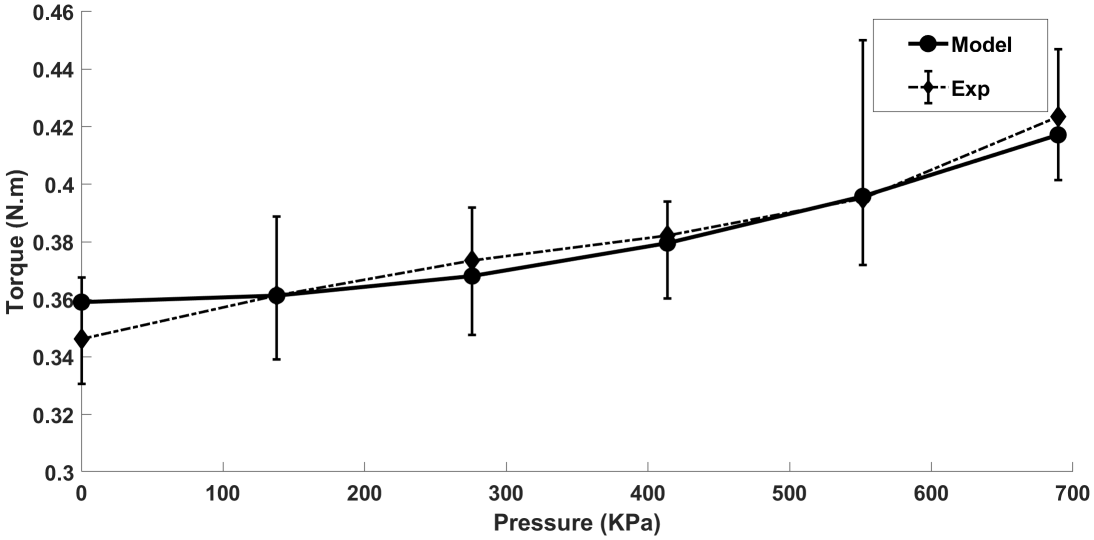

Figure 2.38: Torque for different pressures when the pressure only exists on one side of the high-pressure ball valve.

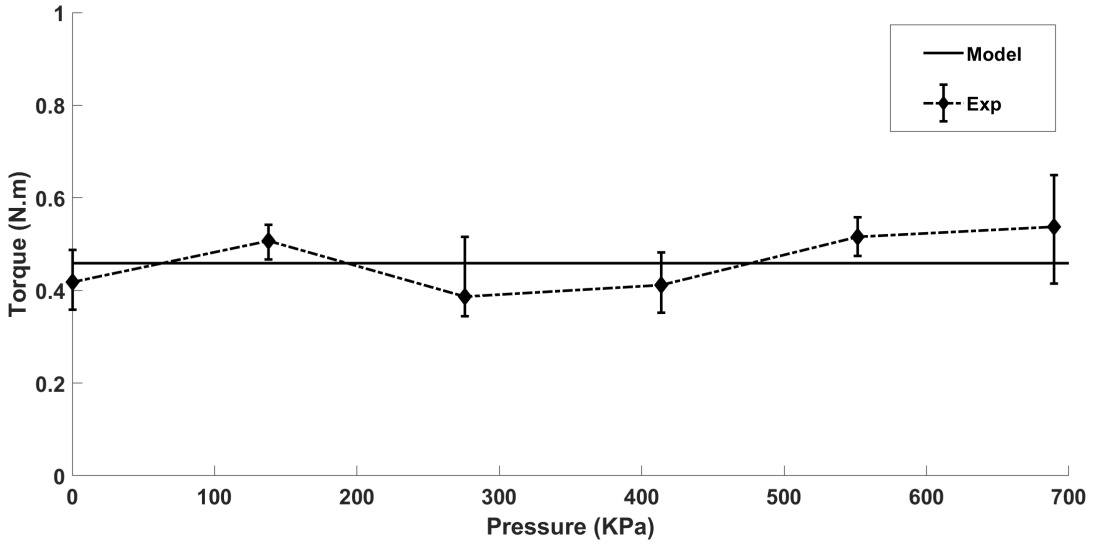

Figure 2.39: Torque for different pressures when the pressure exists on both sides of the butterfly valve. The whiskers show the range of data in five trials.

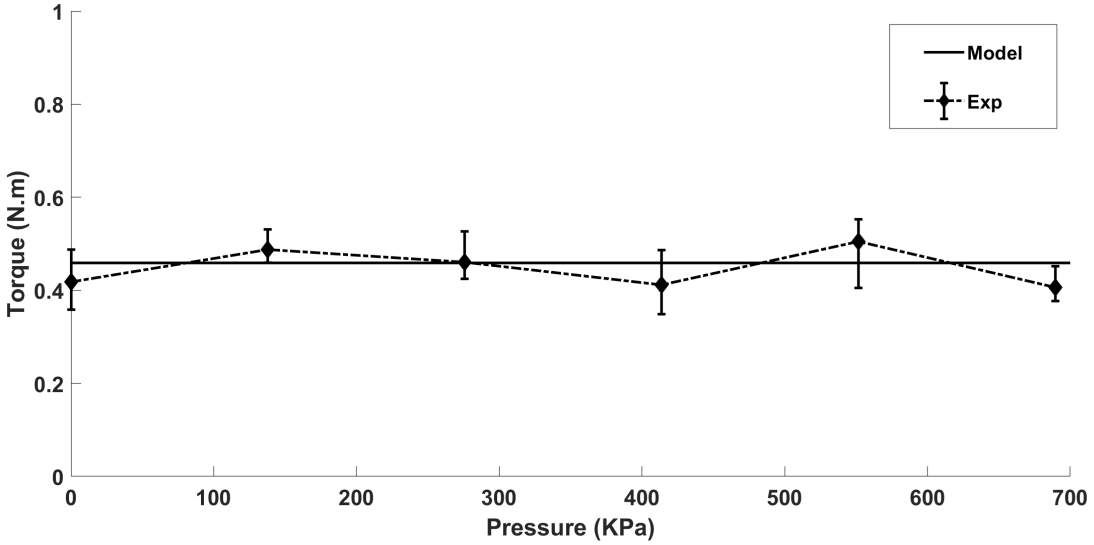

Figure 2.40: Torque for different pressures when the pressure only exists on one side of the butterfly valve.

The digital hydraulic transmission with four actuators requires eight valves. The energy required to switch the 8 butterfly valves and the ball valve was calculated using Equations 2.18 and 2.20 and is shown in Figure 2.41.

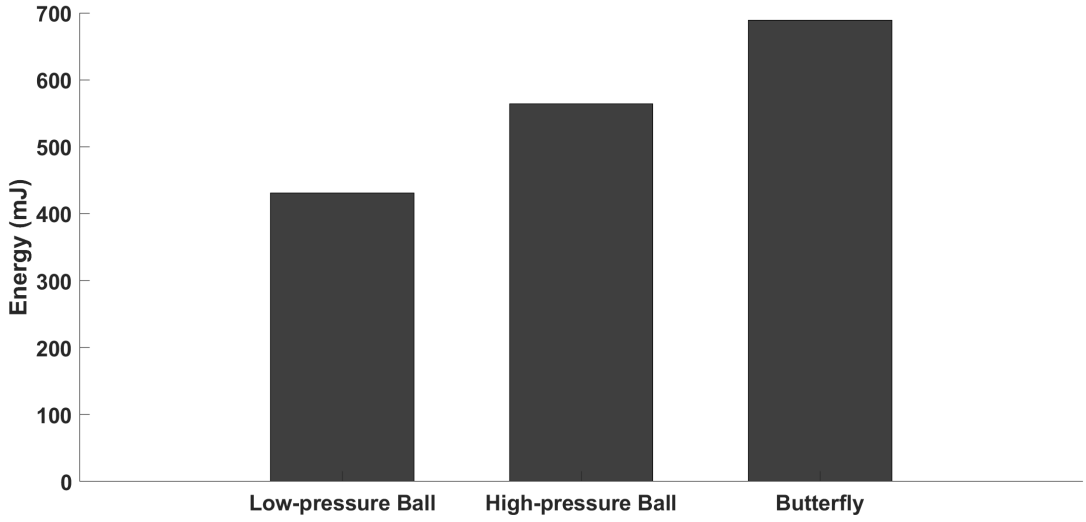

Figure 2.41: The energy required to switch the valves.

The friction torque-angle relations are shown in Figure 2.42 and 2.43. Zero degrees represents the closed position. The grey areas show the minimum to maximum recorded values in four repeated tests.

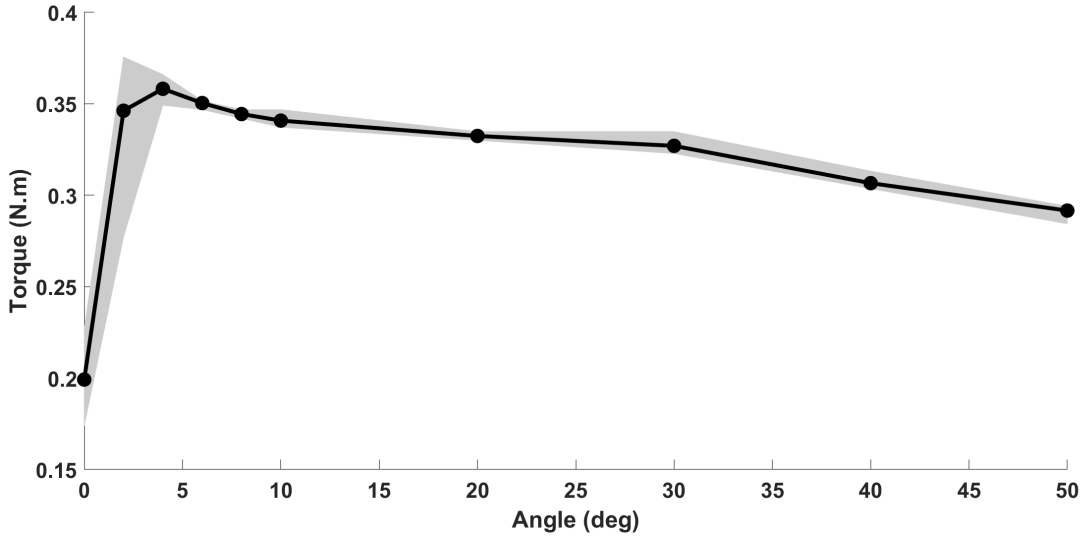

Figure 2.42: Friction torque vs. angle for the high-pressure ball valve.

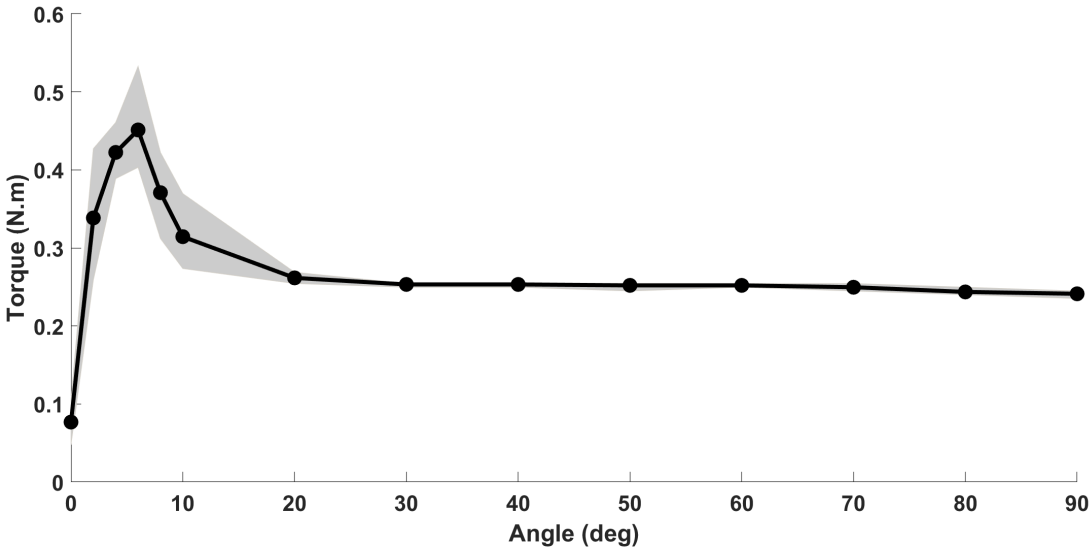

Figure 2.43: Torque vs. angle for the butterfly valve.

2.2.4 Discussion

Ideal valves for digital hydraulics must have zero pressure drop and low switching power consumption. Butterfly and ball valves were chosen for further consideration because they are zero pressure drop rotational valves. O-ring friction is the primary determinant of the amount of energy required to turn the valve between its open and closed states. The friction force for the O-ring around the stem was neglected since the diameter of the stem is small compared to the ball or disc and therefore, the friction force and torque were negligible.

Figures 2.36 and 2.39 show that the valve friction is constant with pressure when both sides of the valve see the same pressure. For the ball valve, when only one side sees the pressure, the valve friction increased with the pressure (Figures 2.37 and 2.38) because the ball was pushed against one of the O-rings, while for the butterfly valve, friction torque did not increase with pressure.

The model followed the experiment data with an acceptable level of accuracy, which means that the model can be used for design purposes. Two parameters, housing diameter and O-ring stiffness, were used to fit the ball valve friction model to the experiment data (Table 2.4). The squeeze ratio for the low-pressure ball valve (0.063) was larger than the ratio for the high-pressure valve (0.007); however, the torque for the high-pressure valve was higher since the O-ring material used in the high-pressure valve is 50 times stiffer the material used in the low-pressure valve O-rings.

The housing diameters measured with a digital calipers were in the range [18.6 18.8] for the low-pressure valve and [18.5 18.7] for the high-pressure valve. As shown in Table 2.4, the fitted housing diameter was 18.51 mm and 18.73 for the low and high-pressure valves respectively, both within the range of the actual valve. The stiffness value α for the high-pressure value is ten times higher than the low-pressure valve. The higher modulus of elasticity of PTFE for the high-pressure valve O-rings compared to the Buna-N low-pressure valve O-rings explain some of the difference with the rest accounted for by the different O-ring geometries in the two valves. The largest pressure differential over the valve exists when the valve is closed and drops to near zero as the valve opens because both ball and butterfly valves do not obstruct the fluid flow when fully open. Therefore, the model and experiment actuation torques measured in this study are the highest that will be seen by the valve. The motor used to actuate can be over-driven for

brief periods to attain the torque needed to open the valve the first few degrees. The torque to switch the butterfly valve is shown in Figures 2.39 and 2.40. The torque did not change with pressure in both cases since the friction force on the O-ring was not related to pressure on the disc. The O-ring squeeze ratio ϵ for the butterfly valve was 0.086, which was larger than the ball valves. The fitted disc diameter for the ball valve was 12.86 mm which is in the range of [10.92 16.51] that was determined by measuring the disc with a dial calipers. The energy required to switch 8 balls and butterfly valves is shown in Figure 2.41. The energy for the butterfly valve was higher because the friction force on the O-ring was higher due to its higher squeeze ratio. For the same squeeze ratio, geometry, and O-ring material, the energy for the butterfly valve would be lower than the ball valve since the distance that the squeezed O-ring travels is smaller for the butterfly valve (Equation 2.22).

$$DiscThickness < \frac{Ball\ Diameter \times \pi}{4} \tag{2.22}$$

The butterfly valve architecture has a small pressure drop in the open position due to the presence of the disc. However, the butterfly valve has lower switching energy compared to the ball valve because the friction force only exists for the few degrees around the fully closed position. This is a design trade-off; therefore, choosing the proper valve architecture will depend on the application.

Figure 2.44 shows the power needed during switching as a function of the switching time for the three valves. The butterfly valve tested in this study required the highest power. The data in Figure 2.44 can be used to specify the motor used to actuate the valve. Since the valves measured in this study were not optimized for friction, the required power could be reduced by custom designing a valve.

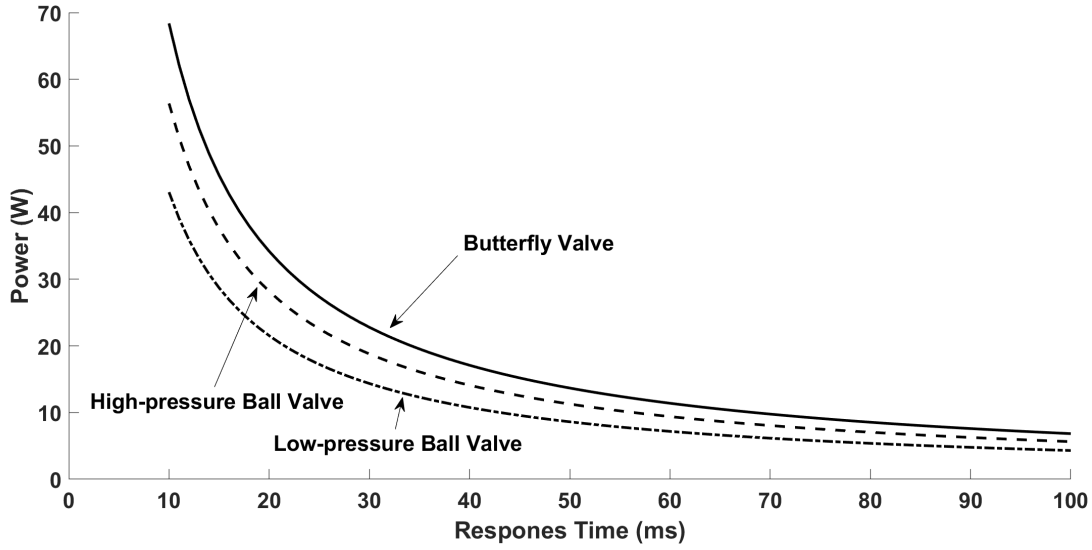

Figure 2.44: Power consumption of the valves for a switch.

The rotational kinetic energy of the ball or disc is negligible compared to the friction energy. Using the geometry parameters in Table 2.2 and 2.3 and assuming stainless steel for the material, the kinetic energy required for the ball or disc to rotate 90 degrees at 10 ms is less than 0.75 mJ.

The friction torque as a function of valve angle is shown in Figure 2.42 and 2.43. The difference between maximum torque and steady-state torque was higher for the butterfly valve. The contact between O-Ring and housing was removed after 6 degrees in the butterfly valve and it confirms the effect of O-Ring friction in overall switching torque. A lower difference between maximum torque and steady-state torque is seen in the ball valve compared to the butterfly valve since the O-Ring is in contact with the blockage over the switch. The maximum friction (stiction) is seen at 4 degrees in the ball valve. The hydraulic transmission discussed in Chapter **??** was assumed to be the application for the valve analysis in this study which requires valve state change in the valves to change the transmission ratio. While a high frequency of state changes is required in pulse width modulation (PWM) digital hydraulics, PWM is not considered in this application. An analysis of the possible wear of O-Rings is required in case of a high number of switches.

2.2.5 Conclusion

Digital hydraulic valves must have low pressure drop, fast response time, and low switching energy. Ball and butterfly valve architectures are appropriate choices for a digital hydraulic system because of their rotary actuation and low pressure drop in the open position. Rotary actuation is desirable since it is easier to seal and allows a more compact design. Analytical friction models can be used for design purposes as they proved to be good predictors of actual valve friction. Friction goes up with the ball valve pressure and if the valve is designed for high pressure, which means that portable hydraulic digital systems with small light motors should be designed to run at lower pressures. Butterfly valves take less energy to switch but have a small pressure drop due to the disc obstructing the fluid path when the valve is in the open position. A prototype with plug valves and brushed micro motors were built to evaluate the performance of the variable hydraulic transmission.

Chapter 3

Antagonist Hydraulic Transmission

3.1 Introduction

Power is characterized by its across and through variables. Transmission is the process of changing the ratio of these variables or the domain of the power. These variables are force and velocity in the mechanical domain and fluid pressure and flowrate in the hydraulic domain [65]. Backdrivability is the ability for interactive transmission of across and through variables between input and output [66]. Rigid cables can be used to transmit power between joints. Bowden cables use the movement of an inner cable within an outer sheath to transmit power in mechanical systems; however, the friction in Bowden cables varies for the bend angle, and they suffer from compliance, poor backdrivability, and high friction. Backdrivability and reasonable friction can be achieved using a push/pull control cable; however, only one transmission ratio can be reached by the cable transmission method. The device shown in Figure 3.1 is a body-powered wearable robot equipped with a push/pull cable with a transmission ratio of 1:1 that transmits the power between arms.[1]

A push/pull control cable has low friction and backlash but also a fixed transmission ratio. A hydraulic transmission adds the possibility of variable transmission ratios that

[1] Elbow orthotic project, Kimberly Gustafson, University of Minnesota, Mechanical Engineering undergraduate student.

can be utilized in the system using digital hydraulics [56, 67, 58].

Figure 3.1: Body-powered, push/pull cable, 1:1 arm rehabilitation device (designed and fabricated by K. Gustafson, University of Minnesota.)

Hydraulic devices produce considerable torque compared to the small size of the device. The fluid carries away the heat generated in the device and acts as a lubricant for the components. Flexible hoses, lightweight components, and variable transmission ratio in the system make the hydraulic transmissions a viable choice for robots designed to interact directly with humans. As discussed in Chapter 2, a novel rolling diaphragm cylinder has approximately the same low friction as a gap seal and commercial rolling diaphragm cylinder and zero leakage [68]. The novel aspect of this cylinder was that, unlike the commercial rolling diaphragm cylinders that are restricted to a 1:1 stroke to bore size ratio, our cylinder can be fabricated with any stroke length (Figure 2.6). This long-stroke rolling diaphragm (LSRD) cylinder is suitable for use in a passive hydraulic body-powered wearable robot (Figure 2.6b). Antagonist transmission provides

an opposing interaction between the input and output (Figure 3.2). A prior art study used commercial rolling diaphragm cylinders in an antagonist hydraulic transmission for a robot/human interaction application [50] that was part of a hybrid hydrostatic telepresence robot [5]. The cylinders used in this study had limited stroke lengths resulted in limited range of motion and low torque capabilities.

Figure 3.2: Antagonist transmission using paired cylinders.

In this chapter, we applied new LSRD cylinders in an antagonist hydraulic transmission, and measure the friction, stiffness, and dynamic properties of such a transmission.

3.2 Methods

3.2.1 Testbed

By pairing two cylinders against one another, the most basic concept of antagonist passive transmission can be shown (Figure 3.2). Using the same concept as the push/pull cable system (Figure 3.1), we can engage the two lever arms using hydraulic transmission to have a 1:1 transmission ratio.

The LSRD cylinders were used in the testbed due to their low friction and zero leakage. The rolling diaphragm cylinder cannot maintain reverse pressure since it would invert and cause the diaphragm to jam. The system needed to be pre-pressurized to prevent reverse pressure on cylinders and reduce the system backlash [50]. Three ways to preload the cylinders in the transmission were considered (Figure 3.3).

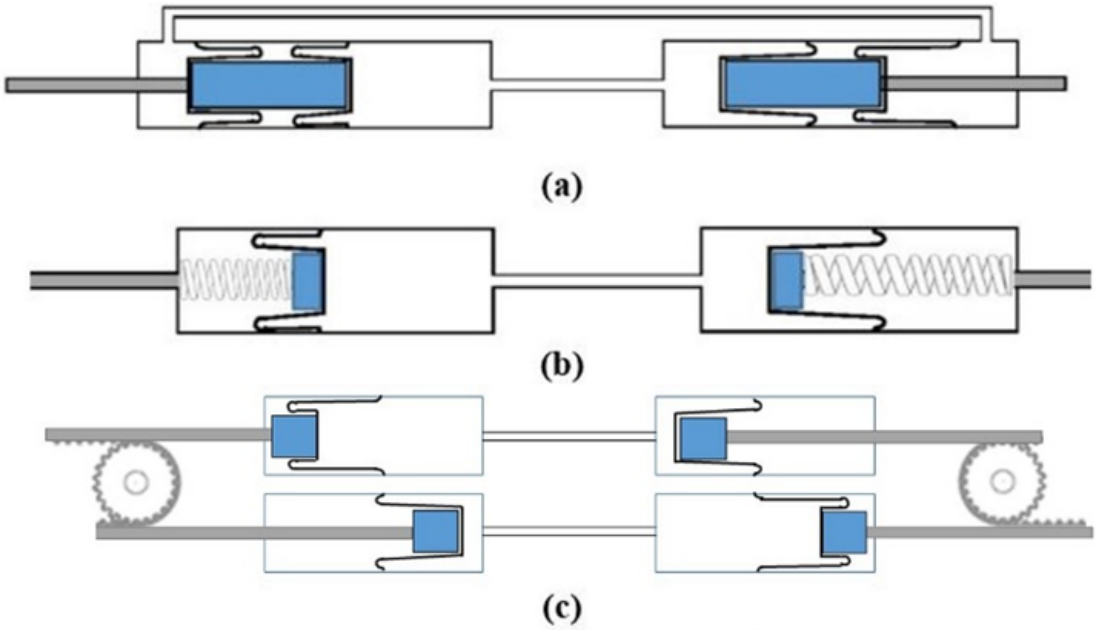

Figure 3.3: Three preload methods using rolling diaphragm cylinders.

Configuration (a) used two engaged double-acting rolling diaphragm cylinders for the transmission. With only two cylinders, the weight of this transmission was an advantage for wearable robotics. Configuration (b) used springs to preload the single-acting cylinders. This type was not a viable choice since energy loss in the springs reduces efficiency. Configuration (c) used a timing belt and pulley system to engage the two series of single-acting cylinders without springs for a rotary antagonist transmission. Configuration (c) was used for the passive transmission testbed studied here. Rotary shafts were placed on the input and output to implement quantitative tests on the transmission. Engaging two lever arms using the transmission without any valves made a testbed for evaluating friction, tracking, stiffness, impulse response, and step response of the system.

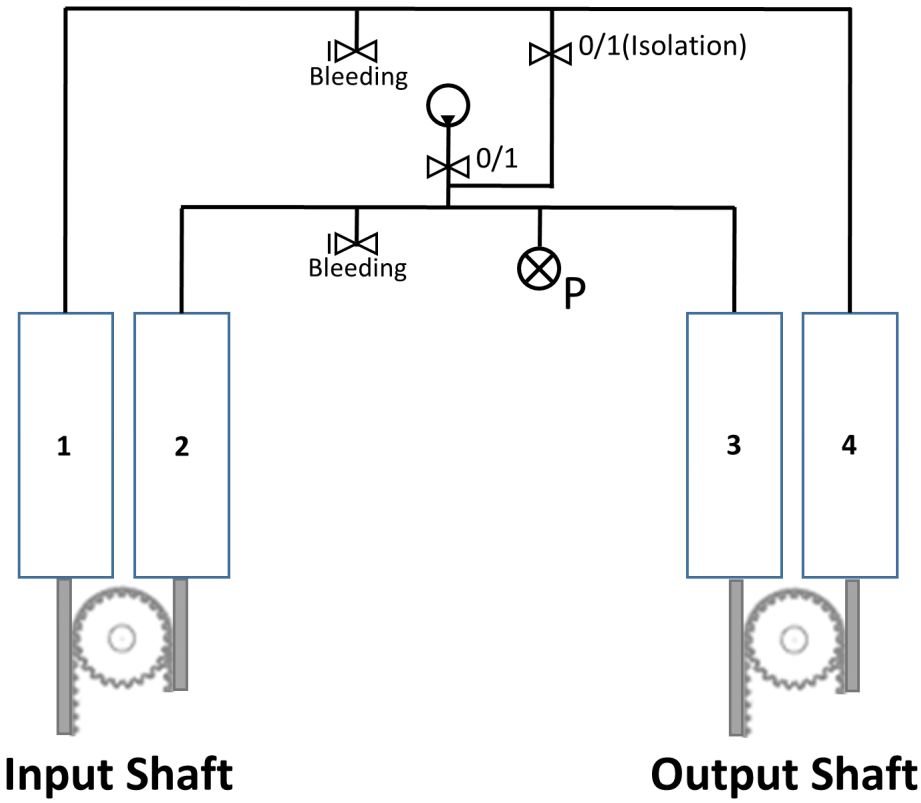

Figure 3.4: Antagonist transmission circuit.

Cylinders with the same bore size were used in the design. A hand pump was used to pressurize the system. System air removal was done using the bleed valves in the circuit. All the valves were closed to isolate cylinders 2 and 3 from cylinders 1 and 4. The transmission ratio between input and output was 1:1. The transmission ratio can be 1:-1 by connecting cylinders 3 to 1 and 4 to 2. There was no engagement between input and output in the transmission when the isolation valve was open.

An antagonist passive transmission was constructed for system testing (Figure 3.5). The cylinders had a 1.5-inch stroke length, and with 2-inch diameter pulleys, provided 90 degrees of rotation for the input and output shafts. The timing belts tighten by pre-pressurizing the cylinders since both cylinder rods move in the same direction (Figure 3.6). The angles on the input and output shafts were measured using potentiometers (Bourns, 6639S-1-103).

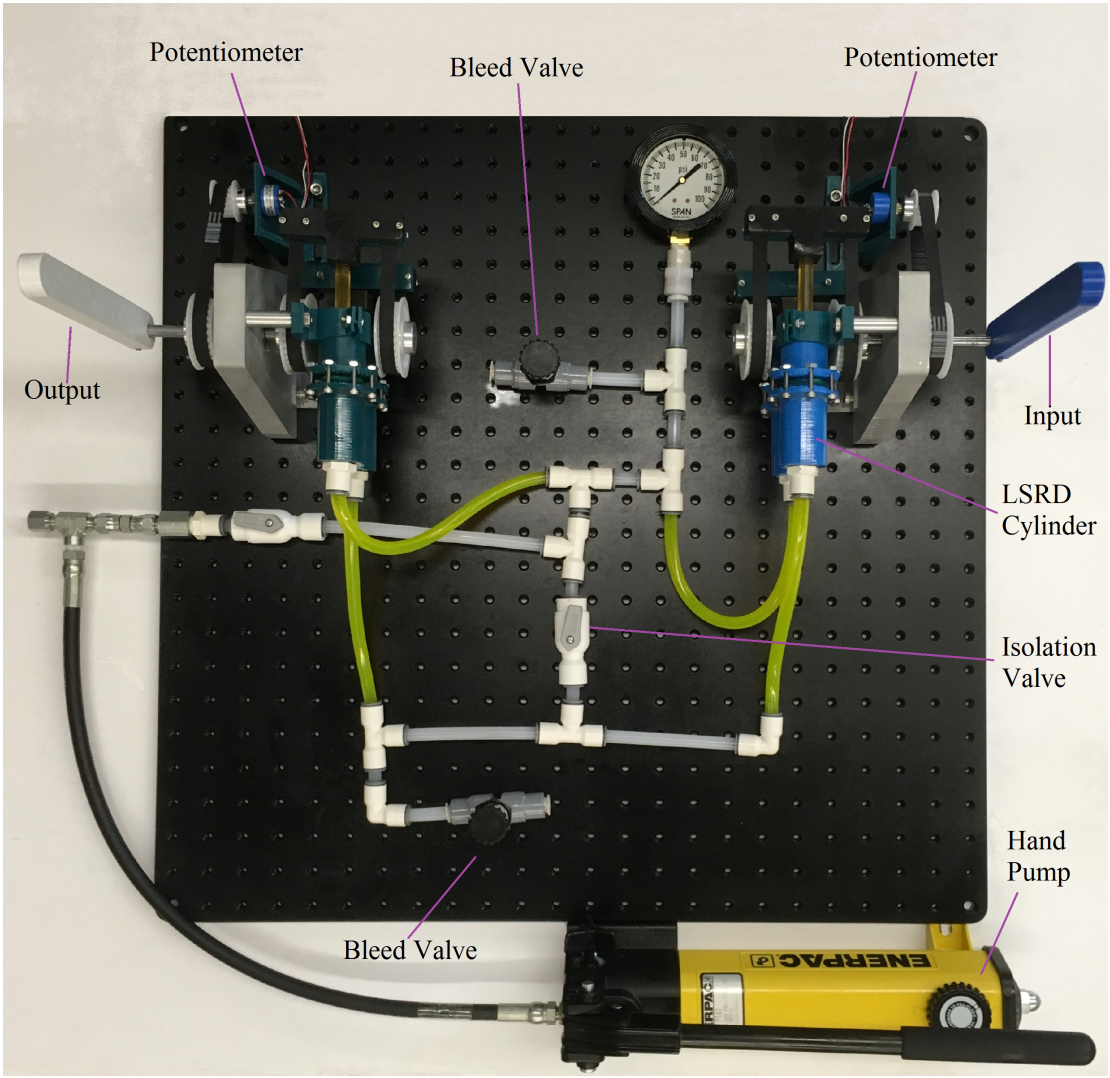

Figure 3.5: Hydraulic antagonist transmission testbed.

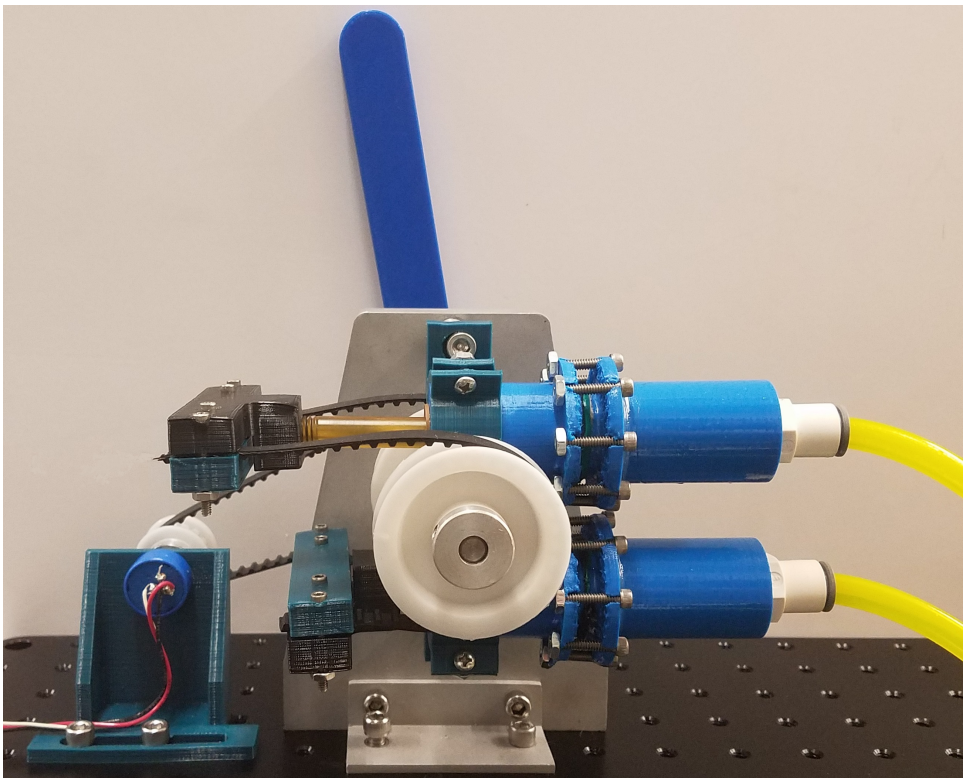

Figure 3.6: Using timing belts and pulleys to convert axial motion to rotary.

3.2.2 Evaluation Tests

Several tests were performed on the LSRD cylinders and the transmission device using the 1:1 transmission ratio configuration. The tests included friction, stiffness, tracking, impulse response, and step response. System tests were conducted at three preload pressures using mineral oil for the working fluid.

Friction

The friction test was performed using a custom-motorized test stand equipped with a linear force sensor (Mark-10, M5-200) coupled to the input shaft while the output shaft was unloaded (Figure 3.7). Stiction is the break-away torque when the output shaft starts rotating, and friction is the torque measured when the output shaft is rotating at a constant velocity. As discussed in Chapter 2, the friction and velocity are independent

for these cylinders at velocities lower than 2 mm/s.

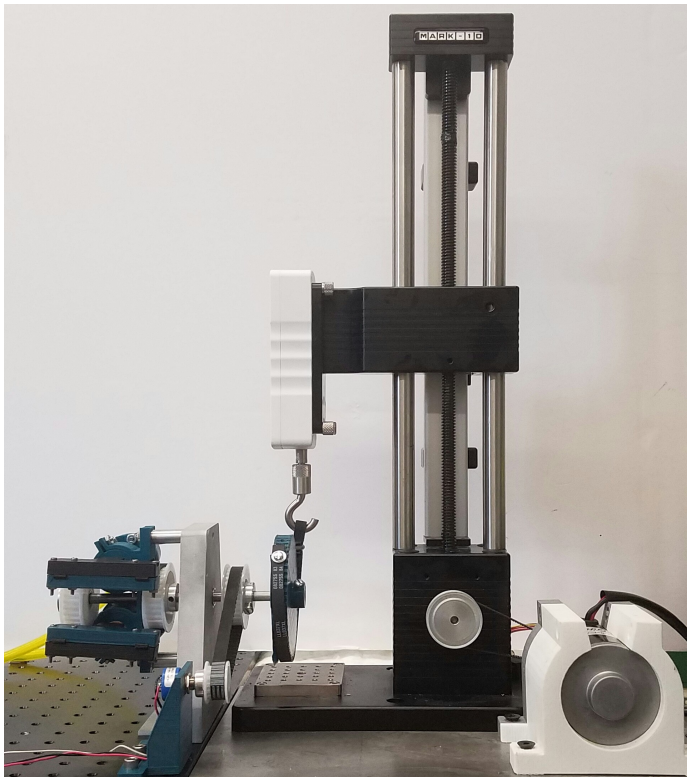

Figure 3.7: Motorized test stand equipped with a linear force sensor.

Stiffness

The stiffness of the transmission was measured by applying torque on the input shaft by a custom-motorized test stand and measuring the input shaft angle and torque while the output shaft was locked (Figure 3.7).

Tracking

Lever arms were placed on input and output shafts to demonstrate the backdrivability of the transmission (Figure 3.5). The output follows the input for a transmission ratio of 1:1, and the angle tracking can be evaluated. The input was moved at various velocities while measuring the input and output shaft angles.

Impulse and Step Responses

An impulse input was applied to the system using a hammer while the output shaft was locked to the force sensor. The input angle and output torque were measured. A torque step input was applied to the input shaft by releasing a weight with zero velocity from a pulley on the input shaft and locking the output shaft to the force sensor.

3.3 Results

3.3.1 Friction

The torque needed to overcome resistance in the transmission was measured. The friction was caused by the diaphragms, several timing belts, and bearings in the system. The friction test results on a single LSRD cylinder from Chapter 2 were used to differentiate these two friction sources. The torque was applying on the input shaft using a custom-motorized test stand and measured by the force sensor while monitoring the output angle. Figure 3.8 shows the friction torque in mN-m for several preload pressures. When the output shaft is stationary, the torque applied on the input shaft is stiction, and when it moves at a constant velocity, the input torque is friction.

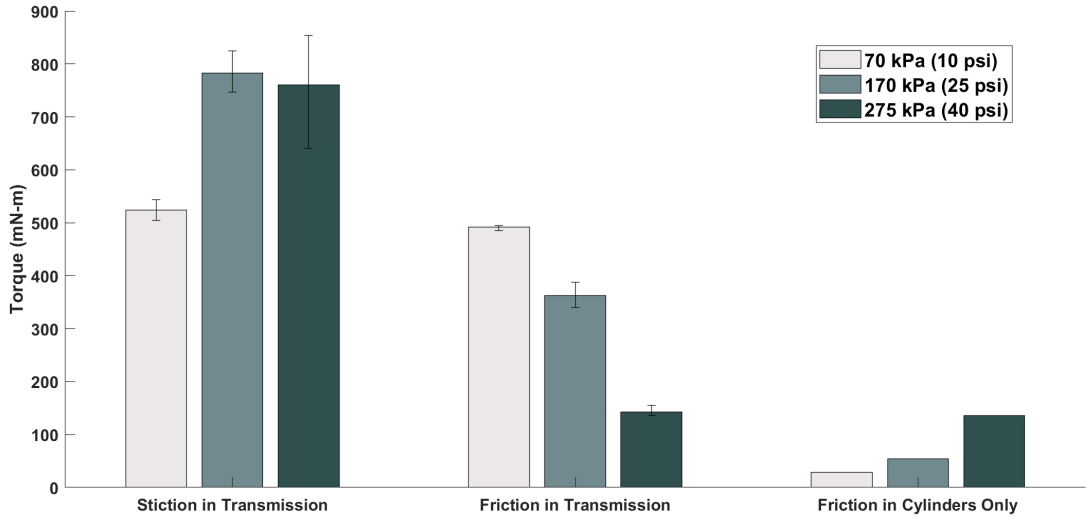

Figure 3.8: Stiction and friction of the device and single cylinders with preload pressure.

As shown in Figure 3.8, the transmission friction decreases with pressure since the system stiffens. Unlike the friction, the same pattern was not seen for stiction.

3.3.2 Stiffness

Figure 3.9 shows the stiffness of the system in different preload pressures. The transmission stiffness increased with preload pressure in cylinders.

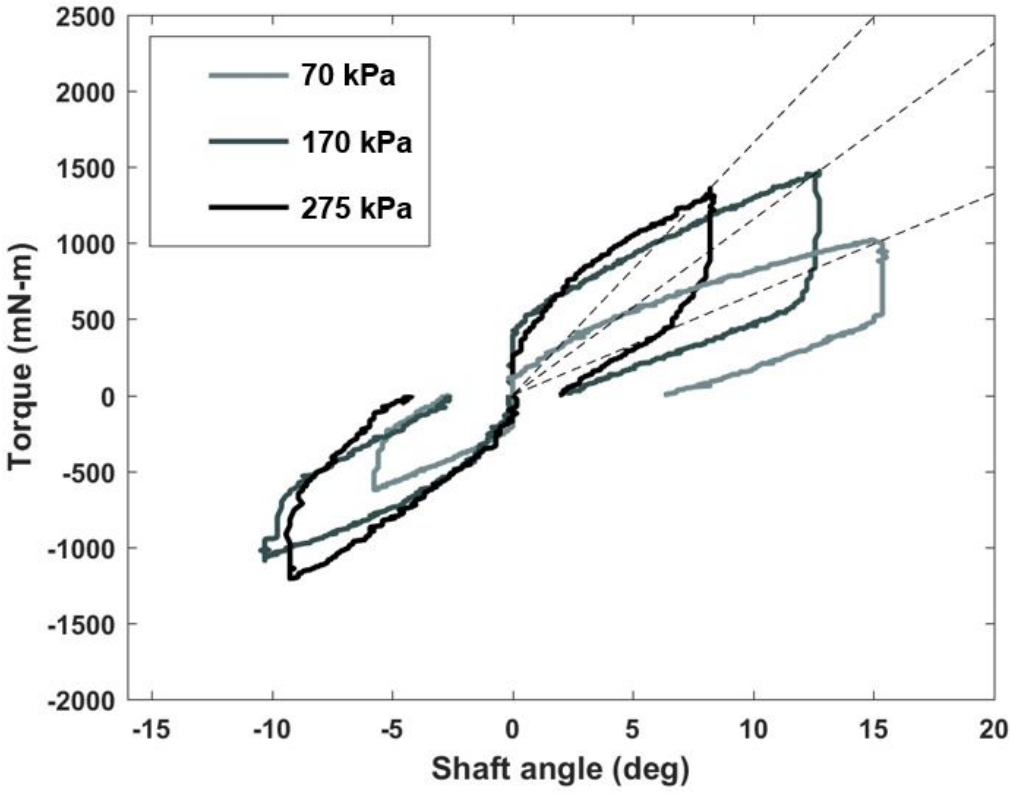

Figure 3.9: Transmission stiffness with preload pressure.

The stiffness for 275 kPa preload pressure was 166 mN-m/deg. The input shaft angle was monitored in this test; therefore, the vertical line at zero shaft angle in the stiffness plot shows the stiction for the input shaft. Stiction is 119.8, 453.5, and 276.7 mN-m for 70, 170, and 275 kPa respectively. Stiction was 524, 783, 760 mN-m for 70, 170, and 275 kPa in the friction test while the output shaft was locked. In both cases,

the highest stiction was seen at 170 kPa.

3.3.3 Tracking

The unloaded input arm was manipulated at various speeds to evaluate the backdrivability of the transmission. Figure 3.10 shows the unloaded output tracking the input over time for several preload pressures. Figure 3.11 shows the root-mean-square error of the output tracking the input illustrating better tracking at higher preload pressures.

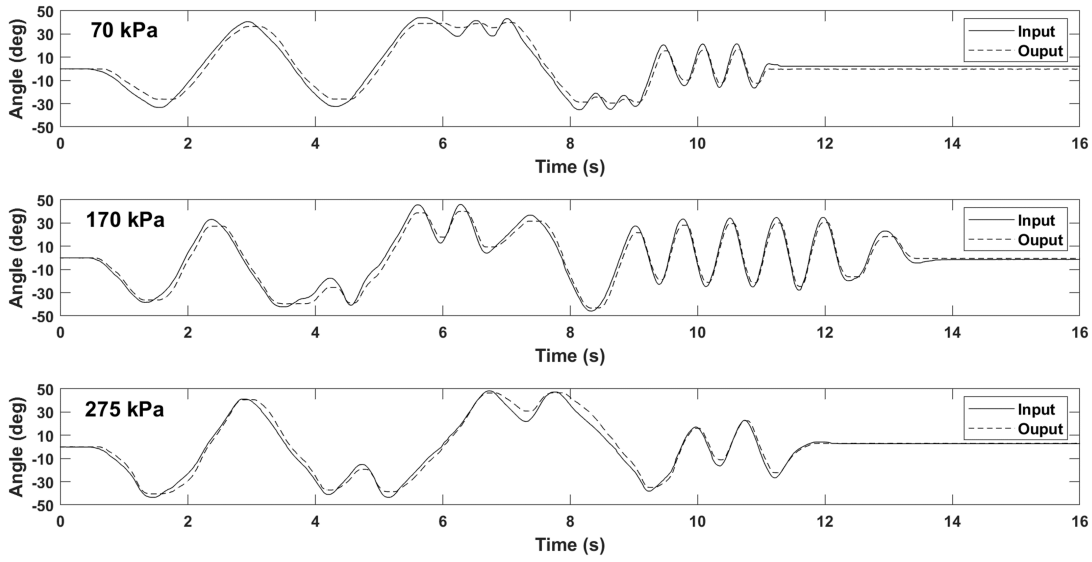

Figure 3.10: Output tracks the manipulated input over time.

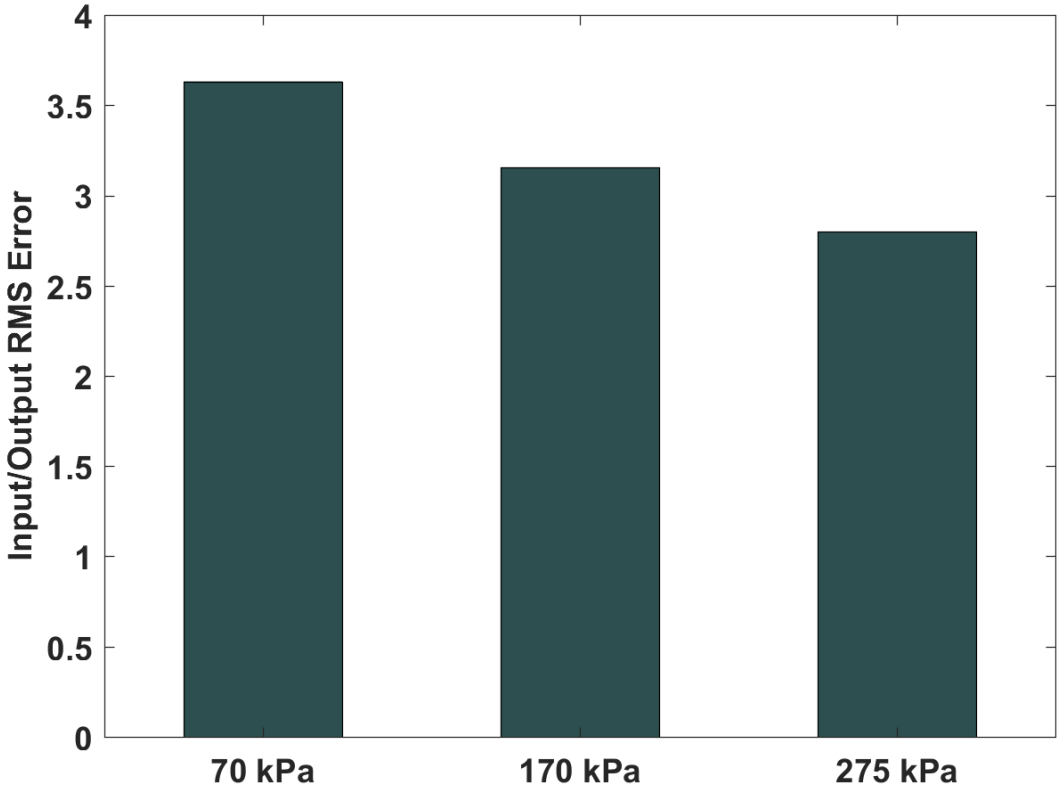

Figure 3.11: The RMS error of the output tracking the input at different preload pressures.

3.3.4 Impulse and Step Response

The output torque response to a torque step input is shown in Figure 3.12 for several preload pressures. Figure 3.13 shows the input shaft angle response to the same torque step input.

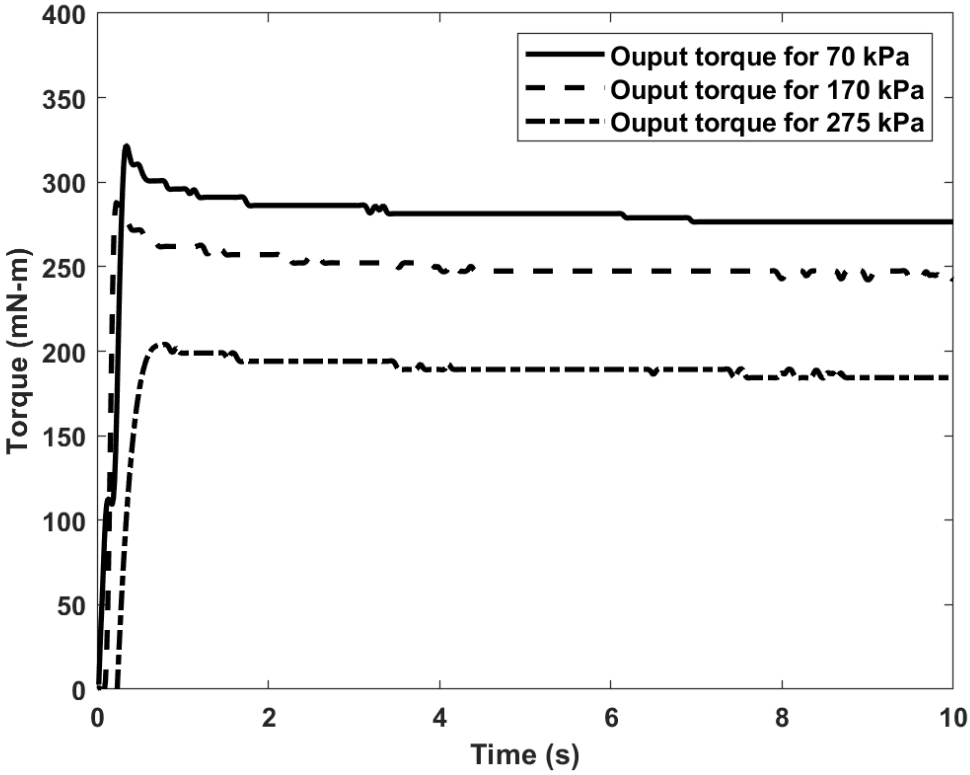

Figure 3.12: Output torque for 1100 Nm-m step torque input.

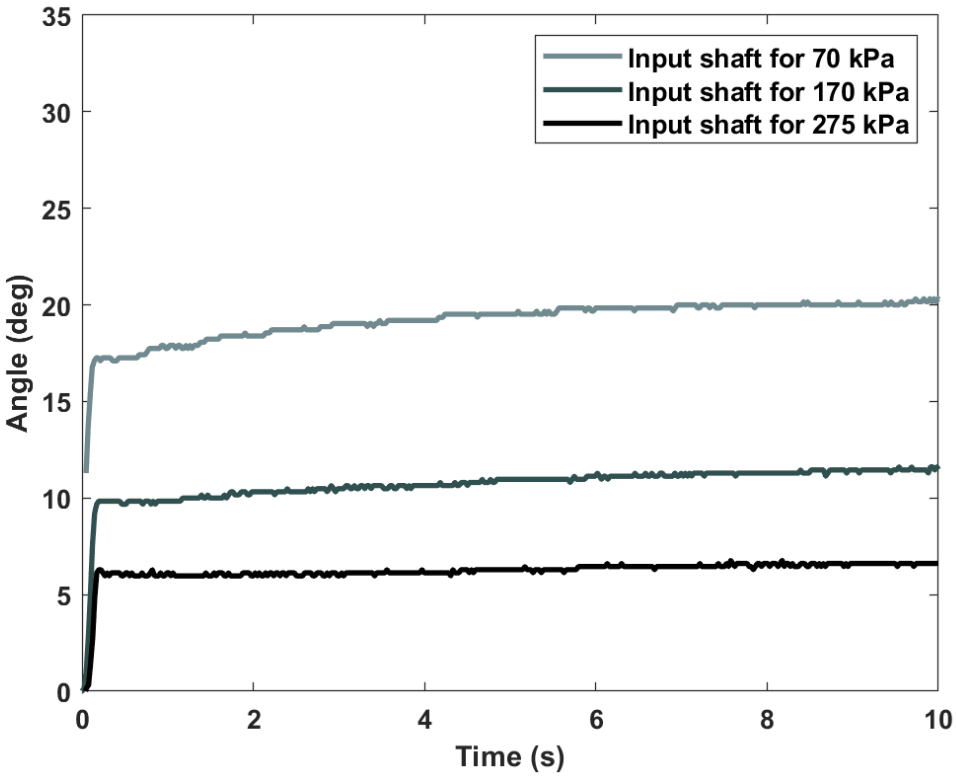

Figure 3.13: Input shaft angle for 1100 mN-m step torque input.

Smaller input angle changes were seen in higher pressures. It shows that the system was stiffer at higher pressure; so that under the condition where the output shaft was locked, the input shaft moved less when subjected to an impulse or step change in torque. The hammer impulse response is shown in Figure 3.14. Higher power transmission can be seen in higher pressures because the system was stiffer.

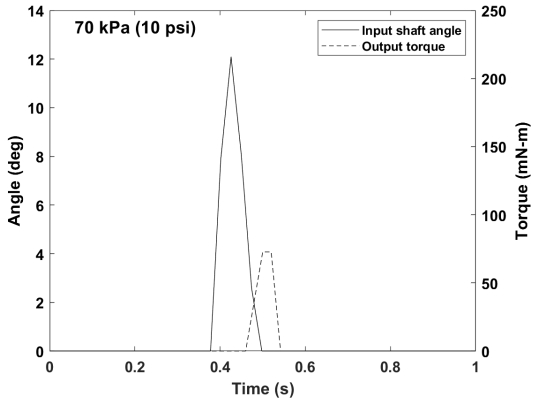

(a) Impulse response at 70 kPa.

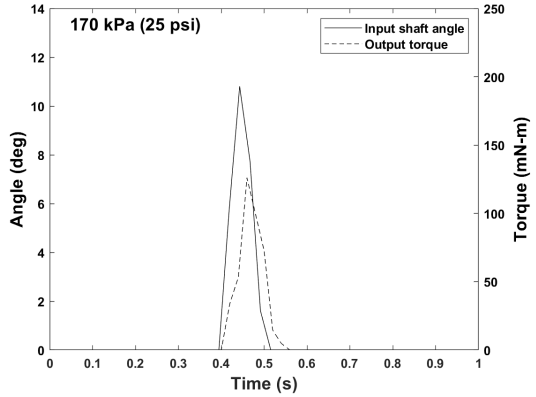

(b) Impulse response at 170 kPa.

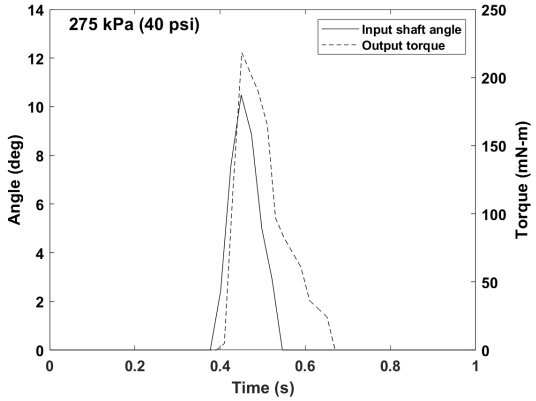

(c) Impulse response at 275 kPa.

Figure 3.14: Input shaft angle and output torque for a hammer impulse input

3.4 Discussion

Friction in a single LSRD cylinder has been measured, and the equivalent value for four cylinders being used in the transmission device was between 29 to 136 mN-m for three pressures (Figure 3.8). With the device testing setup, the timing belts get tighter at higher pressures and decreases the friction in the system [69]. Friction in the device approached the friction in cylinders subjected to higher pressures. At 275 kPa, these values were substantially close to one another, suggesting that this pressure is appropriate for the transmission device use. Stiction seen in this test was the torque needed in input shaft to move the output shaft. The stiction in Figure 3.9 can be seen in a vertical line when the angle is zero and torque is increasing, and it was the required torque to move the input shaft and was less than the stiction in the friction test. This discrepancy is attributed to the fluid and timing belts that transmit the input movement to the output. The stiffness increased from 66 to 166 mN-m/deg when the pressure was raised from 70 kPa to 275 kPa. The increase in stiffness resulted from the timing belts, which were stretched, and therefore stiffer at higher pressures. The output followed the input manipulation (Figure 3.10). Poor tracking can be seen at lower pressures than 275 kPa. Hysteresis is observed at 70 and 170 kPa when the input arm was at rest after manipulation; however, the output angle was different from the input angle. At 275 kPa, shaft angles matched during manipulation, which demonstrates low hysteresis for this pressure. The output shaft was engaged to a stationary force sensor in the step response test. It led the resistance torque to be in the stiction region and not friction. Since the stiction has been seen greater at higher pressures, the output torque response to a torque step input shows higher torque transmitted in lower pressures. Higher power is expected to be transmitted at high pressures for a moving step response test setup. The input shaft angle was lower for higher pressures in the step response test, and it shows that the system stiffens at higher pressures (Figure 3.13). In the impulse test, for the same input shaft rotation, higher input torque was needed at higher pressures, and it caused higher output torque (Figure 3.14). Time delay in impulse decreased from 82.4 to 14.0 ms when the pressure was raised from 70 to 275 kPa. The effect of the bulk modulus is not evaluated since the mineral oil bulk modulus change from 70 to 275 kPa is negligible [70].

3.5 Conclusion

LSRD cylinders were used in an antagonist passive hydraulic transmission. Several tests were conducted to evaluate the dynamic performance of the LSRD cylinders and the antagonist transmission device. Commercial rolling diaphragm cylinders cannot have a stroke to bore ratio greater than one. Using LSRD cylinders gives the input and output shafts 90-degree rotation capability with 2-inch pulleys compared to 60 degrees using commercial rolling diaphragm cylinders with the same bore size. Since no limitation exists regarding the stroke length of the LSRD cylinders, the rotation range can be increased using longer stroke cylinders or smaller pulleys based on the application. LSRD cylinders can retain long diameter pulleys for higher torque while still attaining long angular displacement. The tests demonstrate the performance of LSRD cylinders for applications that need longer stroke lengths. The friction of the device is comparable to the friction caused by the cylinders at higher pressures because the system stiffens and timing belts tightens. The friction of 155 mN-m and stiffness of 166 mN-m/deg were measured for the device with 275 kPa preload pressure. The output shaft tracks the input manipulation better at higher pressures, and at 275 kPa, the hysteresis approaches zero. Step and impulse tests demonstrate system fast behaviors and show acceptable performance at 275 kPa preload pressure. The performance of the transmission device in several tests shows that 275 kPa (40 psi) of preload pressure is needed for satisfactory performance. There are full elastomer commercial RD cylinders with longer stroke length, which has a 170-kPa pressure limit. The performance of the 170 kPa preloaded system shows that these commercial cylinders are not appropriate to use in this device, and cylinders with pressure limits are needed. The performance can be improved by substituting the 3D-printed cylinders used in the prototype transmission with aluminum versions to increase volume efficiency. This device can be used for different applications in robotics, from passive wearable robots to telepresence robots. This fixed transmission ratio can be made variable by adding on/off valves to the device to control the cylinders' connection.

Chapter 4

Variable Hydraulic Transmission

4.1 Introduction

A benchtop hydraulic transmission device was described in Chapter 3 for an antagonist hydraulic transmission. Long-stroke rolling diaphragm (LSRD) cylinders were used in the device, offering low friction and high stroke length, which allow the transmission to have a smooth and high-bandwidth movement in an increased range of motion. Adding a variable transmission between joints enables the system to have a wide range of speeds and to operate close to the peak power and efficiency [65]. Variable power transmissions can be continuous using variable radii pulleys and a belt or using a hydrostatic transmission or discrete using digital hydraulics.

4.1.1 Mechanical Variable Transmission

Variable transmission can be continuous (CVT) or discrete (DVT). Rotary mechanical CVTs usually contain two actuated variable radii pulleys and a belt (Figure 4.1). Speed or torque in the output can be controlled by changing the input and output radii by bringing the walls of the tapered-diameter pullley closer together or further apart [9]. A high normal force between belt and pulley is needed to prevent slip between them, which reduces the efficiency of the CVT [71]. Discrete hydraulic transmissions were used in wave energy converting [72]. A continuously variable transmission (CVT) was developed to maintain the speed of the generator of a wind energy converter by controlling the transmission ratio. The energy loss in a CVT was significantly reduced using a genetic

speed ratio control algorithm [73]. A mathematical model of the transmission through a steel belt and V-belt type continuously variable transmission was developed [74, 75]. A digital manifold with multi-chambered cylinders were used to vary the output force during a wave [76]. The losses in a hydraulic transmission used for tidal energy converting from valve loss to compressibility losses were modeled in a study [77]. Rotary mechanical DVTs have a set of discrete transmission ratios and use shifting to change the ratio. An example is a manual transmission in an automobile.

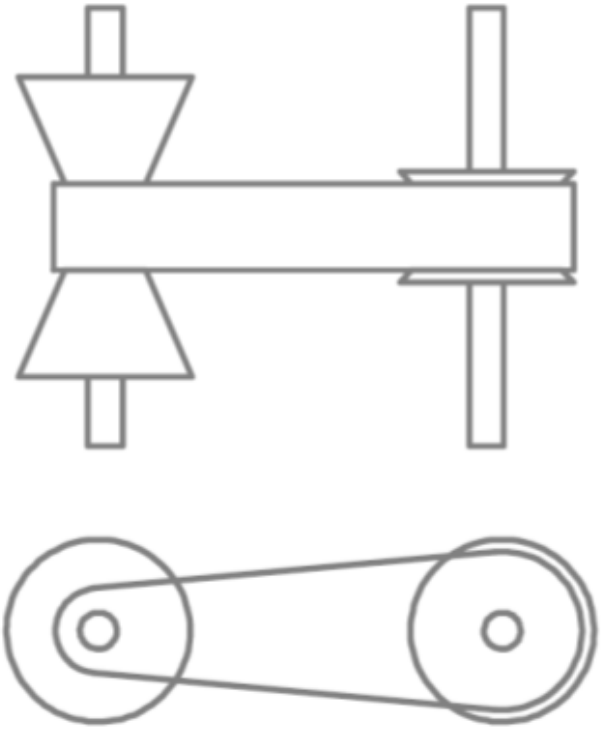

Figure 4.1: Continuously variable transmission.

Rigid cables can be used to transmit the power between joints. Bowden tension cables use an inner cable's movement within an outer sheath to transmit the power in mechanical systems. The friction in Bowden cables varies with respect to the bend angle.

Additionally, they suffer from poor backdrivability, high friction, and nonlinear behaviors. Backdrivability and reasonable friction can be achieved using a push/pull control cable; however, only one transmission ratio can be reached by the cable transmission method (Figure 3.1). The device shown in Figure 3.1 is a BPWR with a transmission ratio of 1:1 that transmits the power between left and right arms.

4.1.2 Variable Hydraulic Transmission

Hydraulic fluid power systems are well known for their high power density [78, 79]. Hydraulic fluid power systems can reach the same force and power level as electromechanical systems with relatively lighter weight [80]. The fluid carries away the heat generated in the device, and acts as a lubricant for the components. Hydraulic devices produce considerable torque compared to the small size of the device. Flexible hoses, lightweight components, and the variable transmission ratio in the system make hydraulic transmissions a viable choice for robots designed to interact directly with humans. Hydraulic actuators have high stiffness and small position error [81].

Hydrostatic transmissions are used to transmit rotary power from an input to an output. The transmission ratio varies continuously in a hydrostatic transmission, which can operate close to the peak efficiency. However, the overall efficiency is less than a mechanical gearbox. A variable swashplate piston pump leaks, which lowers the efficiency and therefore the system cannot be closed because the lost fluid needs to be replaced. Moreover, the transmission's dynamic contribution needs to be considered in hydrostatic transmissions since the transmission is compliant due to the compressibility of the fluid [82]. Figure 4.2 shows a hydrostatic transmission in which the input drives a swash plate pump. The swashplate can vary the pump's flow from zero to maximum and change the flow direction. The hydraulic motor at the output converts the energy of the flow to a rotary output motion. Therefore, the speed at the output can be controlled by the pump swashplate angle that changes the amount of oil delivered by the pump.

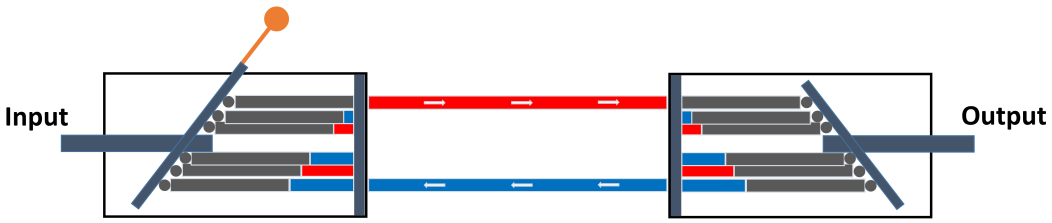

Figure 4.2: Hydrostatic transmission.

A mathematical model for losses in a variable hydrostatic transmission was provided in a study [83]. This model has optimized the performance of the hydrostatic transmission for off-the-road vehicles. An energy-saving hydrostatic transmission was suggested in another study [84]. The efficiency of the system goes down with decreasing the pressure and the volume of the chambers [84]. The system pressure needs to be limited for interaction with the human body, and wearability requires a small size. Therefore, the hydrostatic transmission is too inefficient to be used in small-scale applications like BPWR. High efficiency and small-scale variable transmission are needed to be used in wearable robots.

4.1.3 Digital Hydraulics

Digital fluid power is the controlling of system output using hydraulic or pneumatic components that are coupled to the system with switching valves. A digital fluid power system can be arranged in two configurations. One uses a parallel connection of several valves to have a certain number of discrete outputs, while various valves are used to split the flowrate (Figure 4.3). There is no need to switch components on or off to maintain a specific output value. Figure 4.4 shows the other branch of digital fluid power, which uses continuous pulse width modulation to have infinite output values. Fast and continuous switching is needed to maintain any output value. Although the output can get to any value, the valve response time can limit the smallest or largest possible duty cycles [56].

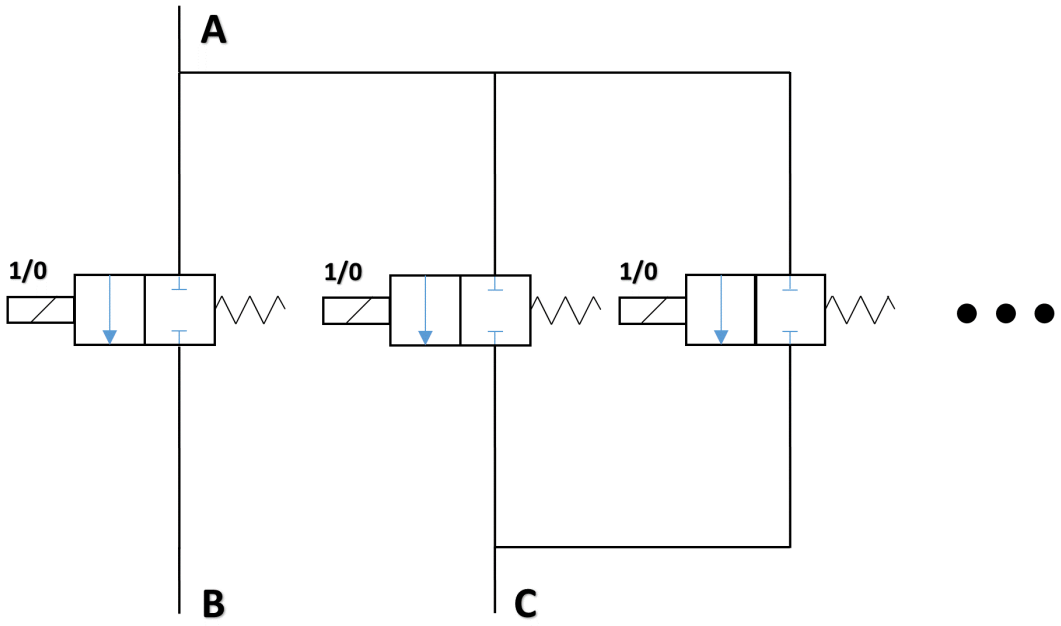

Figure 4.3: Digital fluid power circuit using parallel connection.

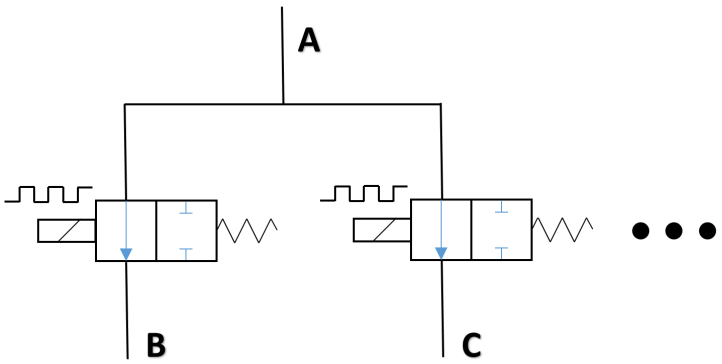

Figure 4.4: Digital fluid power circuit using continuous pulse width modulation.

In a parallel connection, the system's flowrate is the sum of the flow rate of the open valves. Two factors determine the output flow. The first factor is the number of parallel connections N, and the second one is the relative flow capacities of the valves, known as coding of the valve (valves orifice diameters). The system has 2^N output values, and

the number of outputs depends only on the number of the parallel connections N and not the coding of the valve. Based on the coding of the valves, some of the outputs can be the same [56].

It is possible to have a fast opening from a 0 percent to 100 percent flowrate in parallel connection since the time required for this opening depends only on individual valves' response time. In other words, opening ten tiny valves with the area of 10 mm^2 and response time of 10 ms takes only 10 ms, while opening one large valve with the area of 100 mm^2 takes longer. Having redundant transmission ratios allows high fault tolerance in parallel connections. Several parallel components can work to compensate in case of a valve failure and result in the same transmission ratio. The transition from one state combination to another requires switching of several valves can cause a high-pressure peak in a parallel connection system [56]. Flow losses in the valves and hoses and compressibility are the most critical losses in these systems. Compressibility losses occur whenever a valve switches the chamber pressure line between high pressure and low pressure [67].

A variable transmission can be achieved using a digital hydraulic cylinder based on the digital fluid power parallel connection. An array of switched cylinders is one example of digital hydraulic actuators, as shown in Figure 4.5a. A multi-chamber cylinder, a more compact solution, is shown in Figure 4.5b. Four chambers can deliver 16 unique negative or positive force values in the output. The number of force values is P^m, where P is the number of pressure supply lines and m is the number of chambers [56].

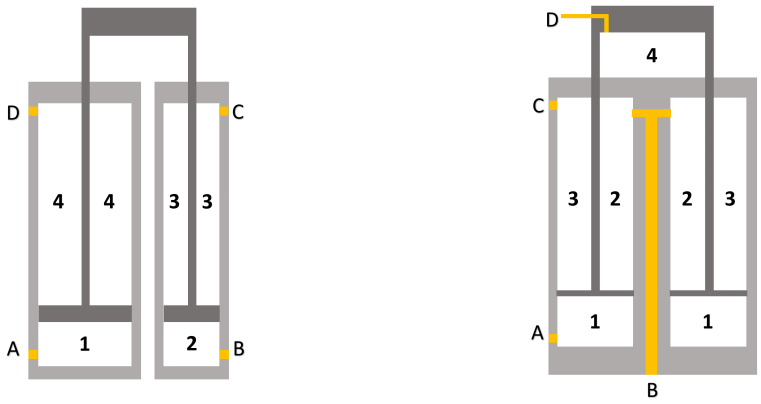

(a) Array of cylinders.

(b) Multi-chamber cylinder.

Figure 4.5: Digital hydraulic actuators

4.1.4 Proposed Variable Hydraulic Transmission

Figure 1.2 shows the proposed hydraulic transmission for a BPWR. This device connects multiple joints to transmit power produced by the patient's strong segments to the stroke-affected ones.

Figure 3.4 shows the hydraulic circuit of the transmission equipped with two cylinders on each joint. A transmission ratio of 1:1 between input and output joints was achieved by pre-pressurizing the system using a hand pump and closing the isolation valve.

Having a certain number of discrete transmission ratios is feasible using a digital hydraulic concept. Digital fluid power is controlling of system output using hydraulic or pneumatic components that are coupled to the system with switching valves. A digital fluid power system can be arranged in two configurations. One uses a parallel connection of several valves to have discrete outputs, and the other uses continuous pulse width modulation to maintain an infinite output value [56].

A discrete variable transmission based on the concept of digital hydraulic was studied in [58] using commercial rolling diaphragm cylinders. 37 different transmission ratios are reached using 6 cylinders. Using three way-two position solenoid valves caused an inefficient pressure drop in this system. Furthermore, the short stroke rolling diaphragm cylinders used in the study have limited the performance range.

In this chapter, a discrete variable transmission equipped with long-stroke rolling diaphragms and two way-two position on/off valves is proposed and evaluated.

4.2 Methods

4.2.1 Design of a variable hydraulic transmission

The digital transmission used several linear to rotary actuator packages that each contained two cylinders, timing belts and a multi-diameter pully (Figure 3.3). All the pulleys in input/output were connected to the input/output shaft, which allowed every cylinder to affect the transmission ratio. Using two on/off valves for each of the cylinders made it possible to have the variable transmission ratio in the system. As shown in Figure 4.6, every cylinder can be either connected to the common closed manifold or the reservoir. Cylinders with different bore sizes increase the number of transmission ratios.

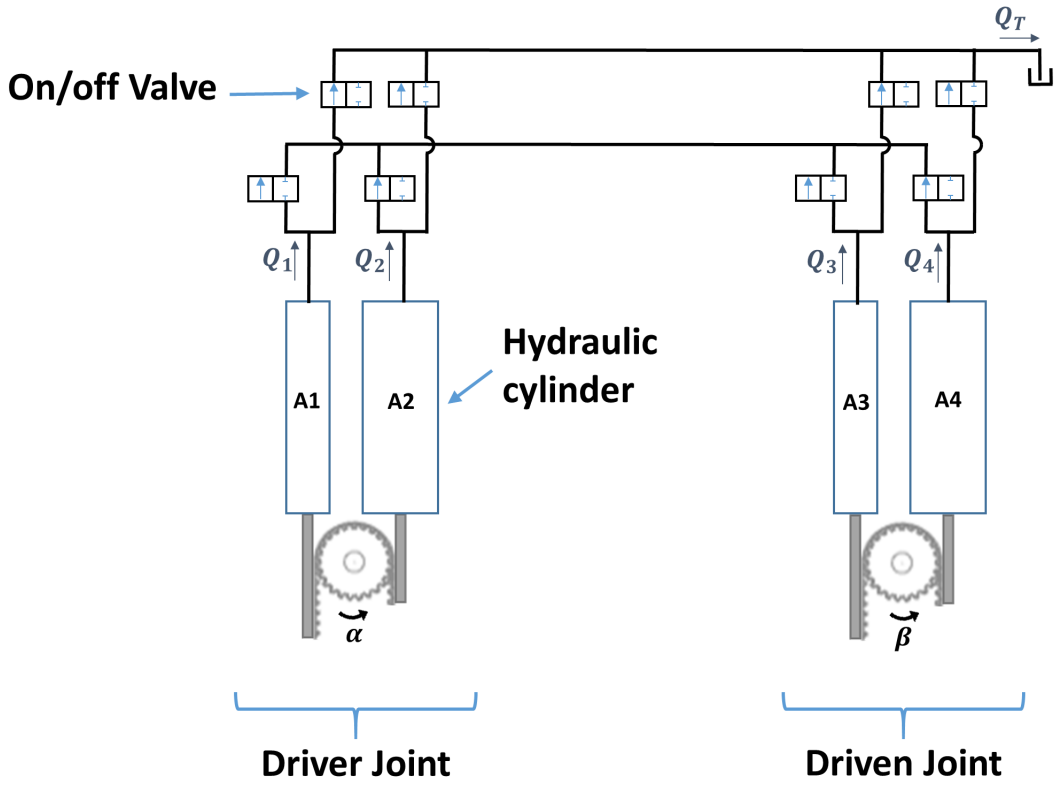

Figure 4.6: Variable hydraulic transmission circuit with four cylinders.

Transmission ratio analyses on a variable hydraulic transmission is performed in previous studies [58]. Similar analyses can be conducted on the variable transmission. The joint angles of the system can be represented by matrix $\theta = [\alpha_1 \ \alpha_2 \ \cdots \ \alpha_n]$. The system had two joints with angles of $\theta = [\alpha \ \beta]^T$. The displacement in each of the cylinders is a function of joint angle for the corresponding pulley size. The displacement of each piston can be represented by the displacement matrix $x = f(\theta) = r\theta$, where r is the pulley radius. The piston velocity is the time derivative of displacement $\dot{x} = \frac{\partial f}{\partial \theta}\theta$. With the hydraulic system's incompressibility assumption, each cylinder's flowrate is $Q_i = \dot{x}A_i$ where A matrix is the diagonal matrix of all n cylinders' cross-sections. The flowrate matrix is a function of the joint velocity matrix, and it can be represented by

a Jacobian $J \in R^{n \times m}$ where n is the number of pistons, and m is the number of joints.

$$Q = J\dot{\theta} \tag{4.1}$$

$$J = A\frac{\partial f}{\partial \theta} \tag{4.2}$$

The net flow into and out of the system is $Q_{total} = \sum_{i=1}^{n} Q_i$. It can be represented in the following vector notation:

$$Q_{total} = 1^T J\dot{\theta} \tag{4.3}$$

where 1 is an n-dimensional column vector of ones.

Two on/off valves connect each cylinder to either the closed manifold or the reservoir. The set of valves can be represented by a vector s. For each cylinder i, $s_i = 1$ if the cylinder is connected to the manifold and $s_i = 0$ if the cylinder is connected to the reservoir. The total flow rate going into the manifold must be zero

$$s^T Q_{total} = s^T J\dot{\theta} = c^T\dot{\theta} = 0 \tag{4.4}$$

c is a m-dimensional constraint vector $c = J^T s$. The flow rate going into the tank will be equal to the total flow rate since the common manifold's flow rate is zero.

$$Q_T = Q_{total} = 1^T J\dot{\theta} \tag{4.5}$$

The flow going into the tank needs to have the same pressure as the common manifold pressure to ensure the joints stay neutral when there is no additional torque on them. That requires the tank to be an accumulator (Figure 2.10) to be pre-pressurized with the system.

Alternatively, the system can be more compact by removing the accumulator. The net flow rate to the tank (Q_T) needs to be zero in this case ($1^T J = 0$). This adds a geometrical constraint in designing the transmission ($1^T J = 0$). In this case, instead of a common manifold and a reservoir, there will be a manifold A and manifold B.

The manifold B are all the lines that the valve state (s) is zero for them. The flowrate in manifold B has to be zero, and it adds a constraint in choosing the cylinders' bore and pulley sizes.

The manifold A are all the lines that the valve state (s) is one for them. The flowrate in manifold A has to be zero, and it determines the transmission ratio between the joint. The flowrate $c^T\dot{\theta}$ is zero, and for a system with two shafts, we can write

$$[c_1 c_2] \begin{bmatrix} \dot{\alpha} \\ \dot{\beta} \end{bmatrix} = 0 \tag{4.6}$$

The transmission ratio T is equal to

$$T = \frac{\dot{\beta}}{\dot{\alpha}} = -\frac{c_1}{c_2} \tag{4.7}$$

Using four cylinders and eight valves (Figure 4.6), 16 (2^4) transmission ratios are available. Still, 11 are redundant, two of them are not useful (+inf and -inf), leaving only 3 unique variable transmission ratios including zero, 1:1, and 1:-1.

Table 4.1: The dimension of a variable hydraulic transmission with eight cylinders.

	1	2	3	4
Cylinder bore (mm)	20.3	27.3	20.3	27.3
Pulley diameter (mm)	45.7	30.5	45.7	30.5

For valve state $s = [1010]^T$, since $c = J^T s$ and $J^T = \begin{bmatrix} 0.9 & -0.9 & 0 & 0 \\ 0 & 0 & 0.9 & -0.9 \end{bmatrix}$, the corresponding transmission ratio is $T = \frac{\dot{\beta}}{\dot{\alpha}} = -1$ since $c_1 = 0.9$ and $c_2 = 0.9$.

Figure 4.7 shows the variable hydraulic transmission device with eight LSRD cylinders, four pulleys, and sixteen valves. Pulleys connected to the joint shafts allow all cylinders to affect the transmission ratio. Each cylinder can be connected to the common manifold A or B using the on/off valves.

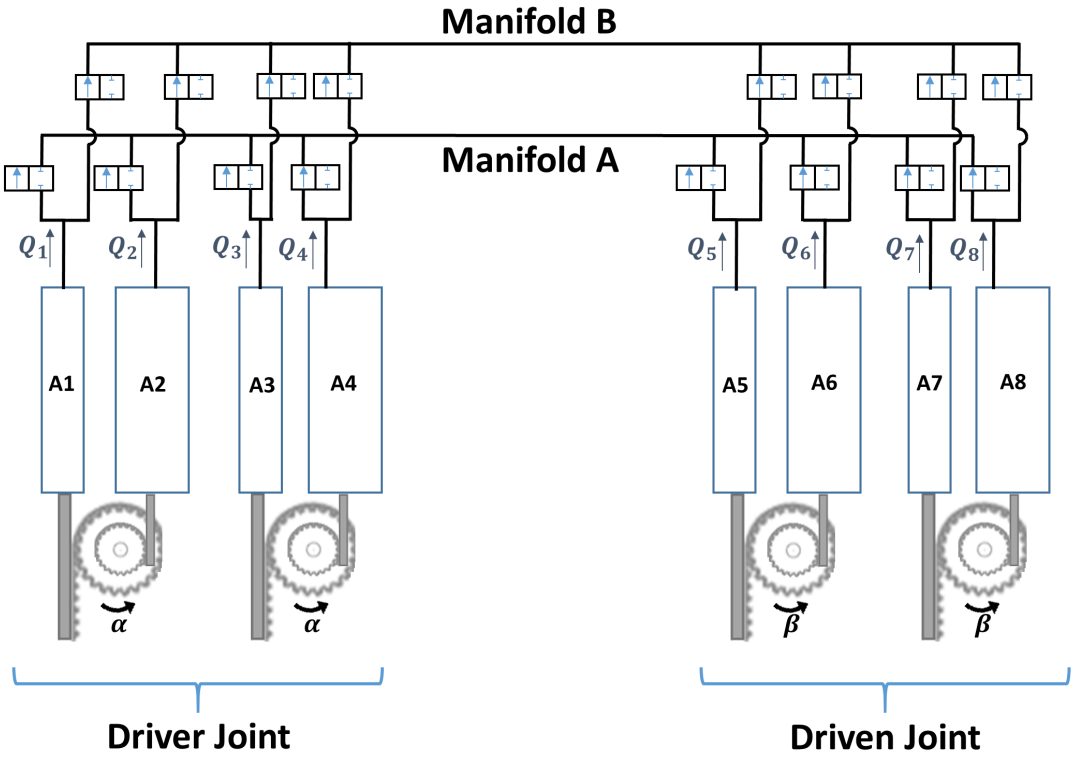

Figure 4.7: Variable hydraulic transmission circuit with eight cylinders.

Choosing one size for the large cylinders and one for the small ones and setting the pulley sizes for cylinders 1 to 3 and 5 to 7, the constraint ($1^T J = 0$) can be used to find the pulley size for cylinder 4 and 8. Table 4.2 shows the dimension of this transmission setup and Figure 4.8 demonstrates the 67 unique transmission ratios range from -6.5 to +6.5.

Table 4.2: The dimension of a variable hydraulic transmission with eight cylinders.

	1	2	3	4	5	6	7	8
Cylinder bore (mm)	20.3	27.3	20.3	27.3	20.3	27.3	20.3	27.3
Pulley diameter (mm)	45.7	30.5	30.5	10.2	45.7	30.5	45.7	17.8

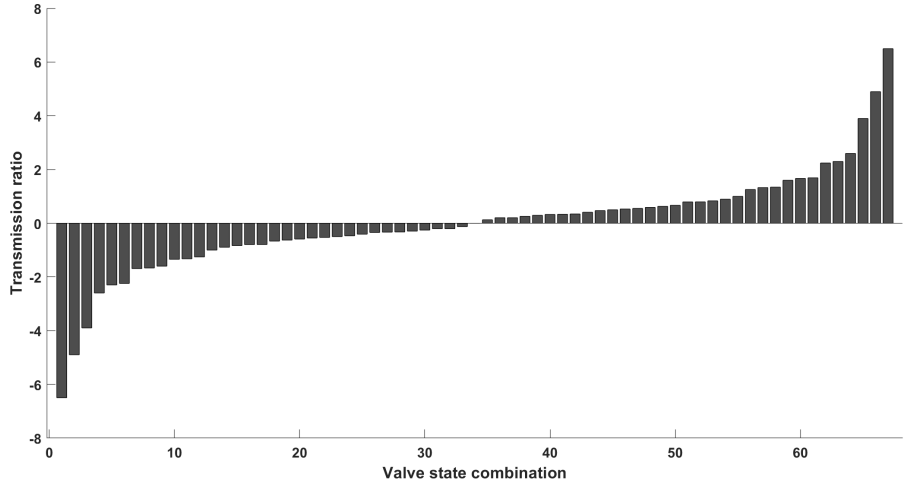

Figure 4.8: The 67 unique transmission ratios for all possible valve states for a transmission setup with eight cylinders.

The proposed variable hydraulic transmission

The system in Figure 4.7 has eight cylinders and 16 valves. To simplify the system, two cylinders are removed from the output. Due to the number of redundant transmission ratios, removing two cylinders from the output allows having no valves at the output. Figure 4.9 shows the resulting system with six cylinders and no output valves. Due to the antagonist action in the cylinders at the output, cylinder number 5 is permanently connected to manifold A, cylinder 6 is connected to manifold B, and the transmission switches occur at the input.

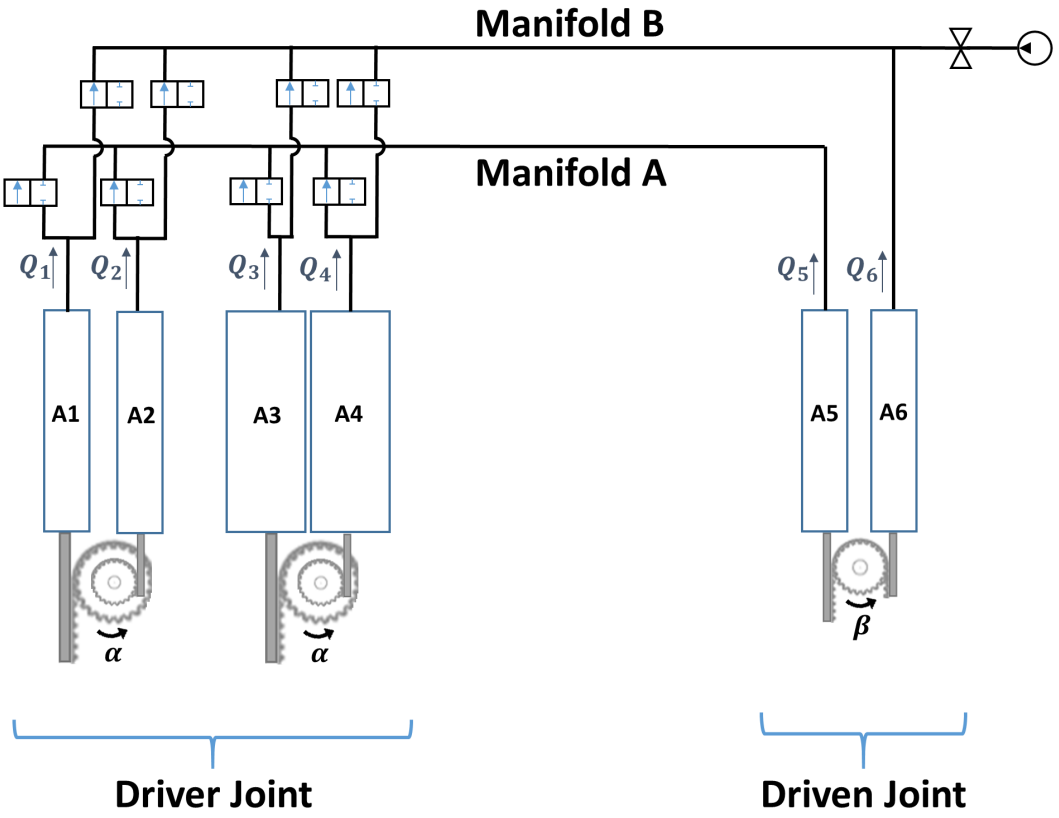

Figure 4.9: The proposed variable hydraulic transmission circuit with six cylinders.

This configuration makes the system asymmetrical, with four cylinders at the input and two cylinders at the output. This will cause different performance from input to output and reversely. On the other hand, this will allow the removal of eight valves from the system. The output joint will be more compact with a lower pressure drop due to the lower number of valves in the system.

Two bore sizes were chosen for cylinders. Pulley sizes were set by the fact that $1^T J$ must be zero. The pulley sizes for cylinders 1,2,3, and 5 were chosen, and the pulley sizes for cylinders 4 and 6 were found using the constraint.

Table 4.3 shows the dimension of the cylinders and pulleys in the system. The bore size is the diameter corresponding to the effective area discussed in Chapter 2.

Figure 4.10 shows the device with the input on the left and output on the right.

Table 4.3: The dimension of the proposed variable hydraulic transmission.

	1	2	3	4	5	6
Cylinder bore (mm)	20.3	20.3	27.3	27.3	20.3	20.3
Pulley diameter (mm)	45.7	30.5	30.5	38.6	30.5	30.5

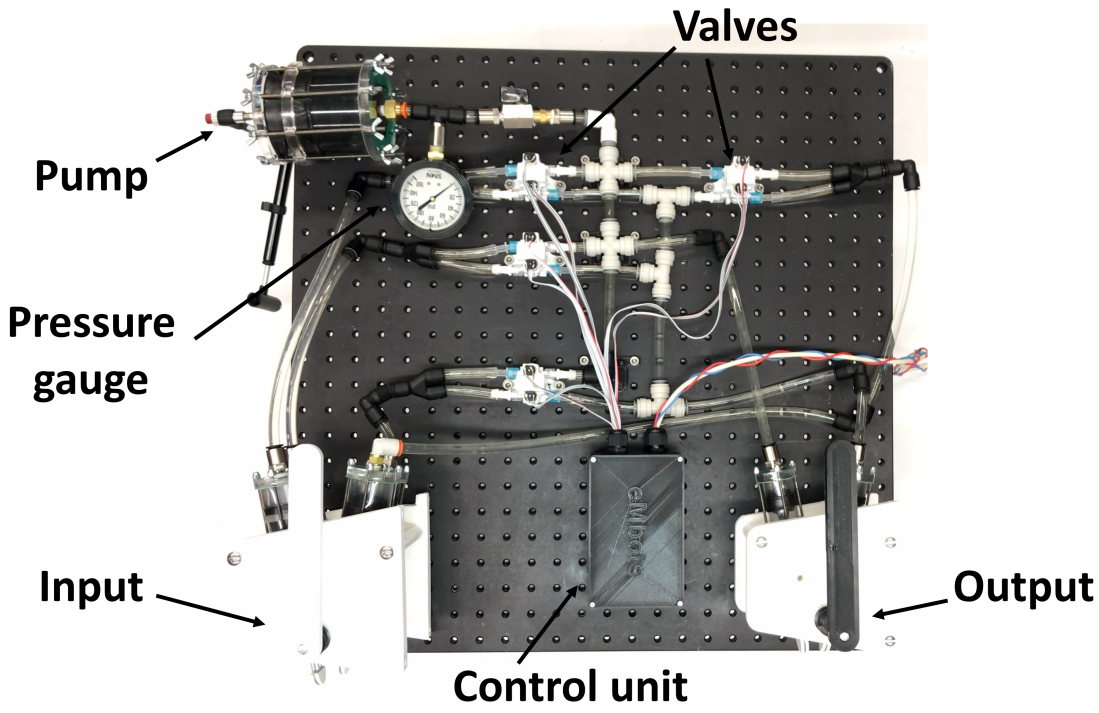

Figure 4.10: The bench-top setup of the proposed variable hydraulic transmission.

Pulleys were designed to have different diameters on each side to have unique pulley sizes for each of the cylinders in pair (Figure 4.12). A cable was inserted inside the pulley and fixed with epoxy. A pair of pulleys were used for each cylinder pair. The cable was tensioned by pre-pressurizing the system (Figure 4.11).

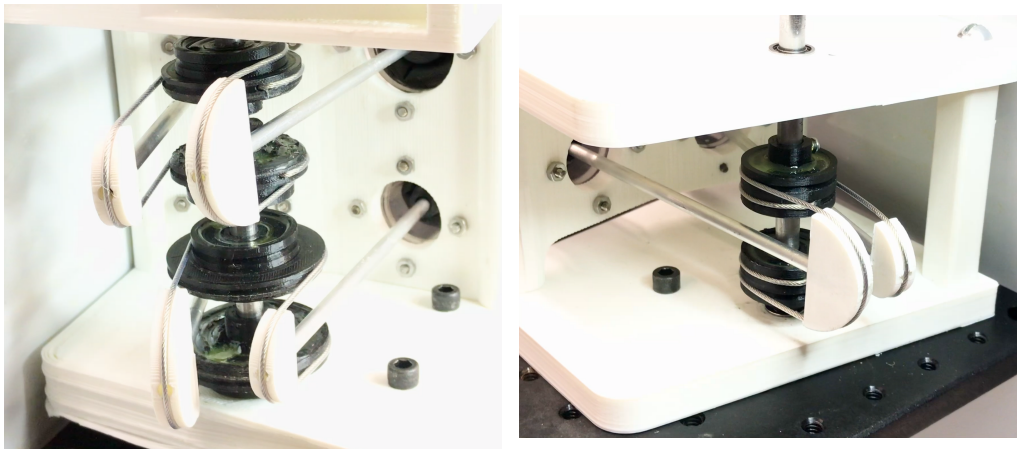

(a) Input (Driver joint).

(b) Output (Driven joint).

Figure 4.11: The cable/pulley mechanism to transmit translational movement to rotational.

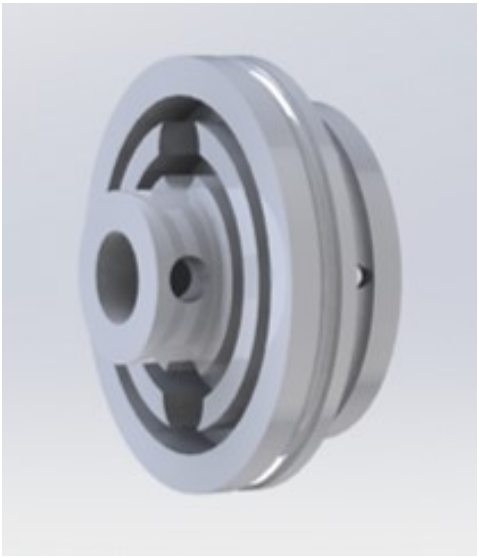

Figure 4.12: The double-sized pulley design to fix the the cable in.

Figure 4.13 and Table 4.4 show the 15 unique transmissions from input with four cylinders to the output with two cylinders. The valve state (s) required to have each transmission ratio is shown in Figure 4.4.

Table 4.4: The 15 transmission ratios and required valve state of the system shows in Figure 4.10 and Figure 4.9

Transmission ratio	s[1]	s[2]	s[3]	s[4]	s[5]	s[6]
-3.4	1	0	1	0	1	0
-2.4	1	1	1	0	1	0
-1.9	0	0	1	0	1	0
-1.5	1	0	0	0	1	0
-1	1	0	1	1	1	0
-0.9	0	1	1	0	1	0
-0.5	1	1	0	0	1	0
0	0	0	0	0	1	0
0.5	0	0	1	1	1	0
0.9	1	0	0	1	1	0
1	0	1	0	0	1	0
1.5	0	1	1	1	1	0
1.9	1	1	0	1	1	0
2.4	0	0	0	1	1	0
3.4	0	1	0	1	1	0

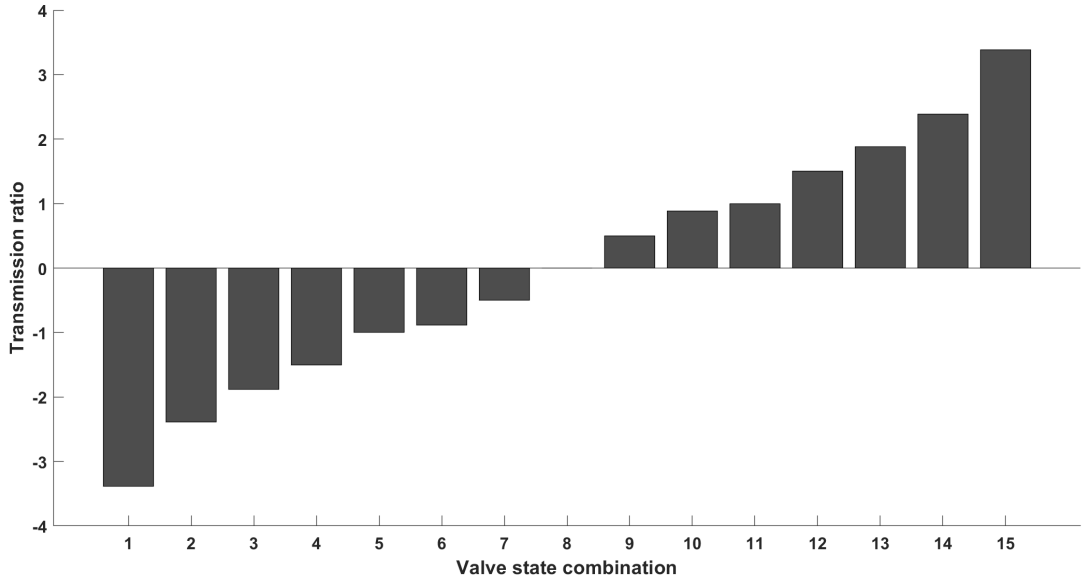

Figure 4.13: The 15 unique transmission ratios for all possible valve states.

The unique transmission ratio and valve state for each transmission for the system driven reversely are shown in Figure 4.14 and Table 4.5.

Table 4.5: The transmission guideline and required valve state of the system that is reversely driven.

Transmission ratio	s[1]	s[2]	s[3]	s[4]	s[5]	s[6]
-2	1	1	0	0	1	0
-1.13	0	1	1	0	1	0
-1	1	0	1	1	1	0
-0.67	1	0	0	0	1	0
-0.53	0	0	1	0	1	0
-0.42	1	1	1	0	1	0
-0.3	1	0	1	0	1	0
0	0	0	0	0	1	0
0.3	0	1	0	1	1	0
0.42	0	0	0	1	1	0
0.53	1	1	0	1	1	0
0.67	0	1	1	1	1	0
1	0	1	0	0	1	0
1.13	1	0	0	1	1	0
2	0	0	1	1	1	0

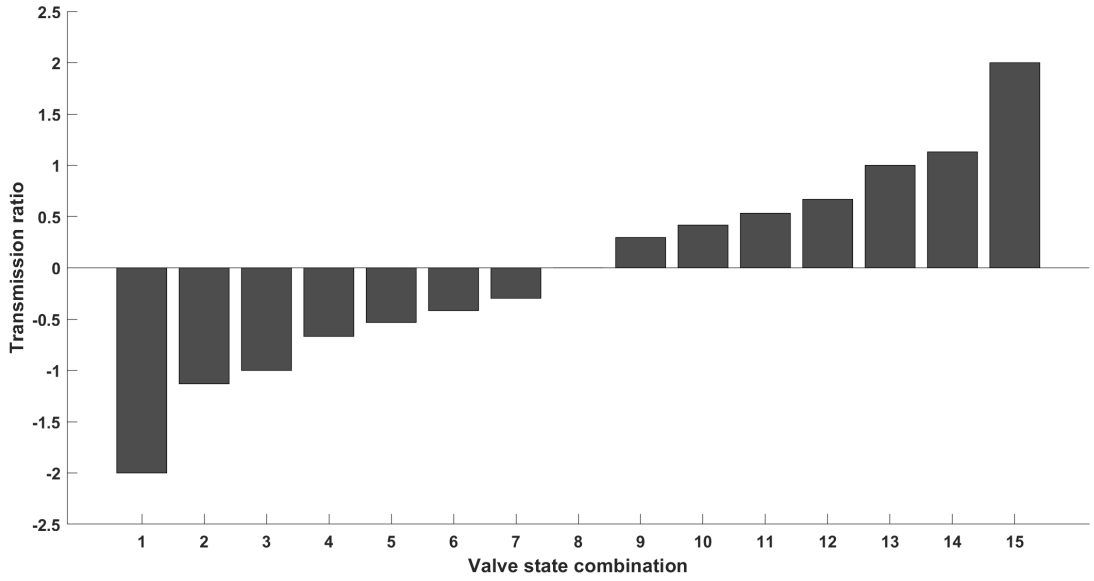

Figure 4.14: Unique transmission ratios for all possible valve states of the system that is reversely driven.

As demonstrated in Tables 4.4 and 4.5the valve state for the cylinders 5 and 6 are fixed for all the unique transmission ratios. Therefore, the valves for the output cylinders can be removed, as discussed before.

4.2.2 Performance evaluation

The system was pre-pressurized to 30 psi (210 kPa) for all the performance evaluation tests, and the isolation valve was closed.

Position transmission

A stepper motor (Pololu, # 2267) was used with a motor controller (Pololu, # 3130) to give random positions to the input joint while the output joint was unloaded (Figure 4.15). The motor was connected to the input shaft using a timing belt and pulley. The input and output positions were measured using a 1000 PPR incremental optical rotary encoders (Calt, # GHS38-6G2500BMP526) connected to the shafts using timing belts and pulleys. There were 20 trials for each of the transmission ratios. The test was

performed having the joint with four cylinders as the input for transmission ratios of 1:1, 1:0.5, 1:2.4, 1:-0.9, 1:-1, and 1:-3.4 and transmission ratios of 1:1, 1:0.4, 1:-0.3, and 1:-1 when the system was driven reversely from output to input.

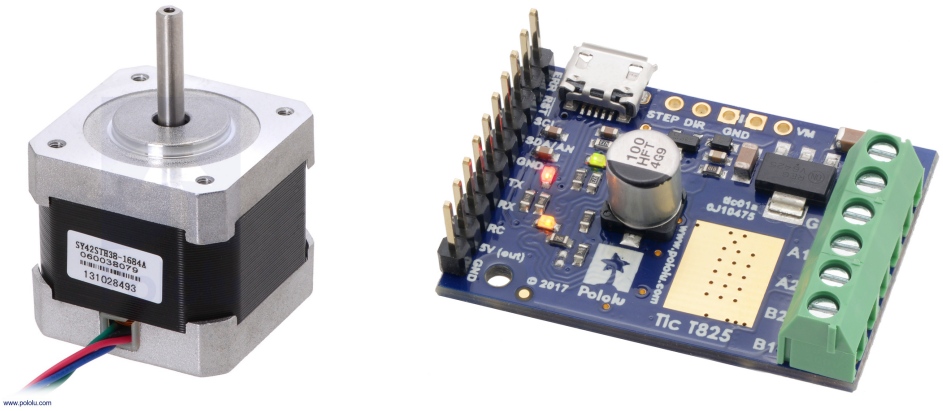

(a) Stepper motor. (b) Motor controller

Figure 4.15: Stepper motor and controller used to test the transmission. (Images from www.pololu.com)

Position tracking

The stepper motor drove the input joint with four cylinders with a sinusoidal displacement while the output was unloaded. The valves were set to switch between six transmission ratios from 1:1 to 1:-1.5, 1:0, 1:0.5, 1:-1, and 1:2.4. The input and output joint displacements were measured using the rotary encoders.

Frequency response

The input joint was moved at frequencies from 0.1 to 4 Hz while the output joint was unloaded. The rotary encoders were used to measure the displacement of the input and output joints. The amplitude and phase diagrams were derived from the periodic input and output displacements. Four Hz was the maximum frequency tested as 4 Hz would be the maximum useful frequency in rehabilitation and most puppetry applications.

Output acceleration bump

The stepper motor was placed on the input joint to move it with a constant velocity (zero acceleration) while the output joint was unloaded. There was a displacement with zero acceleration at the output. An accelerometer (SparkFun ADXL337) was placed on the output handle, 2.5 inches from the joint. A bump in acceleration was seen when the transmission ratio was switched. The acceleration bump would disturb the performance of the output joint while the input joint is being moved.

The transmission ratio switch effect on the acceleration bump was evaluated by repeating the test from transmission ratio of 1:0.9 to 1:1.9, 1:3.4, 1:1, and 1:-0.9. Each of these requires 1, 2, 3, and 4 pairs of valves to be switched, respectively. Another test was conducted to evaluate the acceleration bump in the output if all the required valves switch simultaneously or in a sequence. Sequence delays of 0 ms, 35 ms, 40 ms, 55 ms, and 75 ms were considered to show the importance of the valve actuation sequence. The settling time was derived from the displacement plots as the time span since the acceleration settled in the steady-state error bar.

Input acceleration bump

The input handle was moved at an approximately constant velocity (zero acceleration) with the output joint unloaded. The accelerometer was placed on the input handle, 2.5 inches from the joint. The handle was gripped softly with two fingers (Figure 4.16a) and hard with the palm (Figure 4.16b) to address the operator's damping action. The acceleration bump was evaluated for the case where the valves were actuated simultaneously or in a sequence. The transmission ratio was switched from 1:0.9 to 1:1 and 1:-09 simultaneously and with a 40 ms delay. The augmented Lagrangian method discussed in [85] was used to denoise the acceleration. Figure 4.17 compares an example of the measured and filtered acceleration data.

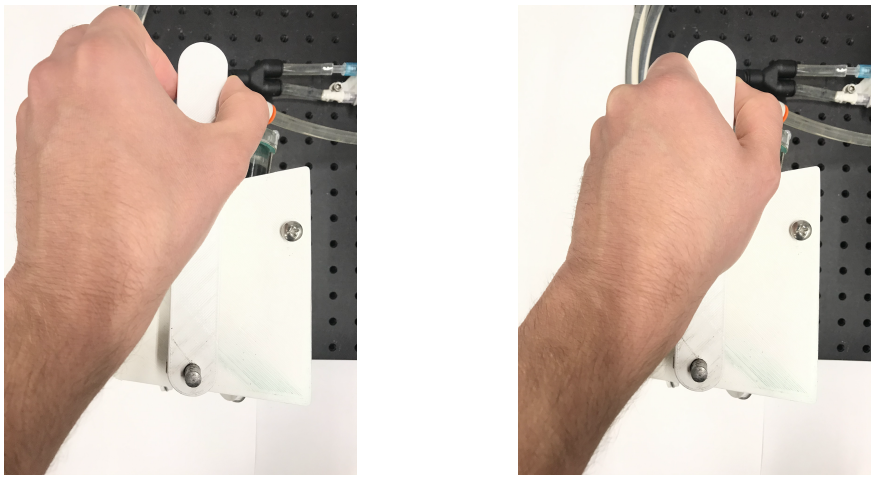

(a) Soft grip. (b) Hard grip.

Figure 4.16: The input manipulation during the input acceleration bump test.

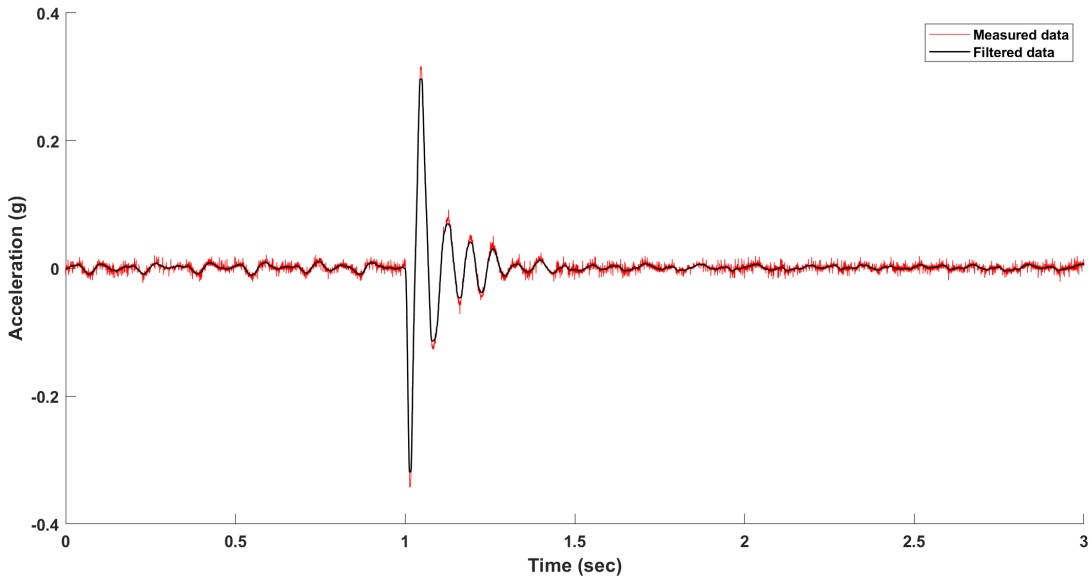

Figure 4.17: The measured acceleration vs the filtered acceleration for transmission switched from 1:0.9 to 1:1 with no delay.

Haptics

Low friction, high efficiency, and incompressibility of the fluid are necessary for haptic feedback. To test the system's haptic capabilities, a balloon was set to be on the output workspace with a sharp object placed on the output handle (Figure 4.31a). The user was blindfolded, had white noise on headphones, and was not aware of the balloon or the handle position. A transmission ratio of 1:1.5 and 1:3.4 was set on the device, and multiple cases were tested during this scenario.

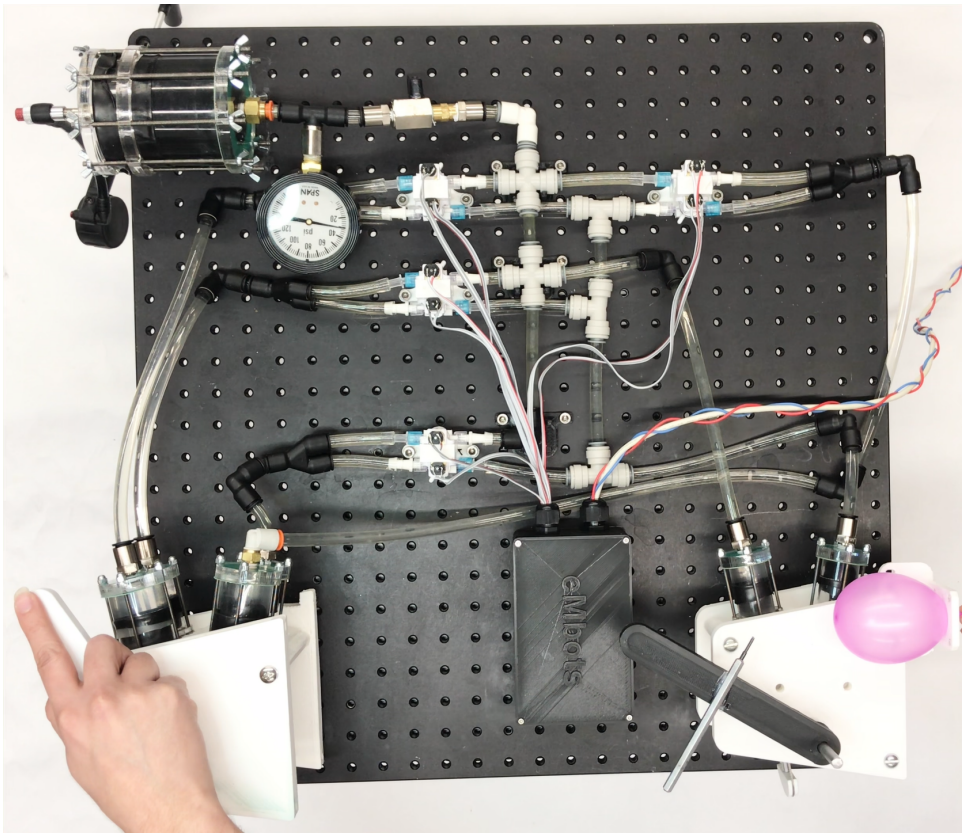

Figure 4.18: The setup for evaluating haptic performance.

4.3 Results

4.3.1 Position transmission

Figure 4.19 shows the 120 trials at six transmission ratios. The gray dashed lines indicate the expected transmission ratio. The error between the expected and measured transmission ratio varies from zero to three percent.

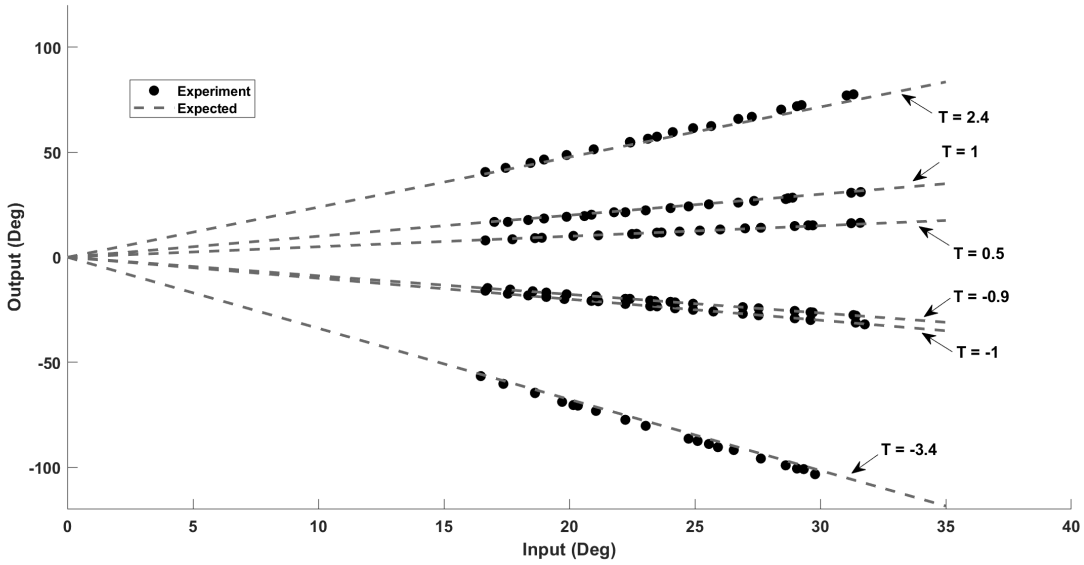

Figure 4.19: Position transmission of the system. Gray lines specify the expected transmission ratio and black dots are experimental trials.

By switching the input and output, the stepper motor carried the output and the system was driven reversely while the input was unloaded. Figure 4.20 shows the 60 trials at four different transmission ratios. The expected transmission ratio is depicted by the gray dashed line. The error by using the device reversely is from six to 12 percent.

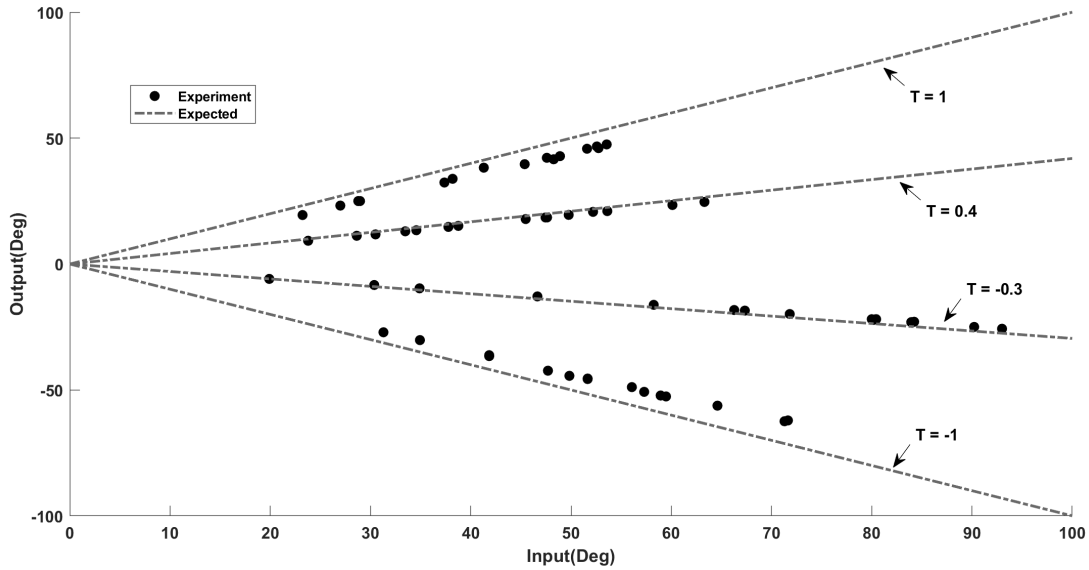

Figure 4.20: Position transmission of the system that is reversely driven. Gray lines specify the expected transmission ratio and black dots are experimental trials.

4.3.2 Position tracking

The input joint with four cylinders moved consistently with the stepper motor going through a sinusoidal. The input and output positions over the six transmission ratios are shown in Figure 4.21.

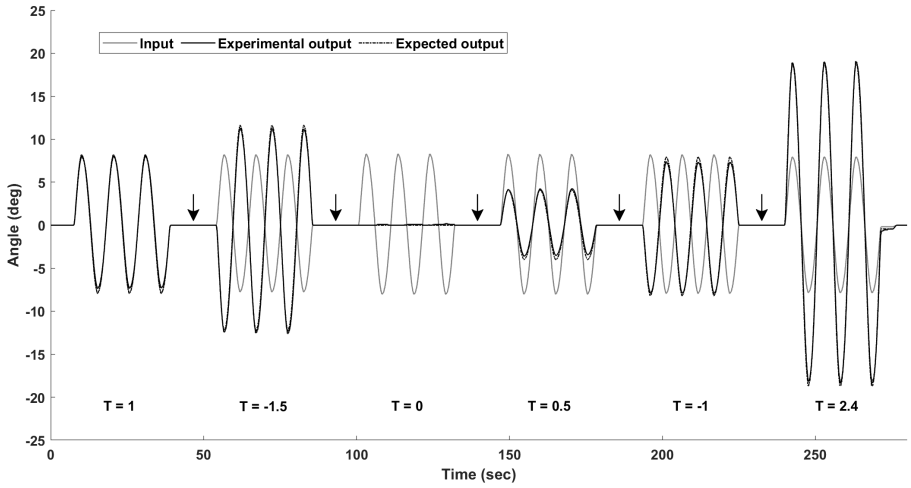

Figure 4.21: The position tracking of the system where the switches in transmission ratio are shown with a black arrow. The dashed line depicts the expected output.

4.3.3 Frequency response

The position output to input ratio and phase delay of the unloaded system at transmission ratio of 1:1 and 1:-1.5 are illustrated in Figure 4.22. The input were moving at frequencies from 0.1 to 4 Hz. The input and output positions were measured using the rotary encoders.

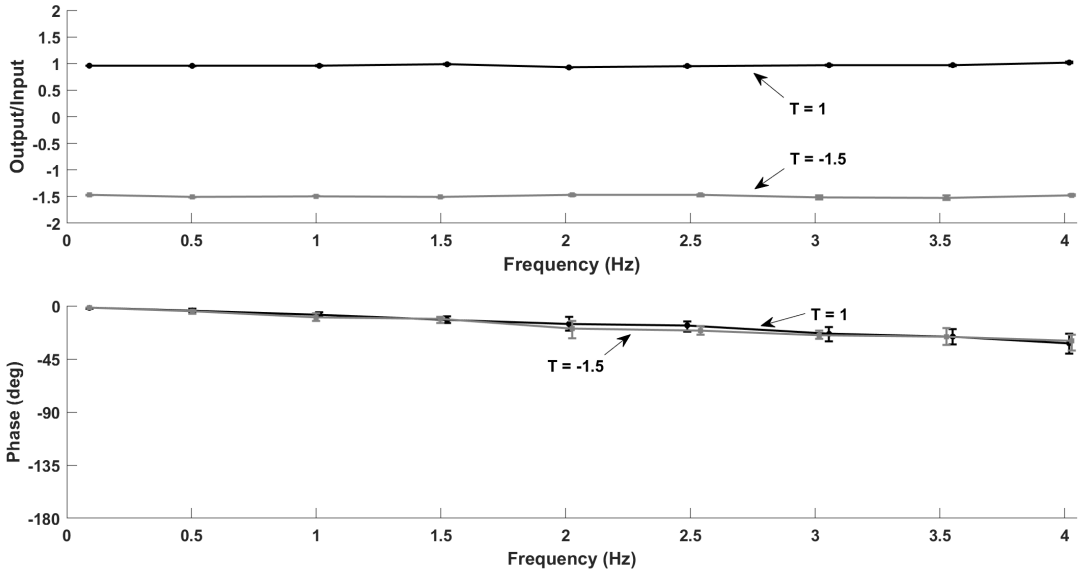

Figure 4.22: The amplitude and phase frequency response of the system with transmission ratio of 1:-1 and 1:-1.5.

4.3.4 Output acceleration bump

The acceleration at the output handle was measured while the input was moving at the constant velocity. The acceleration was zero at the input and output handles; however, a bump in acceleration happened at the input and output handles by switching the transmission ratio. Figure 4.23 illustrates the acceleration bump at the output while changing the transmission from 1:0.9 to 1:1.9, 1:3.4, 1:1, and 1:-0.9. The valves all were switched at the same time.

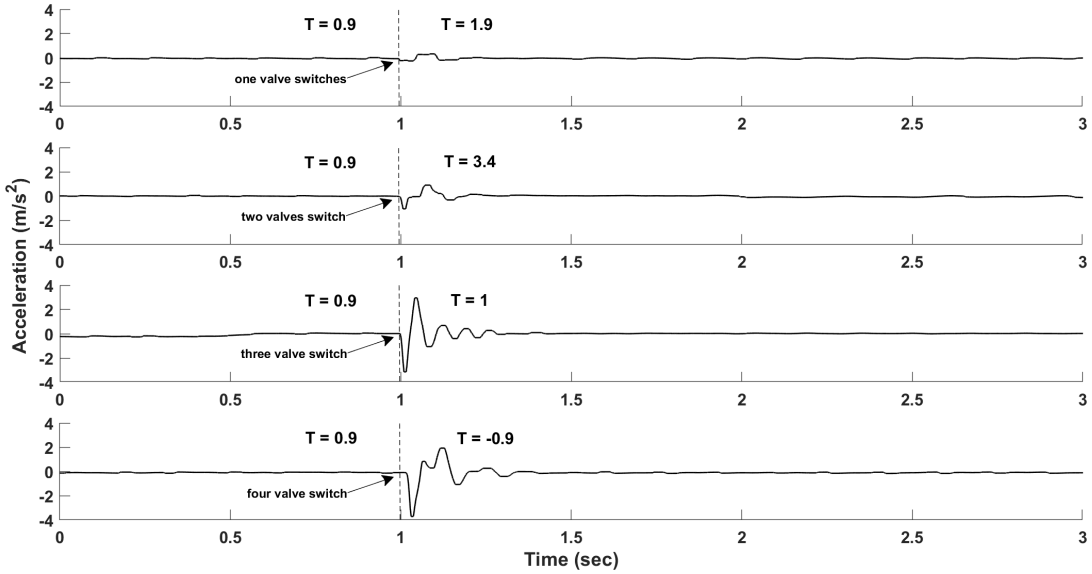

Figure 4.23: The acceleration bump in the output for four transmission switches. The switches in transmission ratio are indicated with the gray dashed line. The number of valves required to be switched is depicted

The maximum acceleration bump for these transmissions is shown in Figure 4.24.

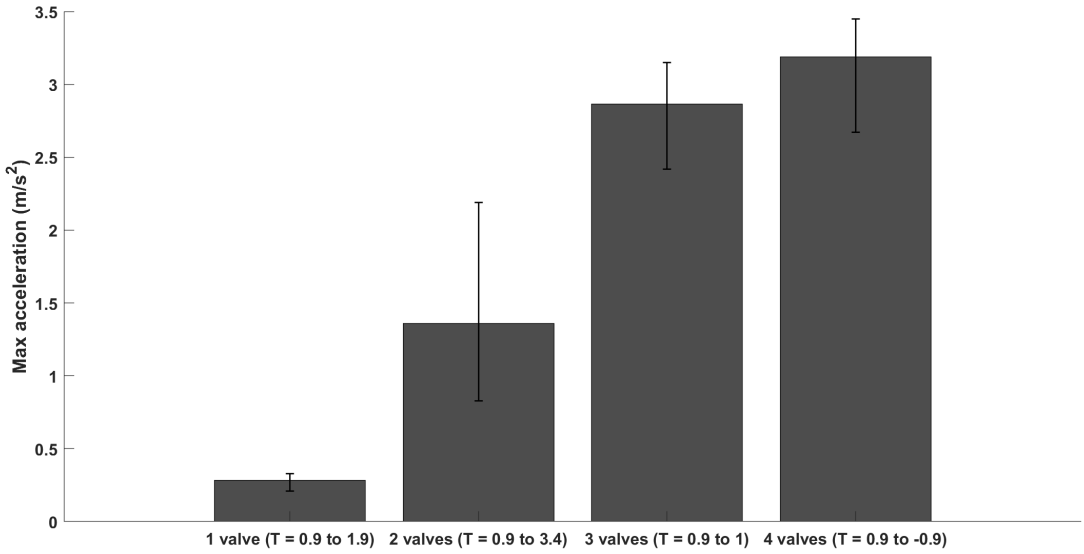

Figure 4.24: The maximum acceleration in the output for four transmission switches. The error bars show the maximum and minimum cases out of five trials.

Sequencing the valve switching times reduced the acceleration bumps. The delay in milliseconds was the time each pair of valves stood by prior to getting actuated after the previous pair of valves switched. Figure 4.25 indicates the acceleration bump for the transmission ratio switched from 1:0.9 to 1:1, which includes actuation in three pairs of valves. The sequence delay was 0, 35, and 40 ms.

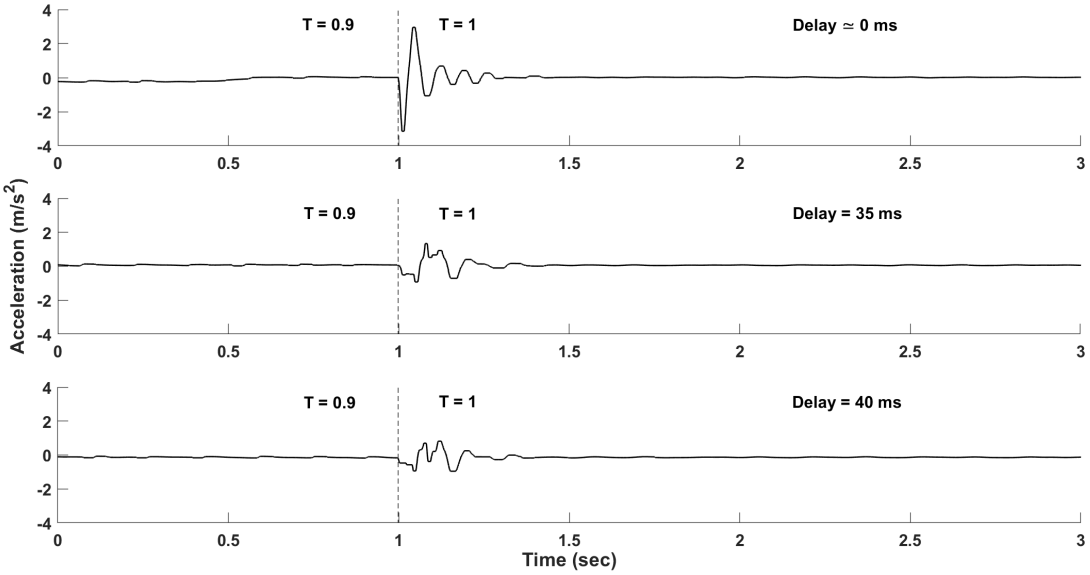

Figure 4.25: The acceleration bump in the output with simultaneous and staggered actuation of three pairs of valves.

As the input consistently moves with zero acceleration, the settling time is the time for the output acceleration bump to settle in the error bar of 0.2 m/s^2. Figure 4.26 shows the maximum acceleration bump and settling time for sequence delay from 0 to 75 ms.

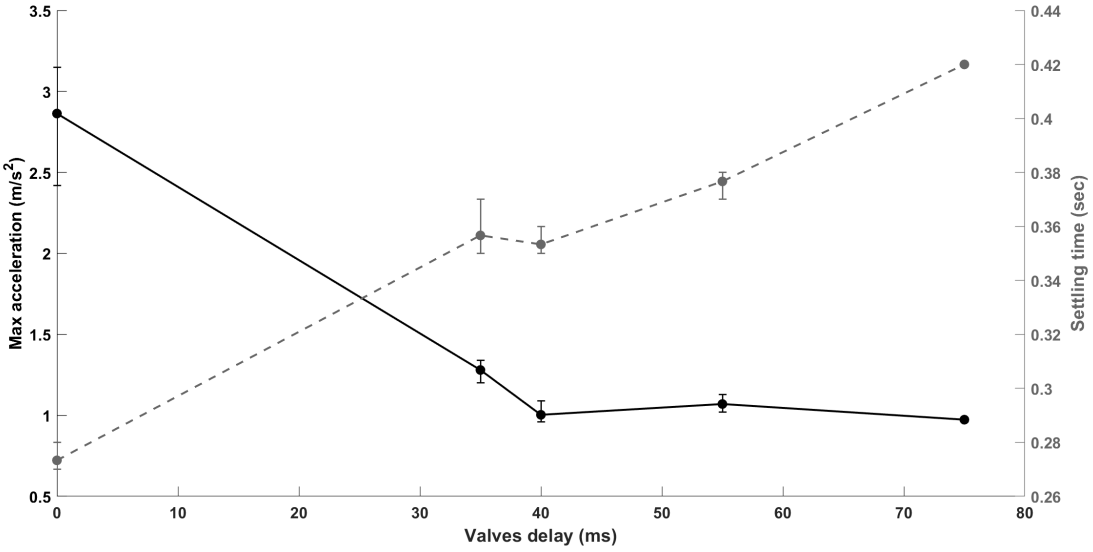

Figure 4.26: The maximum acceleration bump and settling time in the output for simulations and delayed actuation of the valves.

The settling time, error bar, and maximum acceleration bump for the output acceleration of a switch from 1:0.9 transmission ratio to 1:1 are illustrated in the Figure 4.27. The stepper motor was used to have a constant acceleration, and the vibration of the stepper motor causes some steady-state error in acceleration which was found to be around 0.2 m/s^2.

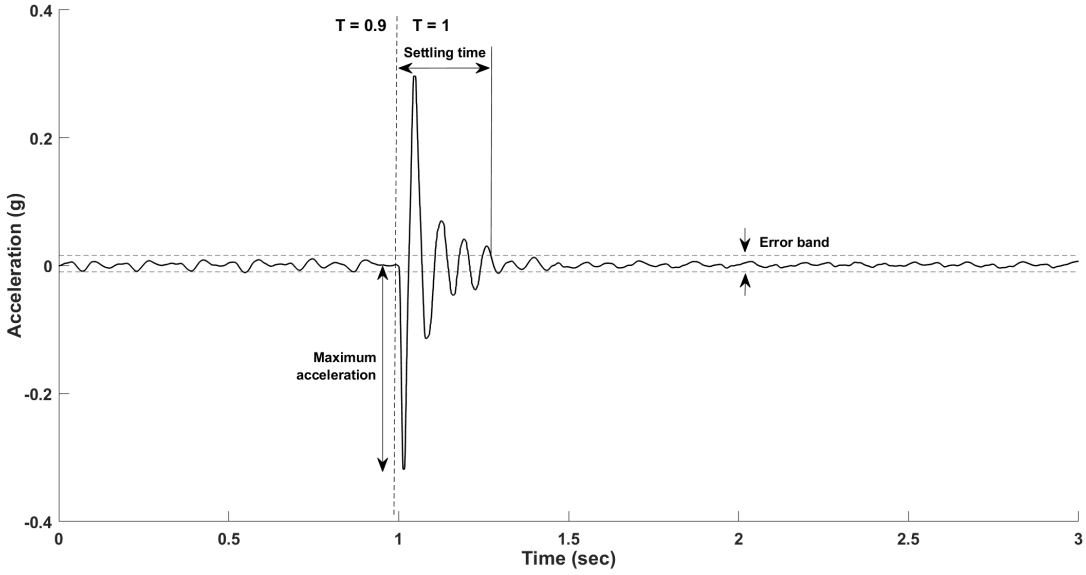

Figure 4.27: An example of recorded acceleration with the maximum acceleration bump, settling time, and error band shown.

4.3.5 Input acceleration bump

The acceleration bump at the input joint was measured while the output was unloaded, and the input was being moved by a soft grip and hard grip at an approximately constant velocity. Figure 4.28 shows the acceleration bump of the input joint for transmission switch from 1:0.9 to 1:1 with soft and hard grips at simultaneous valve actuation and a sequence valve actuation with the delay of 40 ms.

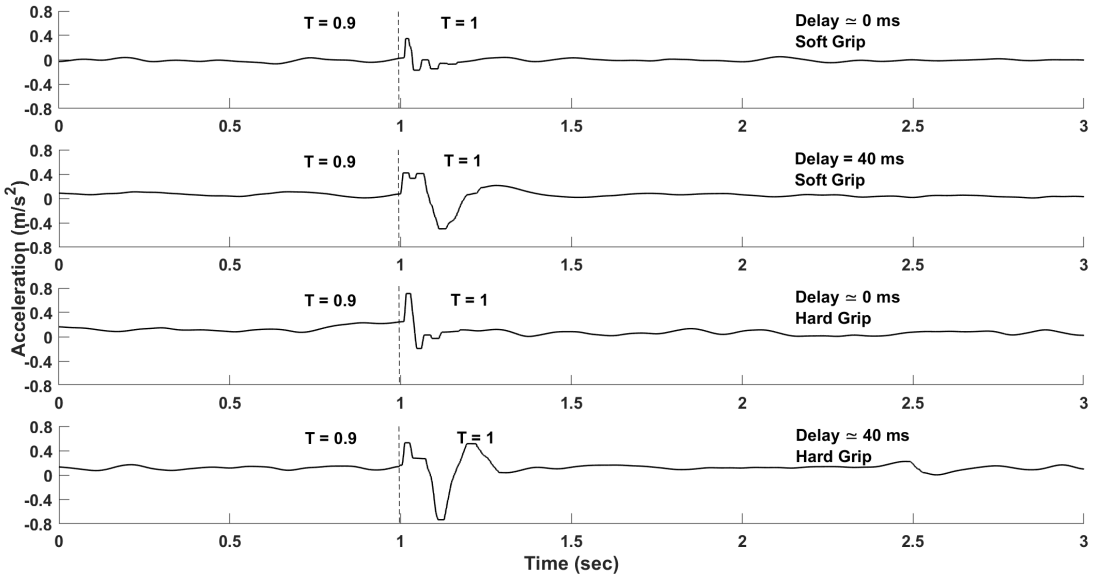

Figure 4.28: The acceleration bump in the input with simultaneous and delayed actuation of the valves for soft and hard grip of the input handle. Switching the transmission ratio from 1:0.9 to 1:1.

The soft and hard grip acceleration bump at the input joint for transmission switch from 1:0.9 to 1:-0.9, which requires four pairs of valves to switch, is shown (Figure 4.29).

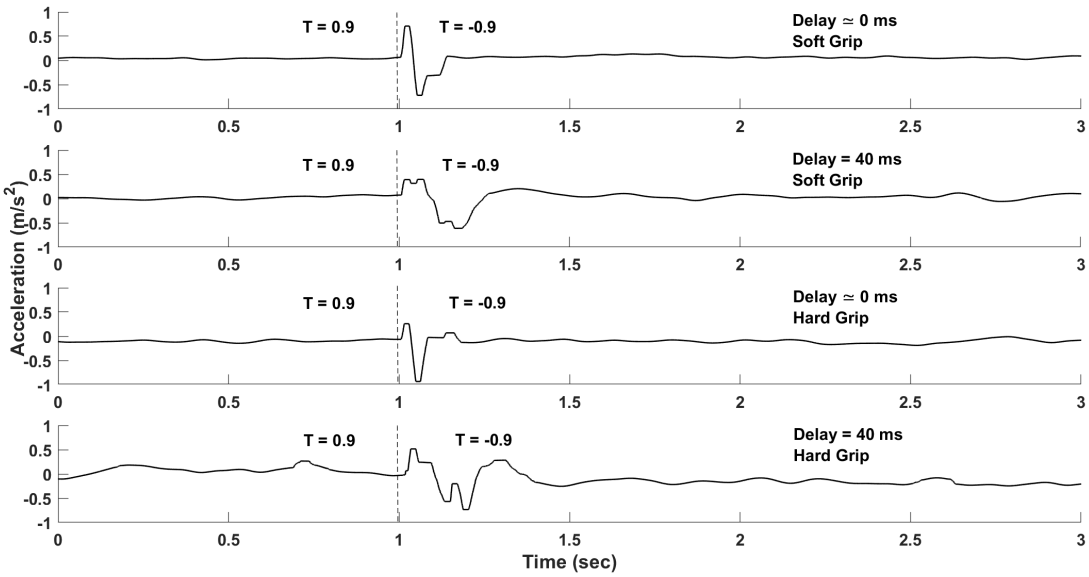

Figure 4.29: The acceleration bump in the input with simultaneous and delayed actuation of the valves for soft and hard grip of the input handle. Switching the transmission ratio from 1:0.9 to 1:-0.9.

The maximum acceleration in the input joint for a soft and hard grip is depicted (Figure 4.30).

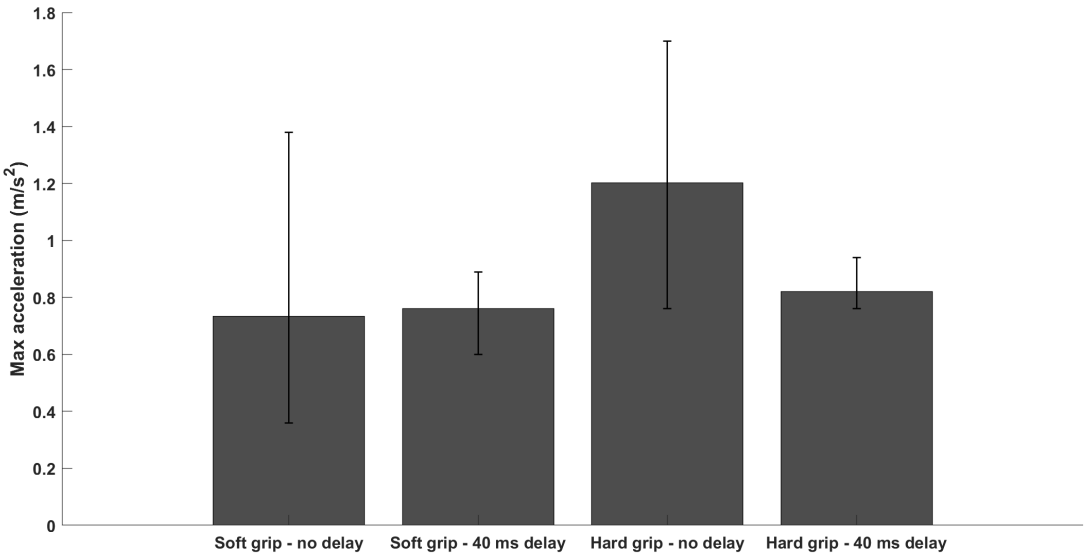

Figure 4.30: The maximum acceleration bump and settling time in the input for simulations and delayed actuation of the valves for soft and hard grip of the input handle.

4.3.6 Haptics

The qualitative test was conducted on the haptic feature of the transmission device. The user on the left was blindfolded, had headphones on with white noise playing, and was not aware of the position of the handle and whether the balloon exists or not. The mission was to avoid breaking the balloon. Figure 4.31 shows two attempts with and without the balloon. The transmission ratio was 1:3.4, and the same quality was achieved by conducting the same test with a transmission ratio of 1:1.5.

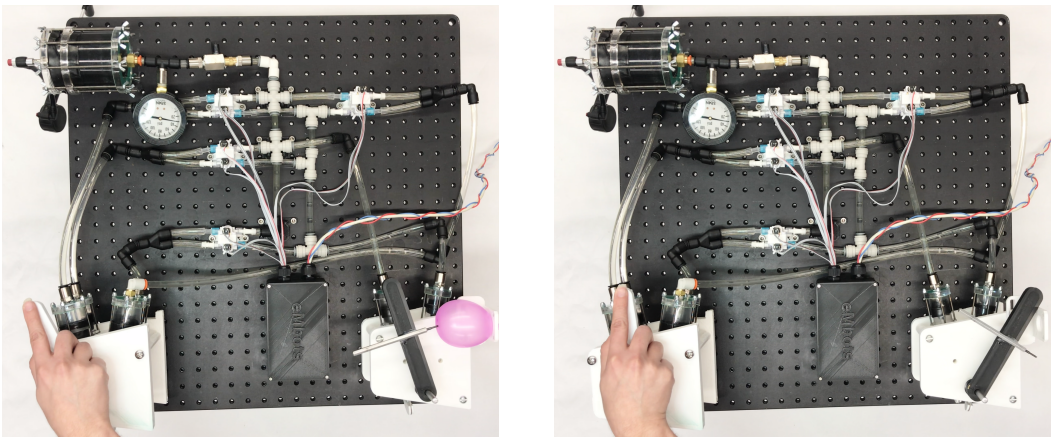

(a) User can feel the balloon before popping it. (b) User can tell if the balloon is in or out.

Figure 4.31: The screenshot of the qualitative haptic video.

4.4 Discussion

Backdrivability is crucial for the system as it allows a smooth motion from input to output, and reversely. Figure 4.10 shows the system with the input with four cylinders, and the output with two cylinders. Due to the system's asymmetry, performance from output to input differs from input to output's performance. Having only two cylinders at the output allows the valves at the output to be removed. Furthermore, a smaller number of cylinders means less friction in the system.

Higher number of cylinders are required to have more unique transmission ratios. If the reservoir pressure is the same as the system using the accumulator; then, the constraint can be neglected and higher number of transmission ratios are achievable at the expense of an accumulator in the system.

Figure 4.19 shows the position transmission from input to output. The error is less than 3 percent from the expected output. The manufacturing error, the elasticity of the hose, and diaphragms cause this volume inaccuracy. The manufacturing error includes the area of the cylinders discussed in Chapter 2 added to the error in sizing of the pulleys and misalignment of the cylinder rods.

Figure 4.20 shows the position transmission from output to input. In this case, added to the volume inaccuracy is the higher friction at the driven joint (with four

cylinders) which results in an error from the expected position of up to 12 percent.

The position tracking illustrated in Figure 4.21 proves the functionality of the transmission device. The transmission ratio of 1:0 shows the noise that is there due to the volume inefficiency.

The frequency response shown in Figure 4.22 illustrates stable performance over the range of frequencies. Low phase difference and constant amplitude assure the performance for MRI applications (lower than 0.5 Hz), rehabilitation (lower than 1 Hz), and puppeteering (lower than 4 Hz).

Both input and output handle bump when the transmission switches. Figure 4.23 shows that the output acceleration bump is not dependent on the difference in transmission ratio before and after the switch. However, the output acceleration bump, which affects the output's precision, depends on how much disturbance in flow occurs by switching the transmission ratio. The higher number of valves involved in the transmission ratio causes more acceleration bump at the output (Figure 4.24). This bump is primarily rooted in the flow stoppage in the valves that are open and need to be closed for the new transmission ratio.

Figure 4.25 illustrates that a delayed sequence in valve actuation decreases the acceleration bump at the output. In this case, the flow stoppage would happen in a sequence that will lessen the effect of the impulse at the output. However, the settling time of the output joint is the time for the output to settle to below of 0.2 m/s^2. A delay higher than 40 ms does not affect the acceleration bump; however, it increases the settling time (Figure 4.26).

The effect of the sequence delay in valve actuation on input acceleration bump depends on how the handle is gripped by the user (Figure 4.30). The soft grip at the input provides higher damping and consequently, lower peak acceleration. The hard grip, however, increases the peak acceleration.

The force at the input increases for any constant force at the output by increasing the transmission ratio. Hence, the system provides higher haptic feedback at higher transmission ratios. The haptic feedback is high enough to detect a balloon at the output with a sharp object for transmission ratios 1:1.5 and higher. The friction, compliance, and damping of the system should be eliminated to have better haptic feedback.

4.5 Conclusion

Having a constraint on the design to have zero net flow rate in each manifold allows one to remove the system's accumulator. In the realization presented in this chapter, the transmission had four cylinders at the input, two cylinders at the output, and eight valves to control the transmission ratio. The position transmission of this variable hydraulic transmission enabled close tracking between input and output. Less than 3 percent of error was found for position transmission from input to output for all the transmission configurations.

The output and input will experience a bump in acceleration at the moment of changing the transmission. This acceleration bump depends on stoppage in the fluid lines due to the switching. The number of required valves to switch can be related to address the bump at the output. Sequencing the actuation of the required valves decreases the acceleration bump at the expense of higher settling time. $40ms$ of delay was found to be a viable delay time for the valve actuation.

The system's inefficiencies come from friction in the cylinders and mechanical joints, pressure drop in the valves, and compressibility of the fluid. The haptic feedback from the output to input is adequate. A soft object like a balloon can be felt at the input by a sharp object at the output before popping.

Chapter 5

Force Transmission Modeling in a Variable Hydraulic Transmission

5.1 Introduction

Hydraulic systems in various applications have been modeled to achieve performance evaluation and improvement. The hydraulic transmission used for a wind turbine power conversion was modeled dynamically [86]. Mathematical modeling of components from pipelines to pumps was conducted to evaluate the performance of a hydraulic transmission in an offshore wind turbine [87]. A deductive mechanical and hydraulic mathematical modeling were performed in a continuous hydraulic transmission [88, 89].

The proposed variable hydraulic transmission in this thesis is illustrated in Figures 4.9 and 4.10. Force transmission evaluation is necessary to find the losses in the system, and modeling the system allows for specific improvements in components. The volume and force efficiencies affect the position and torque performance of the system. The position transmission related to uncertainty in the piston area was discussed in Chapter 4 and resulted in an accuracy of 98 percent.

The main losses in the system can be separated into mechanical and hydraulic pressure drop losses. The mechanical loss includes the friction at the mechanical joints and translational to the rotational mechanism and the long-stroke rolling diaphragm cylinders. In Chapter 2, the friction in the long-stroke rolling diaphragm was found to be two to five percent of the load.

Multiple designs for the joint in transmission were suggested by others. The timing belt, chain, and cables can be used to transmit the translational movement to a rotary one. A timing belt and pulley pair were used in an antagonist transmission described in previous chapters and a teleoperated robot designed for puppeteering purposes [5]. The challenge was to have equal tension in the pair of timing belts. A continuous cable design resolves that concern and allows a compact design for the joints.

The shafts of the cylinders were attached perpendicularly to a joint handle at a different offset in a previous study [90], to provide different moment arms for each cylinder and increase the number of unique transmission ratios in a variable hydraulic transmission. The force and position of each cylinder were perpendicular to the joint handle as long as the handle was vertical. The shaft to handle misaligned with about two degrees of rotation at the joint. This affects the accuracy of the Jacobin calculated for the relationship between the joint speed and hydraulic flowrate. The inaccuracy in the design of the joints in a variable hydraulic transmission directly affects the force efficiency of the device.

Hydraulic components geometries affect the flow resistance and hydraulic loss. The hose diameter, valves orifice size, the number of fittings are some of these parameters. A thorough evaluation of these parameters and their significance in the system's overall efficiency allows designers to find the best parameters to address.

The flow resistance and dynamic performance of hydraulic components have been evaluated in previous studies. The dynamic friction in the hydraulic cylinders were evaluated in one study [91]. This study concluded that the dynamic friction depends on the backing material of the rolling diaphragm and the pressure in the chambers. The flow forces on a seat valve were investigated in a study [92]. The geometry of the valve were discussed in previous chapters. The flow resistance in valves is the significant loss in digital hydraulics [93]. An evaluation of the system loss is needed for each of these components to be designed properly.

A variable hydraulic transmission was modeled in a previous study [90]. The modeling was to find the loss from the driver joint to the driven joint by considering the mechanical friction, flow resistance, and compressibility of the fluid in cylinders and manifolds.

Hydraulic analogy or drain-pipe theory is a method relating flowrate and pressure

in a hydraulic circuit based on the flow resistance [62, 94]. There are two laws similar to Kirchhoff's laws for hydraulics. One is the algebraic sum of flowrate in a network meeting at a point is zero. The second law is the directed sum of the pressure differences around any closed loop is zero.

In this chapter, the mechanical performance of the joints with hydraulic cylinders and a cable-driven translational to rotational mechanism is evaluated. A hydraulic analogy is used to model the loss from the driver joint to the driven joint. Furthermore, the model is validated using experimental tests at various velocities and transmission ratios.

5.2 Methods

5.2.1 Force Transmission

To evaluate the friction in the system, the torque required to move the unloaded output at several transmission ratios was measured experimentally. A force gauge (Mark-10, M5-200) was used to measure the maximum force to pull a timing belt around a pulley at the input while the output was unloaded.

The torque transmitted to the output is

$$T_{transmitted\ to\ output} = T_{applied\ to\ input} - T_{friction} \tag{5.1}$$

where $T_{applied\ to\ input}$ is the torque applied at the input, and $T_{friction}$ is the friction torque in an unloaded configuration.

Figure 5.1 shows the setup used to test the torque transmission from input to output. The output was engaged with a calibrated spring ($T_{transmitted\ to\ output}$) while the torque required to move the output handle ($T_{applied\ to\ input}$) was measured at the input using the force gauge.

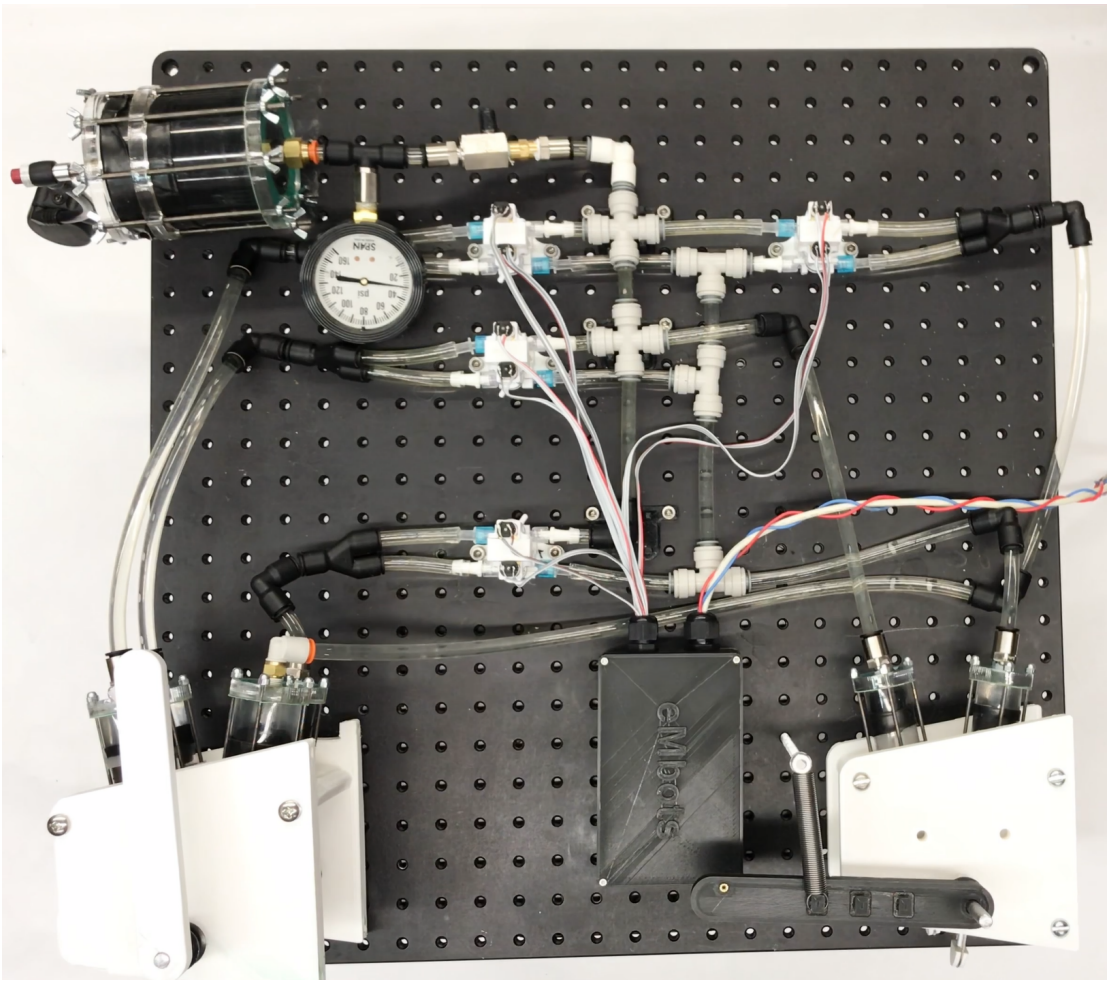

Figure 5.1: Output loaded with calibrated spring.

5.2.2 Force and Velocity Dependency

The unloaded output was moved by hand at two different velocities to evaluate the damping of the system. The velocity was tested using the encoder at the input joint. The maximum torque required to move the system at 5 and 80 deg/s was tested at different transmission ratios. The same test was conducted on the system from output to input at 5 and 80 deg/s.

5.2.3 Modeling Force Transmission

A superposition method was used to model the unloaded system loss. The model was validated at different speeds with the experimental results from the previous section. Figure 5.2 illustrates two sources of loss in the system. One was the mechanical friction in joints and cylinders, and one was the loss across the hydraulic setup, including the hoses, valves, fittings, and fluid entrances and exits.

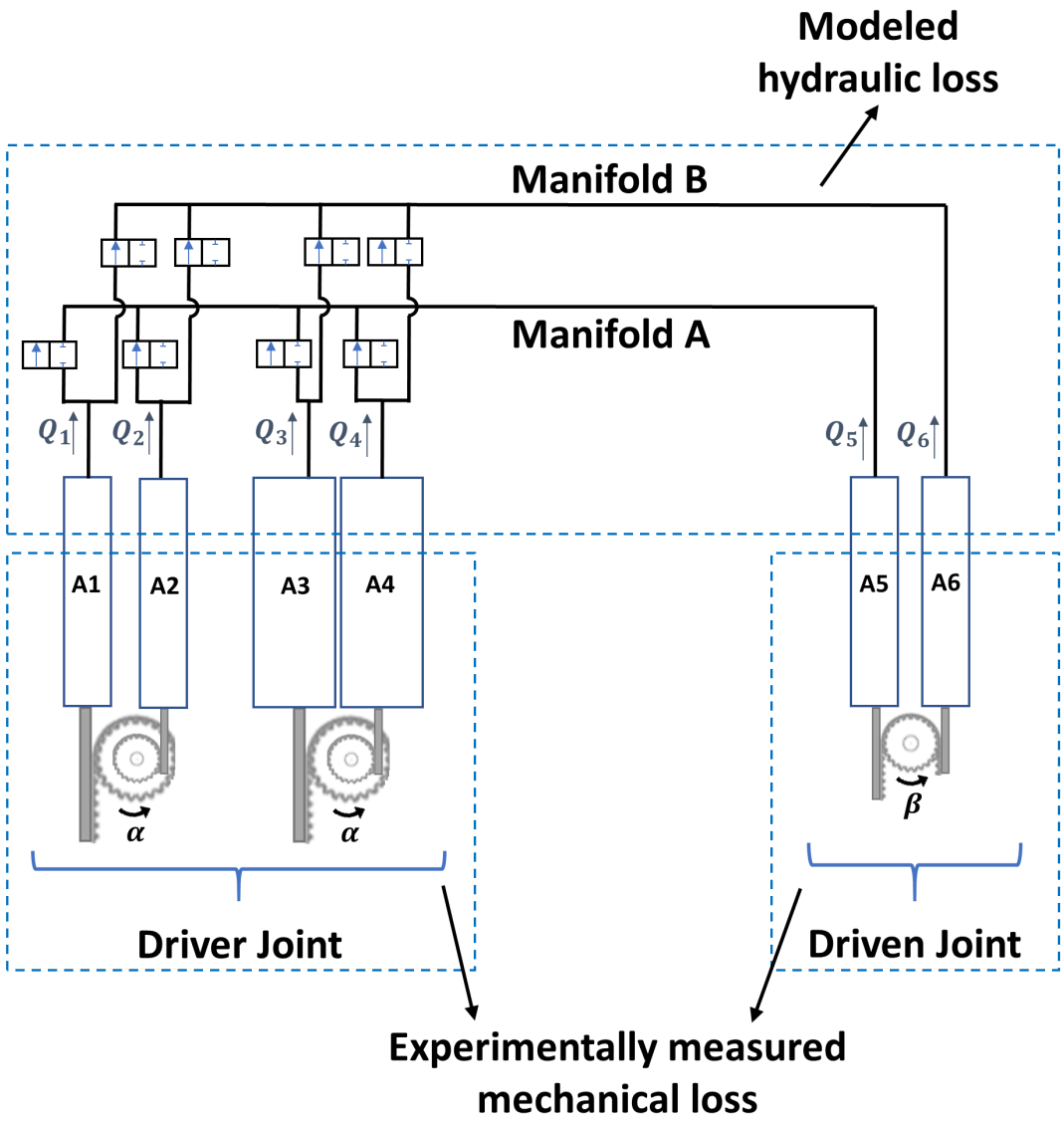

Figure 5.2: The superposition method to model the loss of the system. The total loss is the superposition of the hydraulic system losses and joint mechanical losses.

The loss in the two mechanical joints, including the cylinders, was measured experimentally. Characterizing the losses in the system allows finding the force transmission in the system. To remove the effect of the hydraulic losses, all cylinders at the input and output were connected with a short length of hoses, and the cylinders were pressurized

with air. Cylinders were pressurized for the cable pulley mechanism to be tightened and provide the same performance. Since $1^T J$ was zero, $A_1 D_1 - A_2 D_2 + A_3 D_3 - A_4 D_4$ and $A_5 D_5 - A_6 D_6$ were zero, and torque equilibrium were met at the joints. A_i is the cylinders' effective area, and D_i is the pulley diameter. Figure 5.3 shows the circuit where the input cylinders and output cylinders are connected and pressurized to 200 kPa.

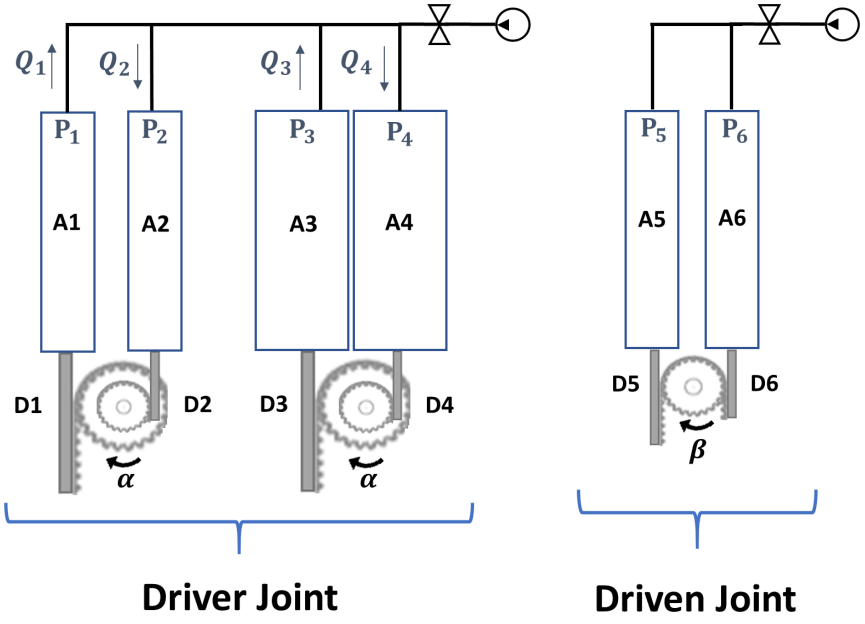

(a) Input joint.

(b) Output joint.

Figure 5.3: The pneumatic setup to test the mechanical friction at joints.

The other source of the loss (from hydraulics) can be modeled and be added to the mechanical loss. To model the loss in a hydraulic unit, the flowrate of the fluid and the fluid properties and system geometries were needed. Different lines of the system had different components and geometries. In some lines, there were valves and a higher number of fittings. Therefore, the system had to be split into separated lines with a relative flowrate. A hydraulic analogy similar to the Kirchhoff's law in electric circuits was used to relate the flowrate and the cylinders' pressure.

For example, to model the loss in hydraulic system for transmission ratio of 1:1 from input to output depicted in Figure 5.4. The net flowrate into two fluid intersections

was set to be zero. Furthermore, since the $1^T J$ was zero and no mechanical loss was assumed, $A_5 D_5 - A_6 D_6$ was zero, and the flowrate in lines 6 and 2 were equal (Equation 5.2). For the input speed of 5 and 80 deg/s, the Q_1 can be calculated from Equation 4.1.

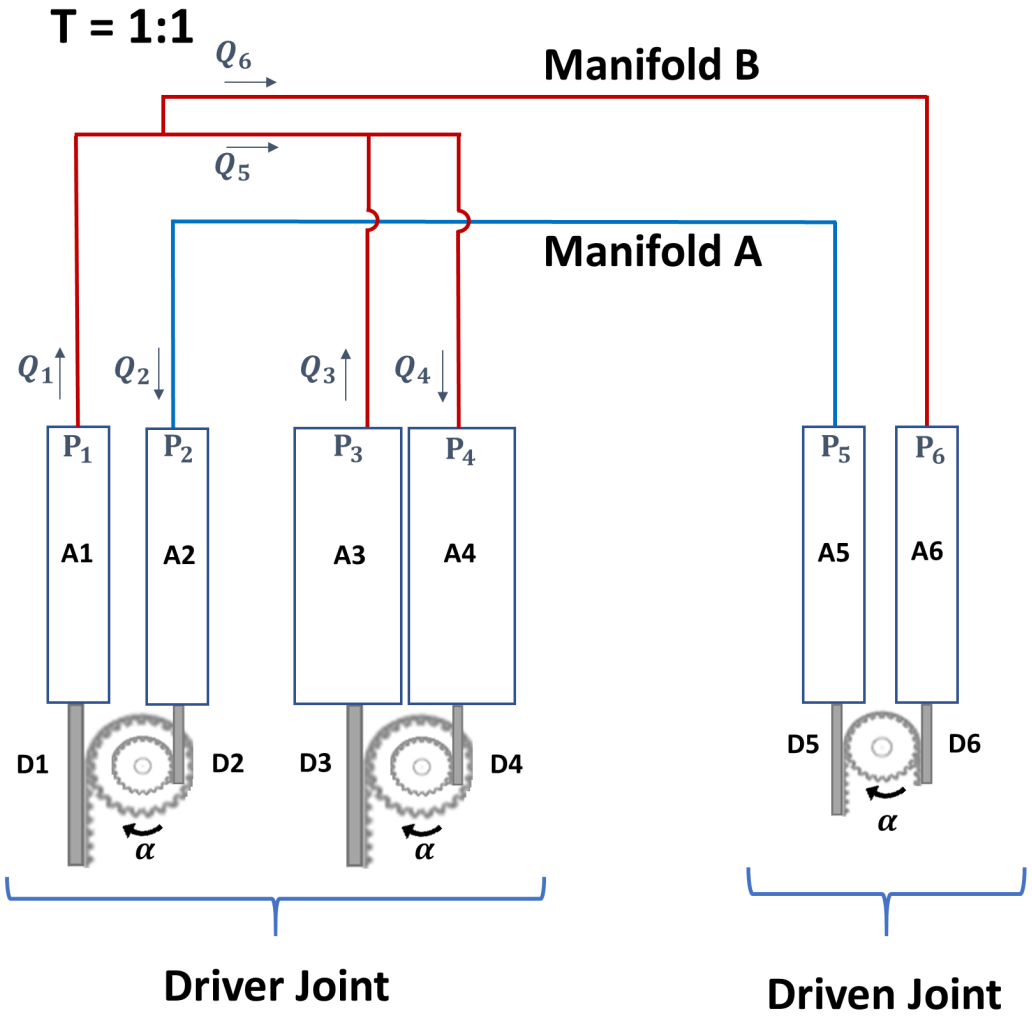

Figure 5.4: The hydraulic circuit for the transmission ratio of 1:1.

$$
\begin{aligned}
Q_1 &= Q_5 + Q_6 \\
Q_5 + Q_3 &= Q_4 \\
Q_6 &= Q_2
\end{aligned}
\tag{5.2}
$$

Assuming there was no mechanical loss at the joints, the torque measured at the input while being moved provides pressure in cylinder 1 (P_1). The loss at each line was calculated by the flowrate calculated in Equation 5.2. Based on the Kirchhoff's law, the pressure at other cylinders can be written based on P_1 (Equation 5.3).

$$
\begin{aligned}
P_1 - L_1 - L_5 - L_4 &= P_4 \\
P_1 - L_1 - L_5 + L_3 &= P_3 \\
P_1 - L_1 - L_6 &= P_6 \\
P_5 &= P_6 \\
P_5 - L_2 &= P_2
\end{aligned}
\tag{5.3}
$$

The pressure loss can be found from .

$$
L_i = \Delta P = K\frac{V^2}{2g} \tag{5.4}
$$

where V is the flow velocity, g is the gravitational acceleration, and K factors are listed in Table 5.1 [95, 96, 97].

Table 5.1: K factors for the pressure drop across the hydraulic components.

	Hose	Valve	Elbow	Tee	Entrance	Exit
K	$f\frac{L}{D}$	$(1.2 + \frac{160}{Re})((\frac{D}{d})^4 - 1) + 2(1 - (\frac{d}{D})^4)$	1.3	1	0.5	1

Re is the Reynolds number, f is $\frac{64}{Re}$ for laminar flow, L is the hose length, D is the hose diameter (6.35 mm) and d is the valve orifice diameter (1.82 mm). Each valve was considered as square reduction to the valve diameter ($(1.2 + \frac{160}{Re})((\frac{D}{d})^4 - 1)$) and a square expansion back to the hose diameter ($2(1 - (\frac{d}{D})^4)$).

The torque measured at the input joint is

$$
T = P_1(A_1D_1) - P_2(A_2D_2) + P_3(A_3D_3) - P_4(A_4D_4) \tag{5.5}
$$

Using the pressure drop equations, the pressure at each cylinder can be derived with respect to P_1 from Equation 5.3.

$$\begin{aligned} T = {} & P_1(A_1D_1) - (P_1 - L_1 - L_6 - L_2)(A_2D_2) + \\ & (P_1 - L_1 - L_5 + L_3)(A_3D_3) - (P_1 - L_1 - L_5 - L_4)(A_4D_4) \end{aligned} \tag{5.6}$$

or to simplify

$$\begin{aligned} T = {} & P_1(A_1D_1 - A_2D_2 + A_3D_3 - A_4D_4) + (L_1 + L_6 + L_2)(A_2D_2) \\ & - (L_1 + L_5 - L_3)(A_3D_3) + (L_1 + L_5 + L_4)(A_4D_4) \end{aligned} \tag{5.7}$$

Since $1^T J$ was zero, $A_1D_1 - A_2D_2 + A_3D_3 - A_4D_4$ was zero, and the torque measured at the input for the loss in hydraulics only depended on the geometry of the mechanical and hydraulic systems, manipulation speed, and fluid properties (Equation 5.12).

$$T = (L_1 + L_6 + L_2)(A_2D_2) - (L_1 + L_5 - L_3)(A_3D_3) + (L_1 + L_5 + L_4)(A_4D_4) \tag{5.8}$$

The same method was used to find the hydraulic loss at other transmission ratios or if the system was used reversely. For example, for the same transmission ratio, a similar method can be used to model the torque to overcome the hydraulic loss from output to input (Measuring the torque required to move the unloaded system from output to input.) Assuming there was no mechanical loss at the joints, the torque measured at the output while being moved, provides pressure in cylinder 5 (P_5). The flowrate was described in Equations 5.2. Assuming $P_1 = P_5 + \delta$, where δ can be positive or negative and the pressure equations can be written as

$$\begin{aligned} P_6 &= P_1 - L_1 - L_6 = P_5 + \delta - L_1 - L_6 \\ P_4 &= P_5 + \delta - L_1 - L_5 - L_4 \\ P_3 &= P_5 + \delta - L_1 - L_5 + L_3 \\ P_2 &= P_5 - L_2 \\ P_1 &= P_5 + \delta \end{aligned} \tag{5.9}$$

Since zero mechanical loss at the input joint was assumed, then $P_1(A_1D_1) - P_2(A_2D_2) + P_3(A_3D_3) - P_4(A_4D_4) = 0$, and $A_1D_1 - A_2D_2 + A_3D_3 - A_4D_4 = 0$, P_5 would be out of

the equation, and δ can be found as

$$\delta = \frac{(-L_2)A_2D_2 + (L_1 + L_5 - L_3)A_3D_3 - (L_1 + L_5 + L_4)A_4D_4}{A_1D_1 + A_3D_3 - A_4D_4} \tag{5.10}$$

The torque measured at the input joint is

$$T = P_5(A_5D_5) - P_6(A_6D_6) = P_5(A_5D_5) - (P_5 + \delta - L_1 - L_6)(A_6D_6) \tag{5.11}$$

and since $A_5D_5 - A_6D_6 = 0$, the torque can be simplified to

$$\begin{aligned} T &= (L_1 + L_6 - \delta)(A_6D_6) \\ &= (L_1 + L_6 - \frac{(L_1 + L_5 - L_3)A_3D_3 - (L_1 + L_5 + L_4)A_4D_4 - L_2A_2D_2}{A_1D_1 + A_3D_3 - A_4D_4})(A_6D_6) \end{aligned} \tag{5.12}$$

Once again, the friction torque in the input joint only depended on the geometry of the mechanical and hydraulic systems, manipulation speed, and fluid properties. The torque from the superposition of hydraulic modeling results and mechanical joint friction was verified at different velocities and transmission ratios with the experimental results.

5.3 Results

5.3.1 Force Transmission

Figure 5.5 indicates the torque required to move the input (with 4 cylinders) and output (with 2 cylinders) to a particular angle when the hydraulic transmission was not engaged. The system was unloaded, and the torque shown in this figure was only coming from the mechanical joints and the long-stroke rolling diaphragm cylinders.

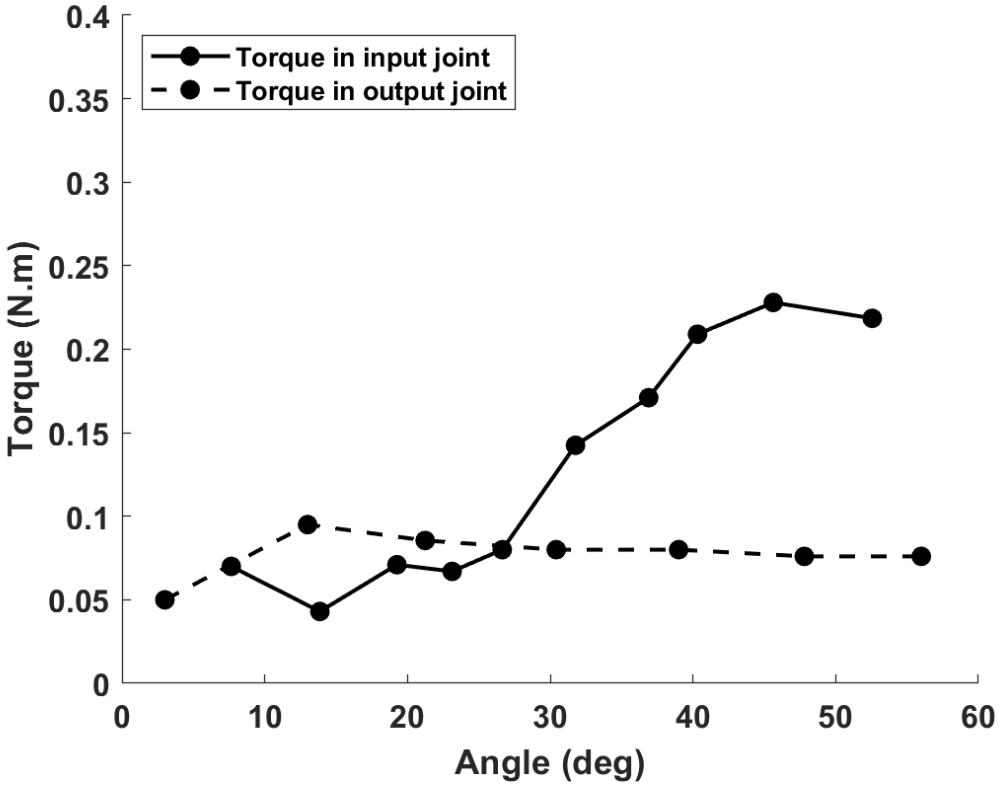

Figure 5.5: The torque required to overcome the mechanical friction at joints.

The torque transmission from one side to another was tested using a calibrated spring attached to the handle at the output and recording the torque required to move the input joint.

The torque transmission of the loaded system is shown in Figure 5.6. The error of the loaded torque transmission closely matched the friction in the system.

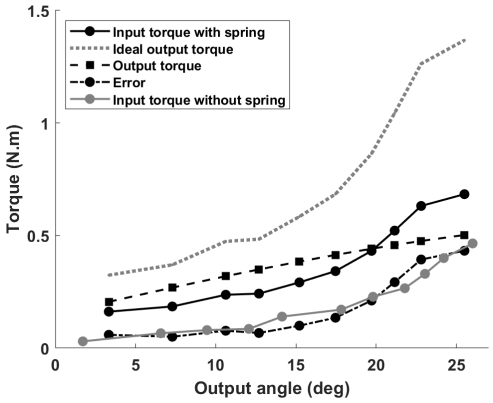

(a) Transmission ratio of 1:0.5.

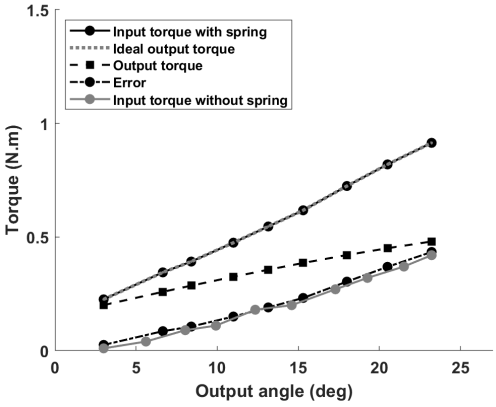

(b) Transmission ratio of 1:1.

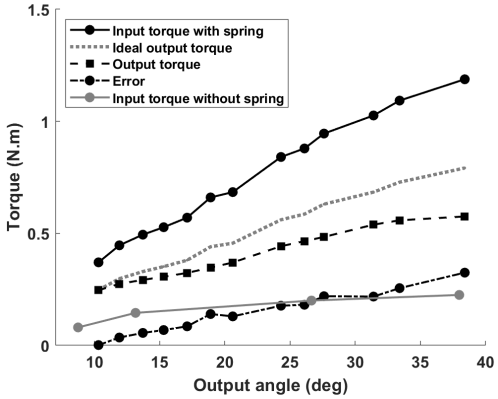

(c) Transmission ratio of 1:1.5.

Figure 5.6: Force transmission in loaded and unloaded system. The grey solid line illustrates the torque required to move the input when the transmission was engaged, but the system was unloaded at the output at three transmission ratios.

5.3.2 Force and Velocity Dependency

The maximum experimental torques recorded to move the unloaded system from input to output at low and high speed for three transmission ratios are depicted in Figure 5.7.

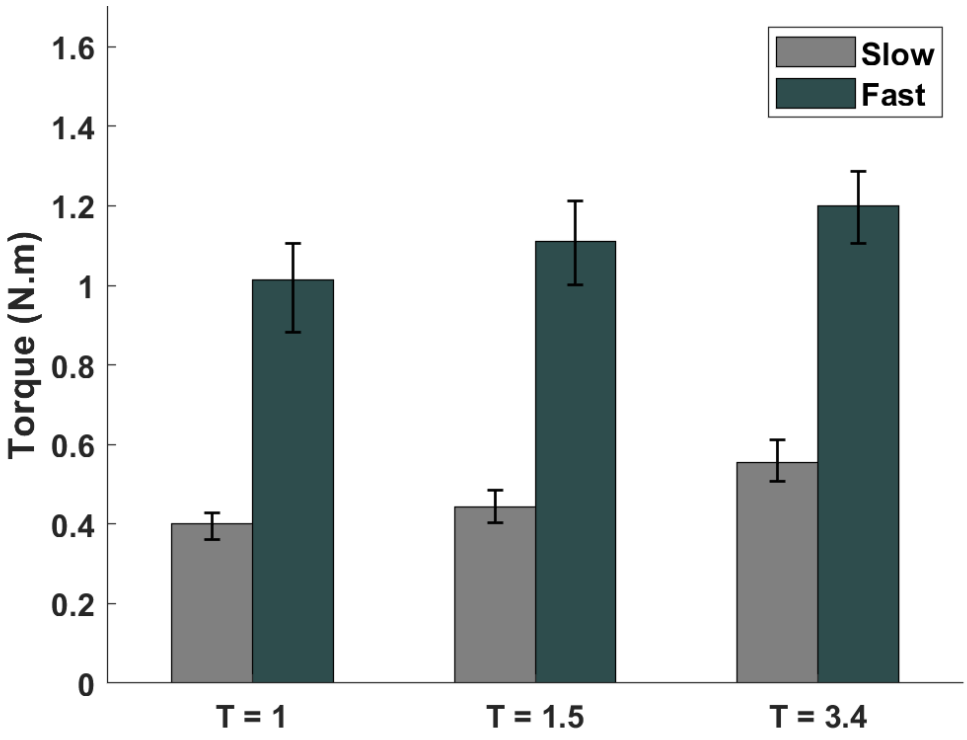

Figure 5.7: The maximum torque required to move an unloaded system from input to output. The slow velocity was 5 deg/s and the fast velocity was 80 deg/s

Lower velocity dependency can be seen in the maximum torque recorded to move the system from output to input. Figure 5.8 shows the maximum torque required to move the system from output to input for three transmission ratios.

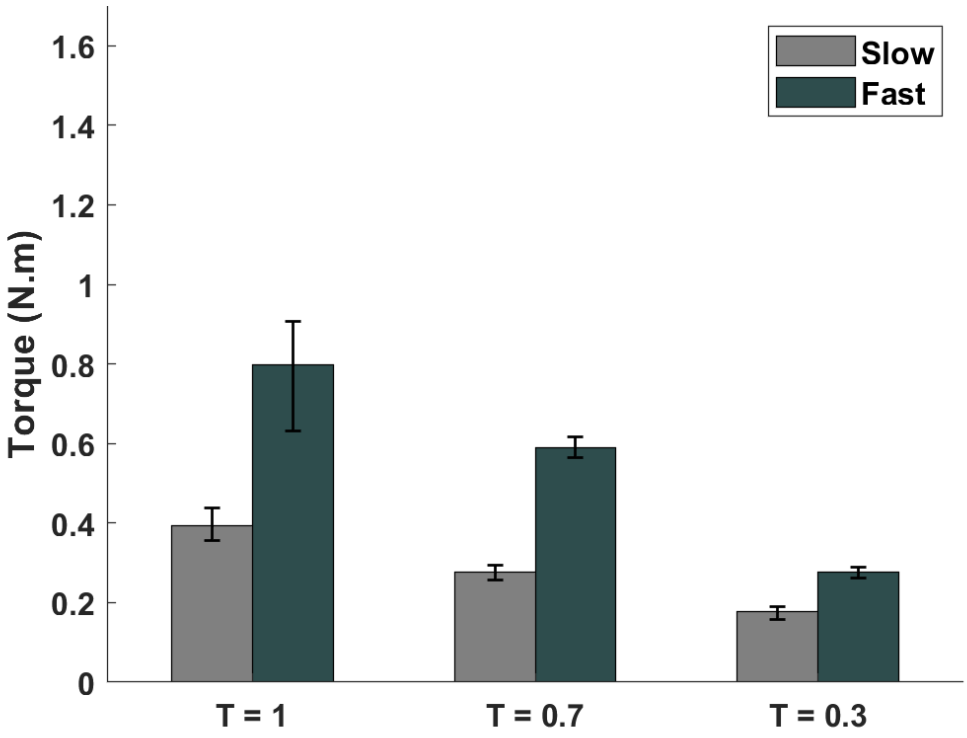

Figure 5.8: The maximum torque required to move an unloaded system from output to input.

5.3.3 Modeling Force Transmission

The overall torque measured experimentally to move the unloaded system from the input to the output and reversely were reported in Figures 5.7 and 5.8. The modeling discussed in the methods was used to calculate the losses in the hydraulic system. The superposition of the calculated hydraulic losses and the experimentally measured mechanical losses in joints and cylinders are shown in Figure 5.9 for the input to output and in Figure 5.10 for output to input.

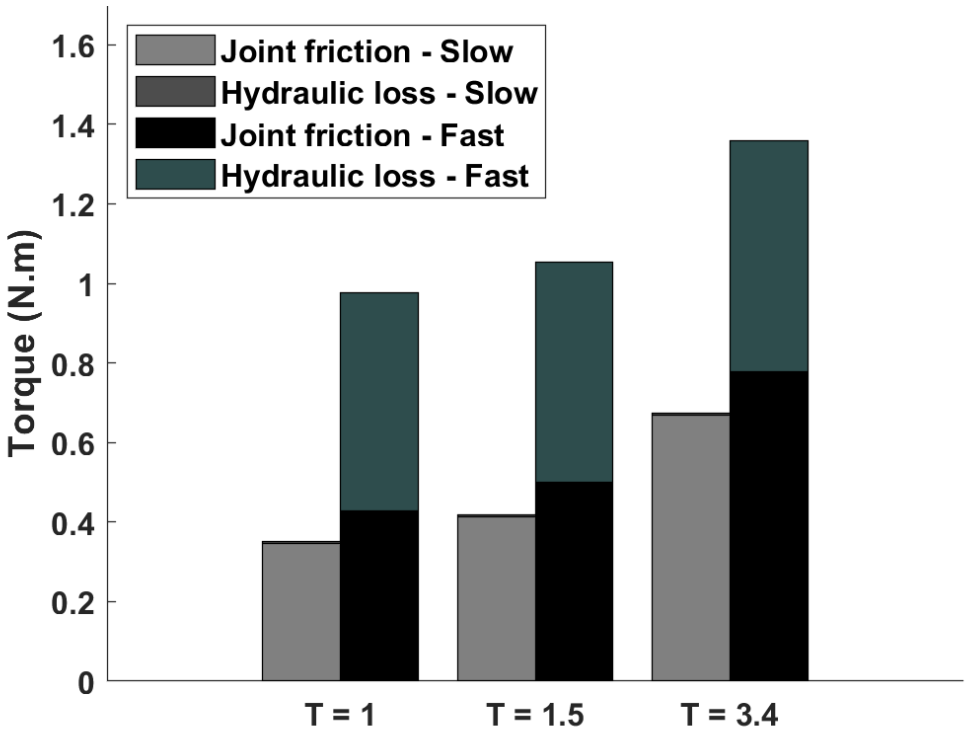

Figure 5.9: The modeling results for the maximum torque required to move an unloaded system from input to output.

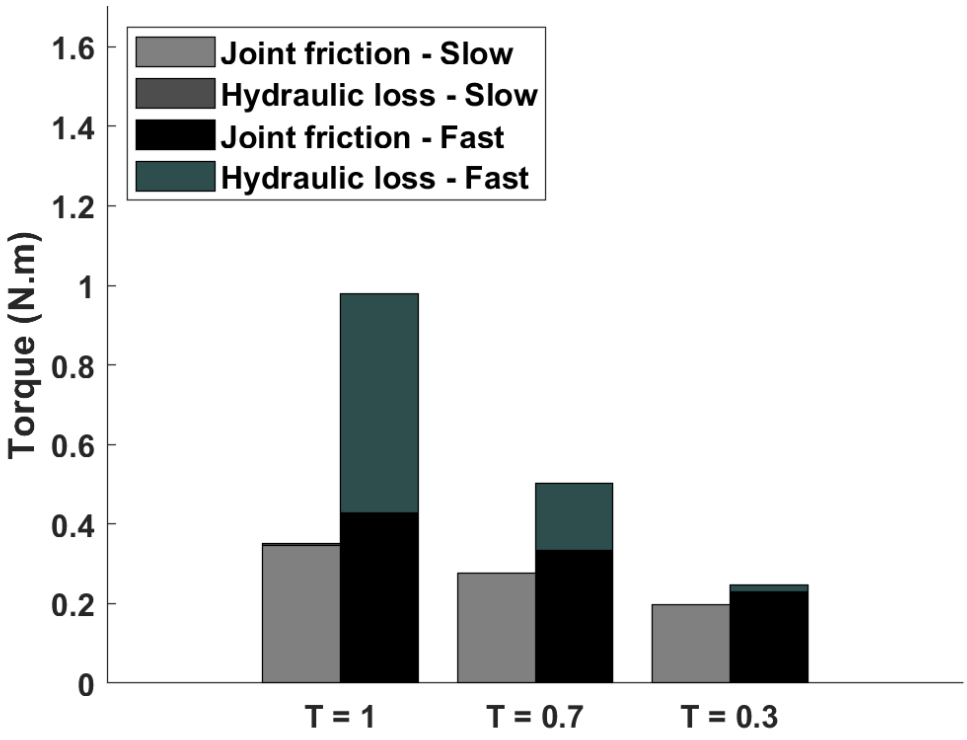

Figure 5.10: The modeling results for the maximum torque required to move an unloaded system from output to input.

The force-velocity dependency for both cases matches the experimentally measured data reported in Figures 5.7 and 5.8.

5.4 Discussion

The mechanical friction at both joints is shown in Figure 5.5. The torque at the output angle that only had two identical cylinders and pulleys was consistent through the range of motion. However, the torque at the input with four cylinders and pulleys increased with the angle. The inconsistency in the performance of the input joint affected the overall transmission's performance. Multiple errors cause the system to not accurately meet the Equation 4.7 ($1^T J = 0$). The Jacobian J was dependant on the cylinders' effective areas and pulleys' diameters. A geometry error in the manufacturing of the

diaphragms, cylinders, and pulleys and possible misalignment of each pulley and cable pair are some of the reasons for the springiness of the input joint.

The loss in the force transmission from input to output comes from the mechanical joints, rolling diaphragm cylinders, and the hydraulic circuit. The torque required to move the unloaded system should match the error in force transmission of the loaded system. This can be seen in Figure 5.6 as the error between the ideal output and the experimental output closely match the torque required to move the unloaded system (grey solid line). The objective of refining the system is to minimize this error or the loss in the unloaded system (to drop the grey solid line to zero).

Figures 5.7 and 5.8 illustrates the damping in the system as the torque depends on the speed of manipulation. The configuration setup used for three different transmission ratios is similar for both figures. For example, for both the cases of transmission ratio of 1:1.5 in Figure 5.7 and transmission ratio of 1:0.7 in Figure 5.8 the speed of the joint with two cylinders was 1.5 times the speed of the joint with four cylinders on. The angular velocity of the joint with four cylinders (eight valves were used on this side of the transmission) at slow and fast speeds were 5 and 80 deg/s in Figure 5.7. However, in Figure 5.8, the speed of the joint with two cylinders (no valves were used in this side of the transmission) at slow and fast speed were 5 and 80 deg/s. The effect of the pressure drop across the valves can be seen here as the higher force, and velocity dependency can be seen in cases that higher speeds were at the fluid lines with valves (comparing transmission ratio of 1:3.4 from input to output and 1:0.3 from output to input).

The superposition of the hydraulic losses and mechanical joint friction reported in Figures 5.9 and 5.10 closely matched the results experimentally measured and reported in Figures 5.7 and 5.8.

5.5 Conclusion

The force transmission for the system was tested and modeled in this chapter. The difference between the applied torque at the input and the measured torque at the output closely matches the friction of an unloaded system. The torque-position relationship of the input joint with four cylinders and pulleys is not consistent, and that inconsistency proceeds to the device's efficiency. The output with two cylinders has an invariable

torque-position performance. Component manufacturing with a higher accuracy could improve the system efficiency.

A hydraulic analogy based on Kirchhoff's law was used to model the loss in the hydraulics system. A superposition method for the modeled hydraulic loss and experimentally measured loss at joints was used to find the maximum torque required to overcome the loss of an unloaded system. An experimental test on the torque required to move the unloaded system at different velocities verifies the model described. Valves with relatively small orifice sizes affect the system's dynamic performance as the small orifice size increases the damping of the system. The lower velocity dependency can be seen at output lines with no valves compared to the input with eight valves. The model described matched the experiments and can be used to evaluate any variable hydraulic transmission and allow improvement in the performance by designing proper components.

Chapter 6

Antagonist transmission with bending soft robots

6.1 Introduction

Conventional rigid body robots are used in human-robot interaction; however, they lack conformality, and the rigid links and joints make them unsafe for interaction with human beings. Softness and compliance enable biological systems to safely interact with the environment, and this compliance is found in soft robots [98]. Pneumatic and hydraulic soft bending elastomeric actuators with flexible embedded materials are promising options for robotic applications because they are light and can be controlled.

One application of a soft robot is manipulating objects, for example, remote manipulation in a leader-follower configured puppet or surgical robot. This keeps a human in the loop, which is a safer mode of manipulation than completely automatic control [99]. Pneumatic soft robots were used in an active hand to copy the motion of a leader to achieve different grasps [100]. Here, the fingers were actuated and controlled using a pneumatic pump connected through on-off valves. In two other studies, tendon-actuated hands were designed to mimic the human hand using servo motor actuation [101, 102]. A low-profile haptic glove using electrostatic brakes was proposed with the glove capable of generating up to 20 N per finger to allow haptic feedback in a VR grasping task [103].

A realistic and complex design can lead to artificial limb regeneration; however, a more straightforward design can help to achieve an uncomplicated actuation method

in addition to reasonable haptic feedback from a soft hand. Hydraulics can bring both actuation and haptic features in one intuitive setup.

Due to the high power density of hydraulics, hydraulic soft fingers can be used to implement a lightweight hand with independent movement in each finger. The advantages of hydraulics over pneumatics, including high power to weight density, low backlash, and incompressibility, are evident in a passive closed system.[104] A hydraulic transmission was described in previous chapters for a rigid leader-follower robot. Furthermore, it was concluded that the friction in rolling diaphragm cylinders is low compared to traditional o-ring cylinders for low-pressure applications. As discussed before, one of the main application of the leader-follower robot is human/robot interaction. The system provided high-bandwidth haptic feedback to the operator. This haptic information allows for high-quality human-robot interaction. Replacing the follower side of the transmission with a soft robot makes it more conformal; however, the compliance of the soft robot can decrease the bandwidth and haptic feedback that the operator gets from the follower side, reducing its utility for puppeteering. For example, previous bending soft robots used in grasping hands had low stiffness and bandwidth due to their fully elastomeric structure [100, 105, 106].

People find a robot to be more trustworthy if the robot is more human-like [107]. Therefore, to make the appearance and motion of a soft robot finger match that of a human finger, the stiffness and natural frequency of the soft robot must be increased. Placing a strain-limiting layer on one side of a bending soft robot or wrapping it with a thread are examples of restrictions that make a soft robot more controllable [108]. The material properties of the elastomer, geometry of the soft robot, and wrapping thread pitch and angle all affect the pressure required to reach a specific angle [109]. For example, the actuation pressure to attain 360-degrees of rotation for a 160 mm fabric-reinforced bending soft robot is about 250 kPa (35 psi) [109]. The pressure required to actuate a soft robot in a leader-follower grasping hand must be low enough to enable smooth and comfortable actuation by the operator. The soft robot can be made with a softer elastomer to decrease the actuation pressure; however, the robot's stiffness will decrease. One method for increasing stiffness is to add a sleeve over the soft robot finger, which does increase the stiffness but comes at the expense of higher actuation pressure [110]. Hence there remains a need for a bending soft robot with high stiffness

and low actuation pressure.

Our approach to solving this problem is to embed rigid structures into a fiber-reinforced bending soft robot finger to increase stiffness and natural frequency and add motion controllability to the device without increasing the actuation pressure. We call this a bone-inspired soft robot.

To demonstrate the capability of bone-inspired soft robots, we designed, built, and evaluated a leader-follower puppeteering robot (Figure 6.1). This passive puppet contains hydraulic transmissions that couple each leader finger with its corresponding follower finger, with a rolling diaphragm cylinder in the leader finger. The four-fingered puppet hand can interact with other humans and can perform several grasps and gestures, all with a relatively simple design. As shown in the figure, different shapes of objects were used to understand how well the puppet's hand could grasp. In operation, the puppeteer was able to feel if any of the fingers were engaged with the object and was also able to gain a general sense of the object's shape.

While we have used the puppet for demonstrations to fully take advantage of bone-inspired soft robots, mathematical models that describe this unique structure are needed to create new designs that optimize static and dynamic performance. The development and validation of these models was the objective of the study, whose results are reported in this chapter.

Static evaluation of traditional bending soft robots has been previously studied to provide force and angle as a function of actuation pressure [109] and force as a function of the input volume [111]. Some analyses of the dynamic performance of soft robots have also been conducted. For example, a one-DOF mass-spring model was used to conduct a dynamic characterization of a soft robotic arm equipped with pneumatic artificial muscles [112], and a 2-DOF mass-spring-damper system was used to model an earthworm-inspired soft crawling robot [113]. Another study modeled the natural frequency of a single-link soft finger using finite element analysis and found the lowest natural frequency for the finger to be about 2.5 Hz [114]. Low natural frequency leads to a problematic resonance in many applications, including puppeteering.

Still, another study used a model to predict the trajectory taken by the tip of a fiber-reinforced soft bending robot that was sectioned into several segments with different fiber arrangements [115]. The trajectory was predicted using the models suggested for

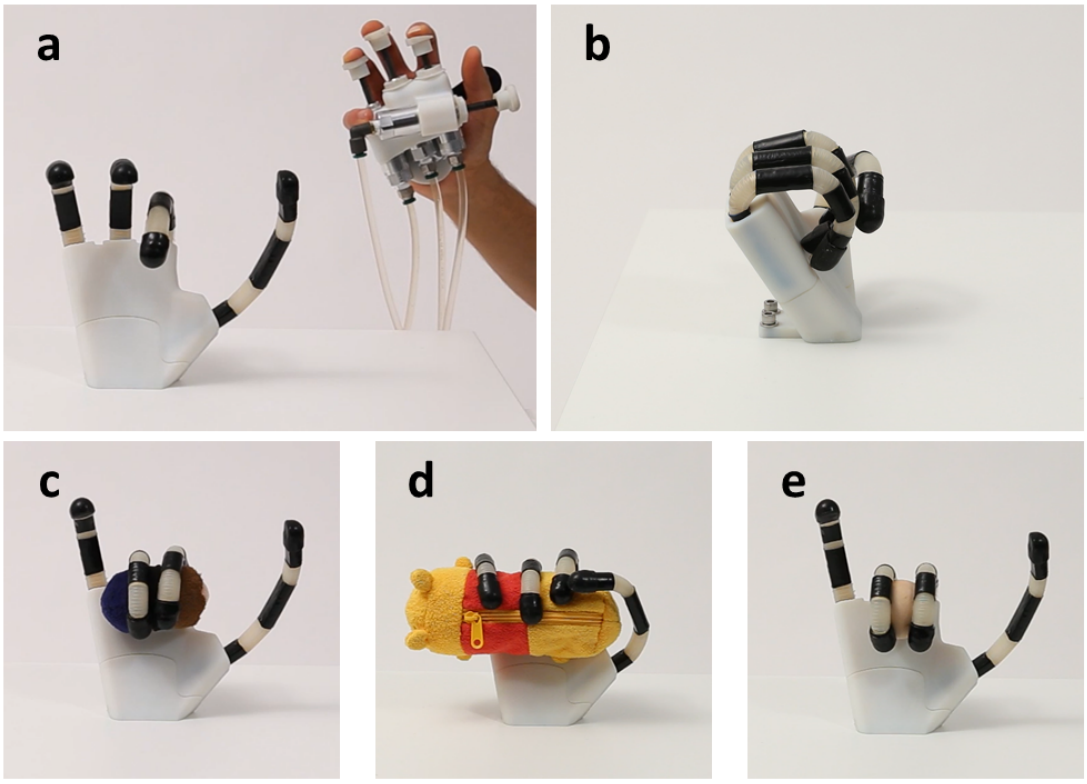

Figure 6.1: leader-follower hand puppet made with bone-inspired soft robot fingers. (a) Front view of the hand and puppeteering glove. (b) Side view of the hand in the closed pose. (c) Small soft doll grasping with two fingers. (d) Large soft doll grasping with four fingers. (e) Wooden ball grasping with two fingers.

extension, expansion, bending, and twist segments [115]. The trajectory prediction for bone-inspired soft robots suggested here is a simpler trajectory planning method controlled by the segments' lengths.

The following sections describe how to fabricate a bone-inspired soft robot, the development and experimental validation of a second-order mass-spring-damper model to describe bone-inspired soft robot dynamics, and the development of a geometric model combined with the trajectory model of a traditional bending soft robot describing bone-inspired soft robot trajectories.

6.2 Methods

6.2.1 Bone-Inspired soft robot manufacturing process

The manufacturing process for a bone-inspired soft robot (Figure 6.2) is a modified version of the process for making conventional fiber-reinforced bending soft robots as described in the soft robotic toolkit.[108] The bones (with an elastic modulus of 2300 MPa) were placed on a half-round, which in turn was placed inside a mold, and elastomer (Smooth-On Dragon Skin 10 Medium, with an elastic modulus of 150 kPa) was added to cure. A strain-limiting fiberglass cloth was glued to the flat side of the elastomeric half-round tube to restrict extension. The tube was wrapped with 0.36 mm diameter Kevlar thread to restrain the radial strain. The bone areas were fully wrapped to seal the gap between the bone and elastomeric skin from the pressurized fluid. Without this wrapping, the elastomer on the top of the bone can separate and bulge at high pressure. The wrapped tube was placed into a second mold, and elastomer (Smooth-On Dragon Skin 10 Medium) was added to form a thin skin. The rod was removed, and one end of the tube was plugged with a stiffer elastomer (Smooth-On Dragon Skin 30, with an elastic modulus of 590 kPa). A vented screw was installed and sealed using silicone glue (Smooth-On Sil-Poxy). Finally, the opposite end of the tube was plugged with the stiffer elastomer and sealed with glue. A covering skin formed from a heat-shrink tube can be optionally applied for the final appearance of the finger.

In addition, a four-finger puppeteering hand was fabricated from bone-inspired robots and additional 3D-printed structures (Figure 6.1). A hand pump was used to pre-pressurize the fingers, and manual switching valves were used to isolate each finger

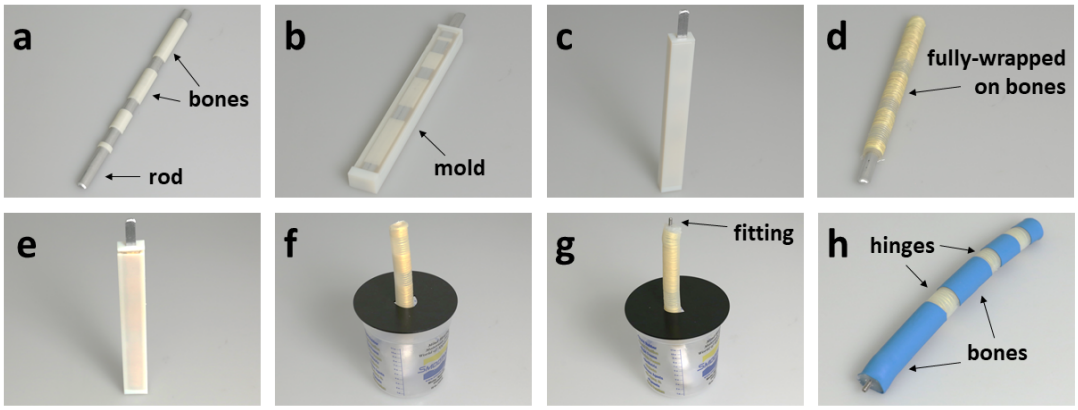

Figure 6.2: Manufacturing process for constructing a bone-inspired soft robot. (a) Place plastic bones on the half-round rod. (b) Place the rod on the mold and add elastomer. (c) Keep the mold upright to cure. (d) Add fiberglass cloth to the flat side and wrap the soft tube with Kevlar thread. (e) Repeat steps 2 and 3 with the second mold to add skin. (f) Remove the rod and plug one side of the tube. (g) Add the vented screw as the fitting and plug the other side. (h) Add the shrink tubes to the bone areas for the final appearance.

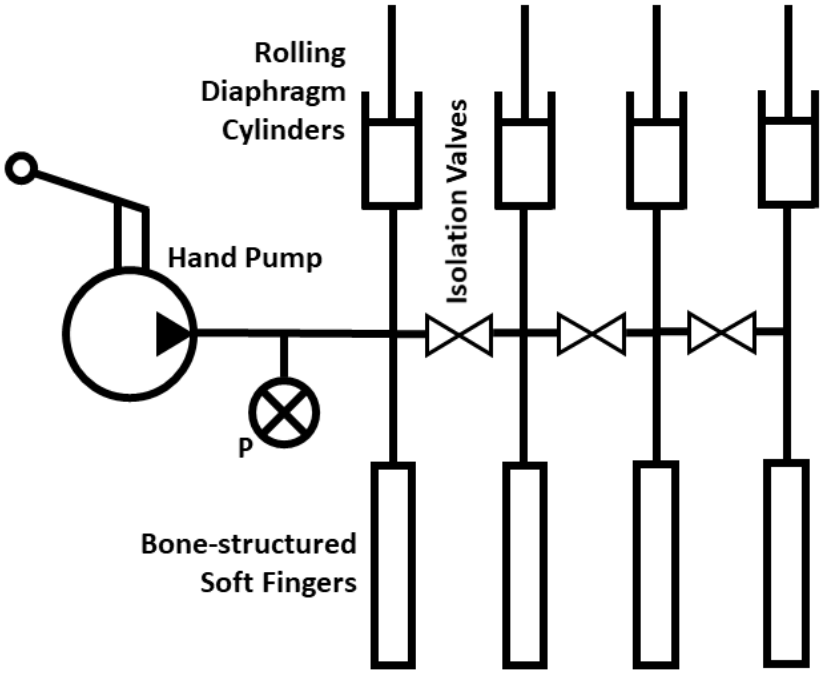

Figure 6.3: Hydraulic circuit for the puppeteering hand.

(Figure 6.3). Four rolling diaphragm hydraulic cylinders were placed in the leader glove operated by the puppeteer, with each hydraulic cylinder actuating its corresponding soft finger.

Bone configurations

Figure 6.4 shows four bending soft robots fabricated for performance testing: (1) A regular fiber-reinforced bending soft robot with no bones (NB). (2) A bone-inspired soft robot with three bones with the shortest bone as the first bone and longest at the end (3B, SBF). (3) A bone-inspired soft robot with three bones with the longest bone as the first bone and shortest at the end (3B, LBF). (4) A bone-inspired soft robot with four bones embedded to mimic human's finger (4B).

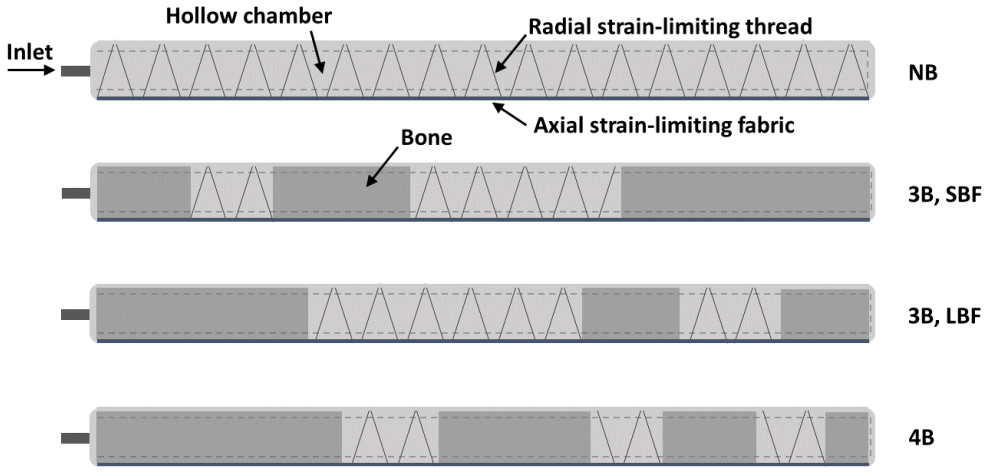

Figure 6.4: Bone configuration in four bone-inspired soft robots. No bone (NB), 3-bone with short bone at first (3B, SBF), 3-bone with long bone at first (3B, LBF), and 4-bone (4B) soft robots.

6.2.2 Performance tests

Stiffness

A displacement test machine (ElectroForce 3200) was attached to the rolling diaphragm cylinder rod to control the position of the piston (Figure 6.5 (a)). The initial pressure of the system was set using a water or air pump. Reflective markers were placed on the base and the tip of the finger to measure the tip-to-base angle, and the motion was captured using a video camera. The piston was lowered by the test machine at a constant velocity (2 mm/s) to increase the pressure and angle. A 690 kPa pressure transducer (SSI Technology, P51-100-G-B-I36-4.5V-000-000) was used to measure pressure while the piston displacement was recorded by the test machine. The stiffness of four bending soft robots was estimated by the best-fit line of the force-displacement data.

Natural frequency

A sinusoidal movement of the test machine resulted in an approximately sinusoidal pressure and movement of the finger. It was used to find the frequency response of the

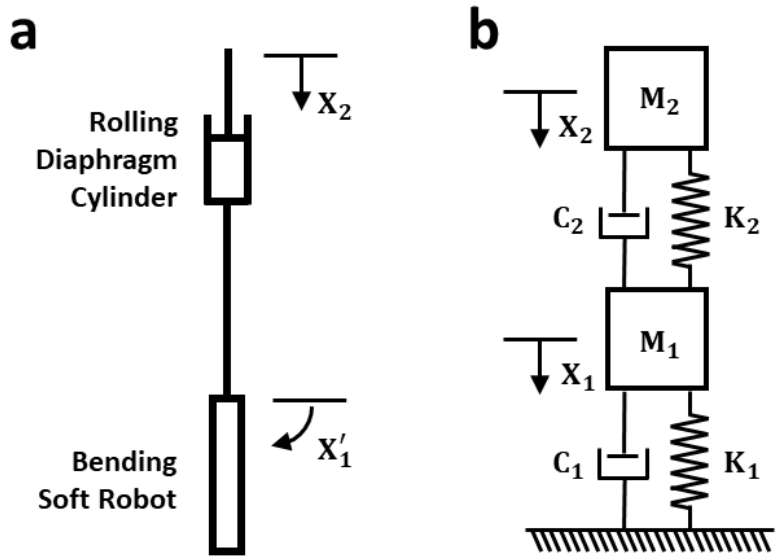

Figure 6.5: (a) Bending soft robot actuated with a cylinder. (b) Equivalent mass-spring-damper system.

four bending soft robots. The test was performed at frequencies from 0.5 to 7 Hz at 34 and 69 kPa pre-pressures.

Trajectory

To validate a model for finger trajectory with applied pressure (model described below), the trajectory of the fingertip was measured using the experimental setup shown in Figure 6.5 (a). The cylinder was attached to a displacement test machine to modulate the pressure. The flowrate was fixed by the displacement of the input cylinder and set to be at 0.2 cc/s. Since the model does not account for gravity, the soft robot finger was placed horizontally on a Teflon-wrapped plate lubricated with mineral oil to lower the friction and remove forces associated with the gravity. Reflective markers were placed at every corner of the bones, and the motion was captured with a video camera. A pressure transducer was used to measure the pressure.

6.2.3 Stiffness and natural frequency model

A second-order mass-spring-damper system was used to model the soft robot and cylinder circuit (Figure 6.5). Displacement X_2 is translational and $X_1^{'}$ is rotational. The pressure at the cylinder was used as an estimator of the force. The spring coefficients are described by

$$K_1 = \frac{PA}{X_1^{'}} \tag{6.1}$$

$$K_2 = \frac{PA}{\alpha X_2 - X_1^{'}} \tag{6.2}$$

where K_1 is the finger stiffness, K_2 is the fluid stiffness, P is the pressure, A is the rolling diaphragm cylinder effective area, and α is a coefficient that transforms translational to rotational displacement. A least squares method based on experiment data was used to estimate an α to have a similar fluid stiffness for air or water in all the tests.

The equivalent translational mass for M_1 was calibrated using Equation 6.3, which is a linear superposition of the finger mass ($M_1^{'}$) and the system water or air mass ($M_2^{'}$).

$$M_1 = I(\alpha_M M_1^{'}) + (1 - I)(\beta_M M_2^{'}) \tag{6.3}$$

where α_M and β_M are scalers needed to transform between rotational and translational units, and I is the relative weight of the two masses.

The displacement of M_1 for a known displacement of M_2 is

$$\frac{X_1}{X_2} = \frac{C_2 s + K_2}{M_1 S^2 + (C_1 + C_2)s + (K_1 + K_2)} \tag{6.4}$$

and the natural frequency is

$$\omega = \sqrt{\frac{(K_1 + K_2)}{M_1}} \tag{6.5}$$

Values for I, α_M, and β_M were estimated from experimental data using the least squares method for the natural frequency shown in Equation 6.5. The assumptions for the stiffness and natural frequency model include linear stiffness for the joints and lumped mass for the fluid and the soft robot. The gravity was neglected in this model.

6.2.4 Trajectory model

A three-link rigid body model was used to analyze the movement of the bone-inspired soft robot. As shown in Figure 6.6, θ is the joint angle, L' is the bone length, L'' is a length that varies with θ, and L is the length of the equivalent link in the rigid body robot. The tip coordinates are X and Y, which can be calculated by the rigid body robot equivalent as shown by Equations 6.6 and 6.7.

$$X = L_2 sin(\theta_1) + L_3 sin(\theta_1 + \theta_2) \tag{6.6}$$

$$Y = L_1 + L_2 cos(\theta_1) + L_3 cos(\theta_1 + \theta_2) \tag{6.7}$$

where L_1 to L_3 are found using

$$L_1 = L_1^{'} + L_1^{''} \tag{6.8}$$

$$L_2 = L_1^{''} + L_2^{'} + L_2^{''} \tag{6.9}$$

and

$$L_3 = L_3^{'} + L_2^{''} \tag{6.10}$$

The lengths $L_i^{''}$ vary with angle and are found using

$$L_i^{''} = tan(\frac{\theta_i}{2})(\frac{L_i}{\theta_i} + \frac{h}{2}) \tag{6.11}$$

where h is the outer radius of the soft joint.

The model developed by Polygerinos et al. [109] was used to predict the joint angle θ at a pressure (P). From that model, the pressure required to reach a bending angle θ is

$$P = \frac{6M_\theta(\theta)}{4a^3 + 3\pi a^2 b} \tag{6.12}$$

where the bending moment M_θ is

$$M_\theta = \int_0^b s_\beta .2(a+t)L\beta d\beta + 2\int_0^t (\int_0^{\frac{\pi}{2}} s_{\tau,\phi}((a+\tau)^2 sin(\phi) + b(a+\tau))Ld\phi)d\tau \tag{6.13}$$

The longitudinal stretch (λ) and stress (s) of the top (β) and bottom (τ) layers are

$$\lambda_\beta = \frac{\beta\theta}{L} + 1 \tag{6.14}$$

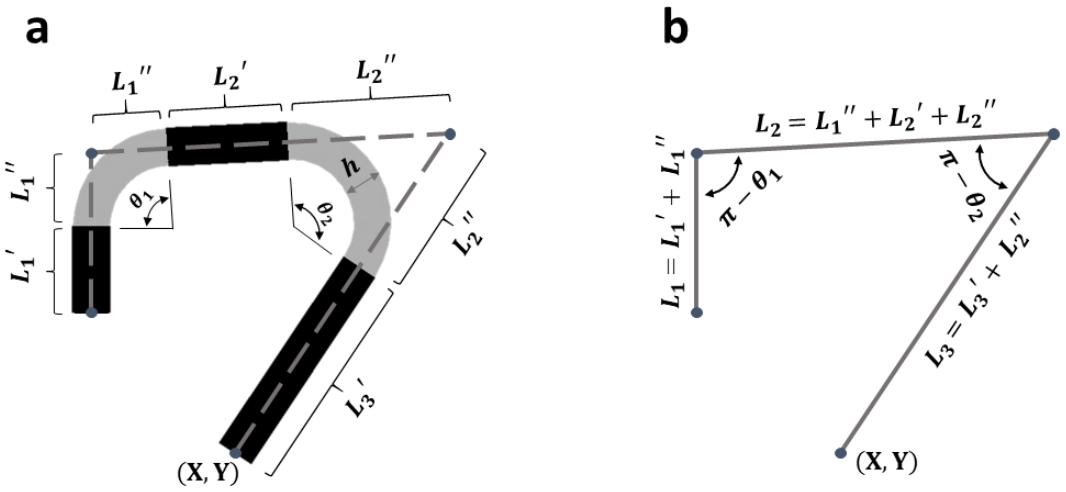

Figure 6.6: (a) Geometry for a 3-bone bending soft robot. (b) Equivalent rigid body structure for a 3-bone bending soft robot.

$$s_\beta = \bar{\mu}(\lambda_\beta - \frac{1}{\lambda_\beta^3}) \tag{6.15}$$

$$\lambda_{\tau,\phi} = \frac{R + b + sin(\phi)(a + \tau)}{R} \tag{6.16}$$

$$s_{\tau,\phi} = \bar{\mu}(\lambda_{\tau,\phi} - \frac{1}{\lambda_{\tau,\phi}^3}) \tag{6.17}$$

where t is the thickness of the top surface, b is the thickness of the bottom, and a is the cross-sectional radius of the semicircular finger. The coefficient $\bar{\mu}$ depends on material properties and wrapping geometry, including pitch and wrap angle, and was found through calibration. Equations 6.12 to 6.17 must be solved numerically to find the bending angle at each pressure since there is no closed-form solution for the integral in Equation 6.13. Constant curvature was assumed for the trajectory model.

6.3 Results

6.3.1 Bone-Inspired soft robot performance

Figure 6.7 shows the experimental frequency response of four bending soft robots using water and air as the working fluid. Figure 6.7a illustrates the frequency response of bone-inspired soft robots using water and air. Figure 6.7b compares the experimental frequency response of a bone-inspired soft robot to a traditional boneless soft robot. Experimental phase angle responses are shown in Figure 6.7c, indicating that embedding bones lead to higher damping and a lower phase shift compared to a soft robot without bones.

6.3.2 Stiffness and natural frequency model

Parameters α, α_M, β_M, and I in Equations 6.2 and 6.3 were identified using the least squares method based on the experimental data to be 120 (deg/mm), 4.58×10^{-5} $(1/g)$, 5.22×10^{-6} $(1/g)$, and 0.28 respectively. Figure 6.8a shows the natural frequency of four bending soft robots using water and air. It compares the results from experiment measurements with what was estimated by the natural frequency model, with model parameters identified above. Figure 6.8b shows the stiffness estimated from the model (Equation 6.2) for four bone-inspired soft robots with water and air as the working fluid.

6.3.3 Trajectory model

Figure 6.9 shows experiment and model data (Equations 6.12 to 6.17) for how angle varies with the working pressure for both joints of two 3-bone fingers. The trajectory model described above was fit to experimental results by sweeping $\bar{\mu}$ using the least squares method. Geometric parameters t, a, b, and T were measured using calipers. Parameters a, b, and T were measured to be 4.76 (mm), 4.6 (mm), and 12 (mm) for both fingers and t was 3.5 (mm) for (3B, LBF) finger and 3.7 (mm) for (3B, SBF) finger. Parameter $\bar{\mu}$ was estimated to be 58 and 53 kPa for the (3B, LBF) and (3B, SBF) fingers respectively.

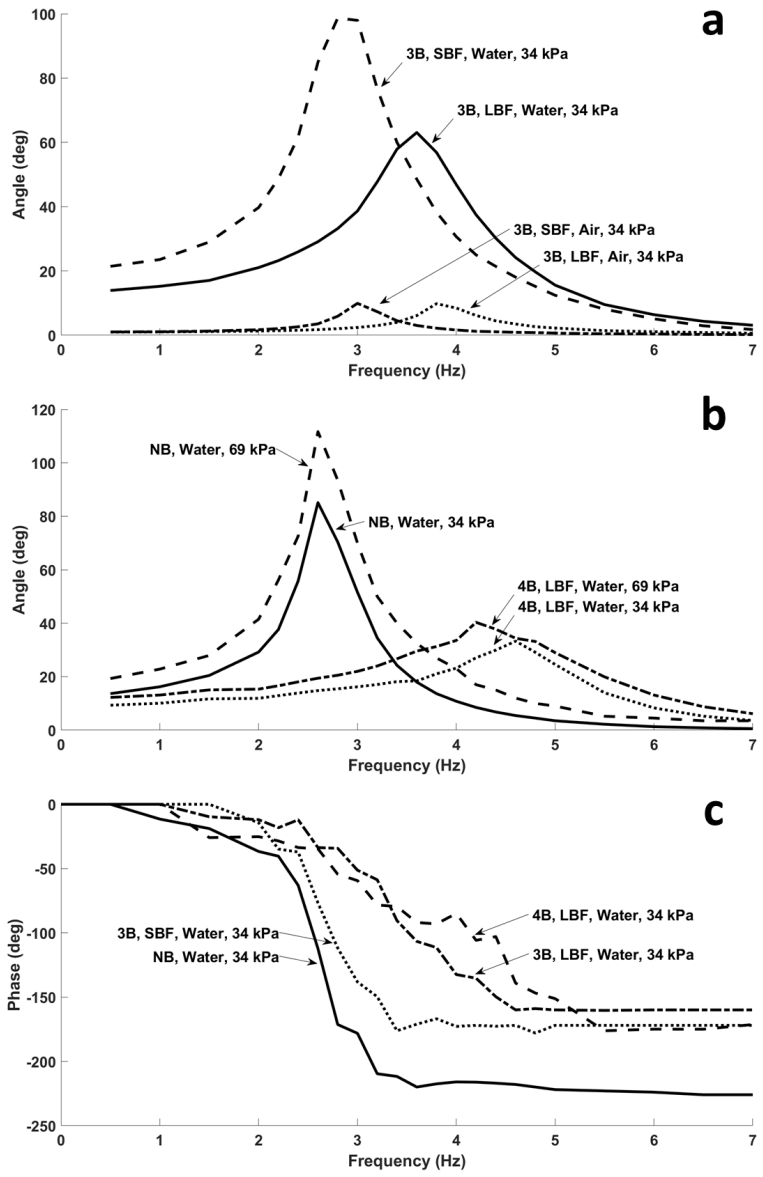

Figure 6.7: (a) Experimental frequency responses of two 3-bones long-bone-first (3B, LBF) and short-bone-first (3B, SBF) bending soft robots using water and air at 34 kPa. (b) Frequency response of a bending soft robot with no bone (NB) and a 4-bones long-bone-first (4B, LBF) bending soft robot using water at 34 and 69 kPa. (c) Phase responses of four bending soft robots (with no bones, 3-bones long-bone-first, 3-bones short-bone-first, and 4-bones long-bone-first) with water at 34 kPa. The data shows that bone-inspired fingers have higher natural frequencies.

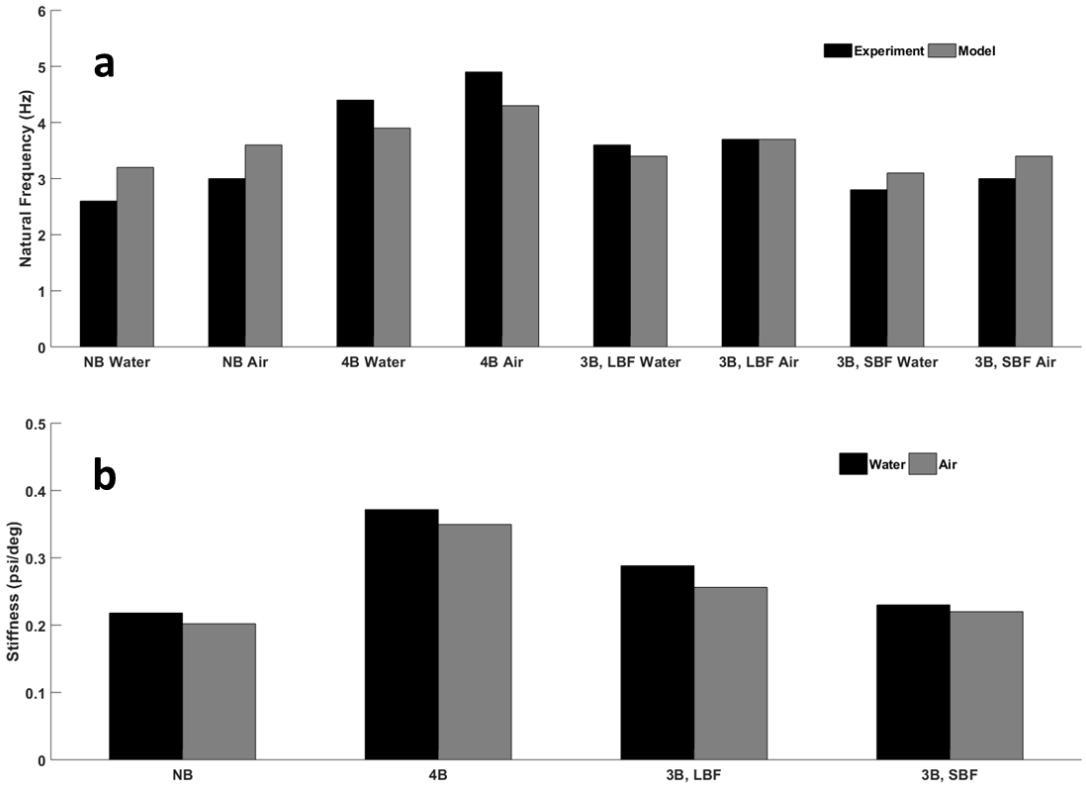

Figure 6.8: (a) Model and experimental natural frequency of four bending soft robots with water and air. (b) Estimated bending soft robots stiffness with water and air as calculated from the mass-spring-damper model. The data shows that bending soft robots with bones are stiffer.

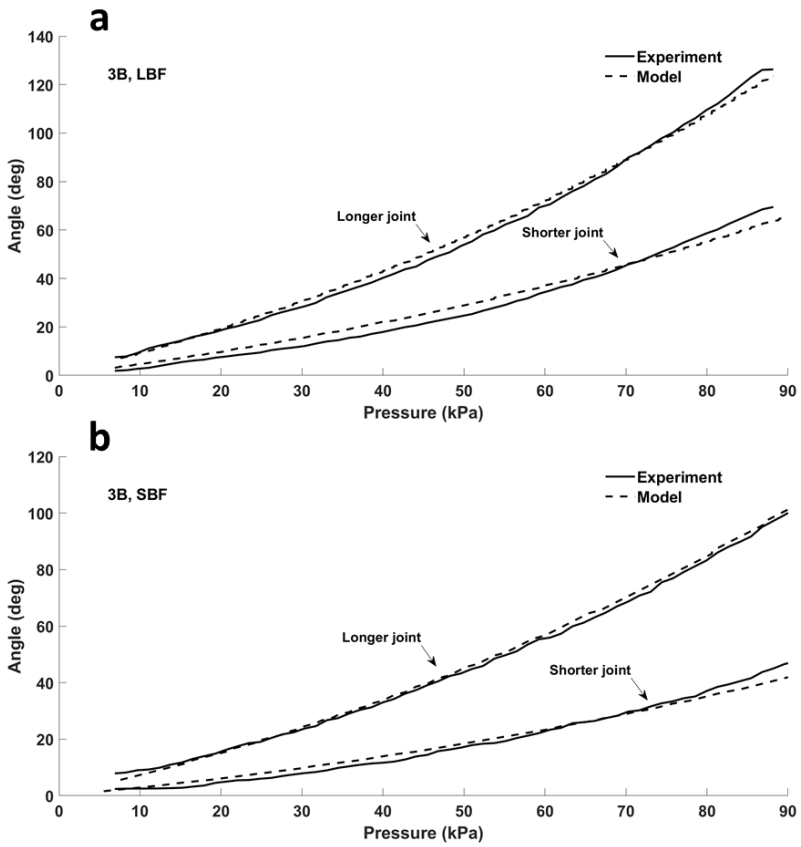

Figure 6.9: Model and experimental results for the angle of long and short soft joints in (a) 3-bones long-bone-first and (b) 3-bones short-bone-first bending soft robots.

Figure 6.10 shows the experimentally measured and model estimated (Equations 6.6 and 6.7) tip trajectories for two 3-bone soft robots for actuation pressures between 7 kPa and 90 kPa.

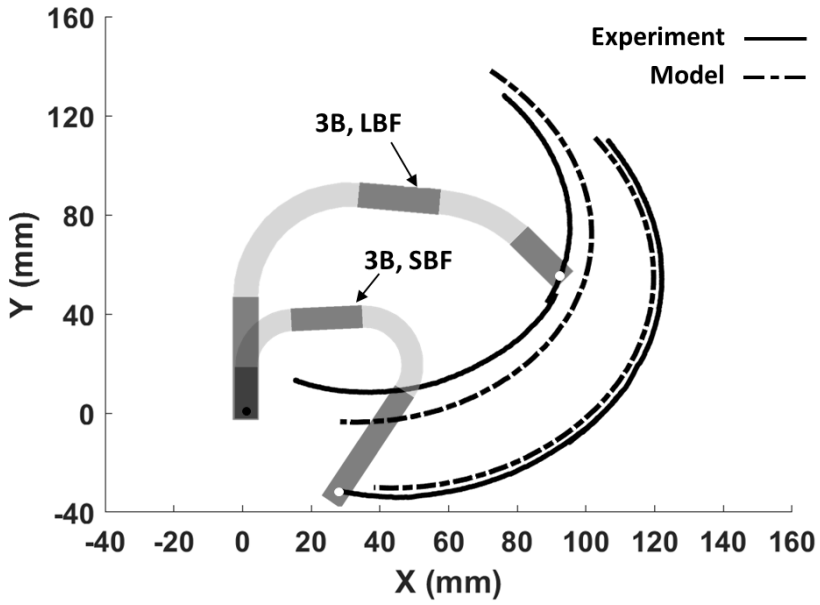

Figure 6.10: Predicted and experimental tip trajectory of a 3-bone long-bone-first and a 3-bone short-bone-first bending soft robot fingers.

6.4 Discussion

Figure 6.7a shows that the natural frequency is approximately the same for air and water. The water-driven fingers had a larger amplitude than the air-driven fingers due to the incompressibility of water. For this reason, water is a better choice than air for leader-follower applications such as puppeteering. In the simulation, keeping the mass of the water constant while changing the stiffness to the stiffness of the air changed the natural frequency by 2 percent. Likewise, keeping the stiffness of the water constant while changing the mass of the water to the mass of the air changed the natural frequency by 15 percent. Therefore, we conclude that the natural frequency of the overall system is dominated by the mass and stiffness of the materials used in the bone-inspired soft robot and not by the properties of the working fluid.

Figure 6.7b shows that the natural frequency of the robot with bones is higher, which means bone-inspired robots can respond more quickly to inputs. This figure also illustrates that the natural frequency is not affected by the preload pressure of the

working fluid as the natural frequency is about the same for 34 and 69 kPa preload pressures.

Figure 6.8 shows the the modeled and experimental natural frequencies and stiffness for different cases. The difference in natural frequency between the two ranges from 1 to 18 percent for all configurations. This difference is likely accounted for by manufacturing variations and the model assumptions, including the linearity of the stiffness.

The model results show that bending soft robots with bones are stiffer. The difference in finger stiffness when air and water were used shown in Figure 6.8b is less than 11 percent, validating the model shown in Figure 6.5. Manipulating the puppet also brought out another benefit of the bone-inspired architecture because the embedded bones almost eliminated undesired out-of-plane movement (Figure 6.11). Experiments must be conducted to determine key parameters to model any specific physical realization of a bone-inspired robot finger, which can certainly be done if the designer wishes to explore the performance of their bone-inspired finger through computer simulation. The main purpose of the stiffness and natural frequency model is not to show the performance of any particular bone-inspired robot finger but rather to reveal the major principles of the bending soft robots, which hold for all design variations.

The difference between $\bar{\mu}$ calculated from model and experiment shown in Figure 6.9 comes from the different thread wrapping angle and pitch that results from a hand fabrication process that did not have precise manufacturing quality control.

The path trajectory model holds for any physical realization since it only depends on the length of the segments and needs no experiments to set key parameters. Therefore the path stays the same for any actuation speed; however, the range of motion along the path does change with actuation frequency and with the properties of the elastomer as described in Equations 6.12 to 6.17. Figure 6.10 illustrates how the trajectory paths differ for the same sized bone-inspired fingers but with the order of the embedded bones reversed.

6.5 Conclusion

Adding the bones into the bending soft robots increases stiffness, damping, and controllability by increasing the natural frequency and decreasing the resonance peak and

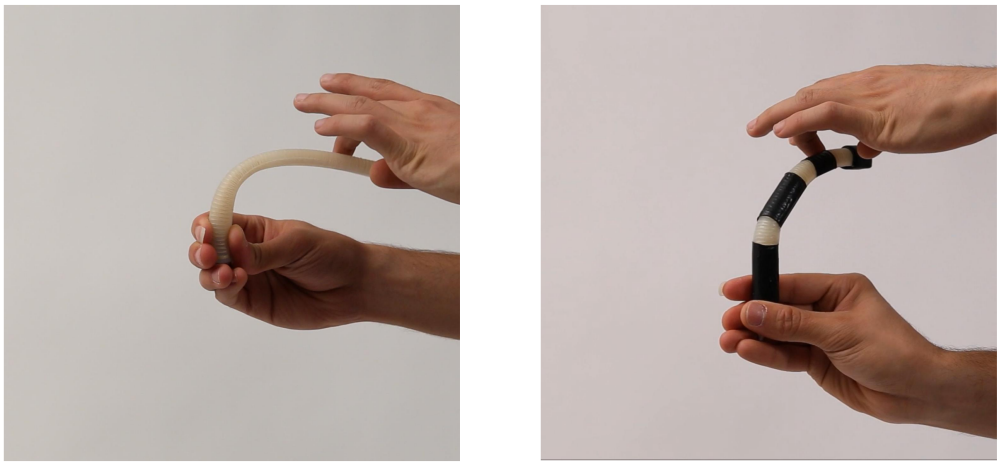

Figure 6.11: The embedded bones reduces the out-out-plane movements.

phase shift. Motion planning is achievable by embedding bones into the bending soft robots. Smooth actuation and sensible haptic feedback were achieved using a four-finger leader-follower puppet constructed using low-friction rolling diaphragm cylinders in the leader and bone-inspired bending robot fingers in the follower.

The dynamic performance of bending soft robots was the same for water and air as the working fluid; however, a higher response was seen for water, which means water is the preferred working fluid. The natural frequency did not change with the nominal pressure of the working fluid; however, a higher amplitude response was seen for higher pressures, which means the soft robot should be pre-pressurized to the highest feasible pressure.

A second-order mass-spring-damper system was used to model the cylinder-soft robot closed system. As with the experiments, the model showed the finger stiffness was similar using air or water. Further, the trajectory model could predict tip paths with reasonable accuracy. The models presented in this paper reveal the general principles of bone-inspired soft robots, and the trajectory model can be used to design any bone-inspired soft robot.

Chapter 7

Conclusion

The research studies conducted in this dissertation evaluated the concept of a low-friction and efficient variable hydraulic transmission to be used in wearable robots through analytical modeling and experimental validation. A variable hydraulic transmission can be used in any wearable and teleoperated embodiment, from rehabilitation and surgical robots to puppeteering and assistive robots. My contributions in this work are in three major areas:

1- To introduce efficient components and validate the performance through analytical modeling.

2- To present a variable hydraulic transmission with high performance and models to describe the multidisciplinary system.

3- To evaluate the performance of the soft robotic embodiment in a passive transmission through analytical modeling and experimental validation.

In chapter 1, a body-powered wearable robot (BPWR) was defined, and state-of-the-art in the wearable and BPWR was discussed. The applications of a variable hydraulic transmission were reviewed, and multiple examples of such embodiment were presented.

In chapter 2, the components required for a variable hydraulic transmission were proposed. Multiple research studies were conducted to provide a better perspective into the performance of actuators and valves. A manufacturing method for a long-stroke rolling diaphragm cylinder was presented. I reported volume and force performance evaluation on hydraulic actuators in this chapter. Consistent performance was achieved in the long-stroke rolling diaphragm cylinder with a 2 to 5 percent friction to load.

I reviewed all possible valve architectures for the system and proposed an analytical model to predict the valve friction in actuation. The model was used to find a valve embodiment with low pressure drop, fast response time, and low switching required energy. A proposed valve design was described in this chapter to be used in the variable hydraulic transmission testbed.

In chapter 3, the proposed actuators were used in an antagonist hydraulic transmission. I introduced a design with a long range of motion and high torque capability using long-stroke rolling diaphragm cylinders. Performance evaluation tests were conducted on friction, stiffness, tracking capability, etc. Results demonstrated the importance of the preload pressure in the system. The impulse time delay decreased, and the stiffness and transmitted power were increased significantly by increasing the preload pressure from 70 to 275 kPa.

In chapter 4, a variable hydraulic transmission design was proposed with 14 unique transmission ratios. The number of unique transmission ratios can increase to 67 by adding another pair of cylinders to the output with the same design. I conducted multiple performance evaluation tests on the system, and less than 3 percent of error was found in position transmission. The acceleration bump at the input and output was controlled by sequencing the valve actuation. Adequate haptic performance was reported for multiple transmission ratios.

In chapter 5, the variable hydraulic transmission was modeled to provide a system-level perspective. I used a hydraulic analogy to model the hydraulic friction through the system for multiple transmission ratios and configurations. The velocity dependency of the system and solutions to decrease that were discussed in this chapter. A superposition method of mechanical friction and hydraulic friction was performed and validated with experimental tests.

In chapter 6, the output of an antagonist hydraulic transmission was replaced by a bending soft robot. I introduced a bone-inspired bending soft robot to increase the stiffness and natural frequency of the traditional bending soft robots. I proposed a model to reveal the natural frequency and stiffness of bending soft robots and a geometrical model to predict the motion trajectory of the bone-inspired bending soft robots. I experimentally validated the dynamic and geometrical models and illustrated the similarity of the dynamic performance of the soft robots in a passive transmission in the case of using

air and water.

For future research, a new custom design for the valves needs to be explored deeply to provide zero pressure drop capability. This would eliminate the velocity dependency of the device to perform smoothly in any circumstances. An improvement in the design of the translational to rotary converting mechanism is necessary, and that would decrease the springiness of the joints and consequently the system's hysteresis. The haptic performance of the device at various transmission ratios needs to be investigated. The improvement in terms of the valve and actuation performance increases the haptic quality. Future research should include a comprehensive investigation of the valve sequence pattern to decrease the settling time and acceleration bump at the transmission switch. Furthermore, an exploration of the control theories in valve actuation would be helpful to allow a smoother transmission switch.

The wearability of this variable hydraulic transmission is another aspect that needs to be explored in the future. The small, lightweight, and conformal design of the actuators and the valve package are the two vital tasks for this purpose. The design for the rehabilitation robot can achieve both the clinical and take-home versions. The clinical evaluation of a wearable rehabilitation robot is also another area of interest for future work.

References

[1] N Yagn. Apparatus for facilitating walking, running, and jumping. 1890. *US Patent*, 420:179.

[2] Erico Guizzo and Harry Goldstein. The rise of the body bots [robotic exoskeletons]. *IEEE spectrum*, 42(10):50–56, 2005.

[3] Brett Neubauer and William Durfee. Preliminary design and engineering evaluation of a hydraulic ankle–foot orthosis. *Journal of Medical Devices*, 10(4), 2016.

[4] Adam B Zoss, Hami Kazerooni, and Andrew Chu. Biomechanical design of the berkeley lower extremity exoskeleton (bleex). *IEEE/ASME Transactions on mechatronics*, 11(2):128–138, 2006.

[5] John P Whitney, Tianyao Chen, John Mars, and Jessica K Hodgins. A hybrid hydrostatic transmission and human-safe haptic telepresence robot. In *2016 IEEE International Conference on Robotics and Automation (ICRA)*, pages 690–695. IEEE, 2016.

[6] Parker Seals. Parker o-ring handbook (ord 5700). *Parker Seal Group, Lexington, KY*, 1992.

[7] José L Pons. *Wearable robots: biomechatronic exoskeletons*. John Wiley & Sons, 2008.

[8] Hiroaki Kawamoto and Yoshiyuki Sankai. Power assist system hal-3 for gait disorder person. In *International Conference on Computers for Handicapped Persons*, pages 196–203. Springer, 2002.

[9] Hiroaki Kawamoto, Suwoong Lee, Shigehiro Kanbe, and Yoshiyuki Sankai. Power assist method for hal-3 using emg-based feedback controller. In *SMC'03 Conference Proceedings. 2003 IEEE International Conference on Systems, Man and Cybernetics. Conference Theme-System Security and Assurance (Cat. No. 03CH37483)*, volume 2, pages 1648–1653. IEEE, 2003.

[10] Aaron M Dollar and Hugh Herr. Lower extremity exoskeletons and active orthoses: Challenges and state-of-the-art. *IEEE Transactions on robotics*, 24(1):144–158, 2008.

[11] Brett C Neubauer, Jonathan Nath, and William K Durfee. Design of a portable hydraulic ankle-foot orthosis. In *2014 36th Annual International Conference of the IEEE Engineering in Medicine and Biology Society*, pages 1182–1185. IEEE, 2014.

[12] Wolf Schweitzer, Michael J Thali, and David Egger. Case-study of a user-driven prosthetic arm design: bionic hand versus customized body-powered technology in a highly demanding work environment. *Journal of neuroengineering and rehabilitation*, 15(1):1–27, 2018.

[13] John W Michael and John H Bowker. *Atlas of amputations and limb deficiencies: surgical, prosthetic, and rehabilitation principles.* American Academy of Orthopaedic Surgeons Rosemont, IL, 2004.

[14] Tariq Rahman, Whitney Sample, Rahamim Seliktar, Michael Alexander, and Mena Scavina. A body-powered functional upper limb orthosis. *Journal of rehabilitation research and development*, 37(6):675–680, 2000.

[15] Tariq Rahman and Sean Stroud. A body-powered rehabilitation robot. *Journal of Rehabilitation Research and Development*, 34:143, 1997.

[16] Darwin G Caldwell, Nikolaos G Tsagarakis, Sophia Kousidou, Nelson Costa, and Ioannis Sarakoglou. " soft" exoskeletons for upper and lower body rehabilitation—design, control and testing. *International Journal of Humanoid Robotics*, 4(03):549–573, 2007.

[17] SG Millstein, H Heger, and GA Hunter. Prosthetic use in adult upper limb amputees: a comparison of the body powered and electrically powered prostheses. *Prosthetics and orthotics international*, 10(1):27–34, 1986.

[18] Xun Luo, Tiffany Kline, Heidi C Fischer, Kathy A Stubblefield, Robert V Kenyon, and Derek G Kamper. Integration of augmented reality and assistive devices for post-stroke hand opening rehabilitation. In *2005 IEEE Engineering in Medicine and Biology 27th Annual Conference*, pages 6855–6858. IEEE, 2006.

[19] Stephanie L Carey, Derek J Lura, and M Jason Highsmith. Differences in myoelectric and body-powered upper-limb prostheses: Systematic literature review. *Journal of Rehabilitation Research & Development*, 52(3), 2015.

[20] Edward P Washabaugh, Emma Treadway, R Brent Gillespie, C David Remy, and Chandramouli Krishnan. Self-powered robots to reduce motor slacking during upper-extremity rehabilitation: a proof of concept study. *Restorative neurology and neuroscience*, 36(6):693–708, 2018.

[21] Yasuhisa Hirata, Zhi-dong Wang, and Kazuhiro Kosuge. Human-robot interaction based on passive robotics. In *2006 SICE-ICASE International Joint Conference*, pages 4206–4209. IEEE, 2006.

[22] Weiguang Huo, Samer Mohammed, Juan C Moreno, and Yacine Amirat. Lower limb wearable robots for assistance and rehabilitation: A state of the art. *IEEE systems Journal*, 10(3):1068–1081, 2014.

[23] Yi Long, Zhi-jiang Du, Wei-dong Wang, Long He, Xi-wang Mao, and Wei Dong. Physical human-robot interaction estimation based control scheme for a hydraulically actuated exoskeleton designed for power amplification. *Frontiers of Information Technology & Electronic Engineering*, 19(9):1076–1085, 2018.

[24] Xue Zhang, Zan Yue, and Jing Wang. Robotics in lower-limb rehabilitation after stroke. *Behavioural neurology*, 2017, 2017.

[25] Feng Zhang, Pengfeng Li, Zeng-Guang Hou, Zhen Lu, Yixiong Chen, Qingling Li, and Min Tan. semg-based continuous estimation of joint angles of human legs by using bp neural network. *Neurocomputing*, 78(1):139–148, 2012.

[26] Ho Shing Lo and Sheng Quan Xie. Exoskeleton robots for upper-limb rehabilitation: State of the art and future prospects. *Medical engineering & physics*, 34(3):261–268, 2012.

[27] Susan Karlin. Raiding iron man's closet [geek life]. *IEEE Spectrum*, 48(8):25–25, 2011.

[28] José González-Vargas, Jaime Ibáñez, Jose L Contreras-Vidal, Herman Van der Kooij, and José Luis Pons. *Wearable Robotics: Challenges and Trends: Proceedings of the 2nd International Symposium on Wearable Robotics, WeRob2016, October 18-21, 2016, Segovia, Spain*, volume 16. Springer, 2016.

[29] Kurt Amundson, Justin Raade, Nathan Harding, and Hami Kazerooni. Hybrid hydraulic-electric power unit for field and service robots. In *2005 IEEE/RSJ International Conference on Intelligent Robots and Systems*, pages 3453–3458. IEEE, 2005.

[30] H Kazerooni and R Steger. The berkeley lower extremity exoskeleton. pages 14–25, 2006.

[31] Cyrus Raoufi, Andrew A Goldenberg, and Walter Kucharczyk. A new hydraulically/pneumatically actuated mr-compatible robot for mri-guided neurosurgery. In *2008 2nd International Conference on Bioinformatics and Biomedical Engineering*, pages 2232–2235. IEEE, 2008.

[32] Roland Moser, Roger Gassert, Etienne Burdet, Laurent Sache, HR Woodtli, J Erni, Willy Maeder, and Hannes Bleuler. An mr compatible robot technology. In *2003 IEEE International Conference on Robotics and Automation (Cat. No. 03CH37422)*, volume 1, pages 670–675. IEEE, 2003.

[33] Ziyan Guo, Ziyang Dong, Kit-Hang Lee, Chim Lee Cheung, Hing-Choi Fu, Justin DL Ho, Haokun He, Wai-Sang Poon, Danny Tat-Ming Chan, and Ka-Wai Kwok. Compact design of a hydraulic driving robot for intraoperative mri-guided bilateral stereotactic neurosurgery. *IEEE Robotics and Automation Letters*, 3(3):2515–2522, 2018.

[34] Roger Gassert, Roland Moser, Etienne Burdet, and Hannes Bleuler. Mri/fmri-compatible robotic system with force feedback for interaction with human motion. *IEEE/ASME transactions on mechatronics*, 11(2):216–224, 2006.

[35] Mingyen Ho, Yeongjin Kim, Shing Shin Cheng, Rao Gullapalli, and Jaydev P Desai. Design, development, and evaluation of an mri-guided sma spring-actuated neurosurgical robot. *The International journal of robotics research*, 34(8):1147–1163, 2015.

[36] Kit-Hang Lee, Kin Chung Denny Fu, Ziyan Guo, Ziyang Dong, Martin CW Leong, Chim-Lee Cheung, Alex Pui-Wai Lee, Wayne Luk, and Ka-Wai Kwok. Mr safe robotic manipulator for mri-guided intracardiac catheterization. *IEEE/ASME Transactions on Mechatronics*, 23(2):586–595, 2018.

[37] Bo Yang, U-Xuan Tan, Alan B McMillan, Rao Gullapalli, and Jaydev P Desai. Design and control of a 1-dof mri-compatible pneumatically actuated robot with long transmission lines. *IEEE/ASME transactions on mechatronics*, 16(6):1040–1048, 2010.

[38] Ningbo Yu, Christoph Hollnagel, Armin Blickenstorfer, Spyros S Kollias, and Robert Riener. Comparison of mri-compatible mechatronic systems with hydrodynamic and pneumatic actuation. *IEEE/ASME transactions on mechatronics*, 13(3):268–277, 2008.

[39] Jing Dai, Zhuoliang He, Ge Fang, Xiaomei Wang, Yingqi Li, Chim-Lee Cheung, Liyuan Liang, Iulian Iordachita, Hing-Chiu Chang, and Ka-Wai Kwok. A robotic platform to navigate mri-guided focused ultrasound system. *IEEE Robotics and Automation Letters*, 6(3):5137–5144, 2021.

[40] Evelyn Mendoza and John Peter Whitney. A testbed for haptic and magnetic resonance imaging-guided percutaneous needle biopsy. *IEEE Robotics and Automation Letters*, 4(4):3177–3183, 2019.

[41] Natalie Burkhard, Samuel Frishman, Alexander Gruebele, J Peter Whitney, Roger Goldman, Bruce Daniel, and Mark Cutkosky. A rolling-diaphragm hydrostatic

transmission for remote mr-guided needle insertion. In *2017 IEEE international conference on robotics and automation (ICRA)*, pages 1148–1153. IEEE, 2017.

[42] Homayoon Kazerooni. Extender: a case study for human-robot interaction via transfer of power and information signals. In *Proceedings of 1993 2nd IEEE International Workshop on Robot and Human Communication*, pages 10–20. IEEE, 1993.

[43] Craig Causer. Disney tech: Immersive storytelling through innovation. *IEEE Potentials*, 38(5):10–18, 2019.

[44] Nicolas Badeau, Clément Gosselin, Simon Foucault, Thierry Laliberté, and Muhammad E Abdallah. Intuitive physical human-robot interaction: Using a passive parallel mechanism. *IEEE Robotics & Automation Magazine*, 25(2):28–38, 2018.

[45] Marc-Antoine Lacasse, Genevieve Lachance, Julien Boisclair, Jérémie Ouellet, and Clément Gosselin. On the design of a statically balanced serial robot using remote counterweights. In *2013 IEEE International Conference on Robotics and Automation*, pages 4189–4194. IEEE, 2013.

[46] Apurba Das and M Nabi. A review on soft robotics: Modeling, control and applications in human-robot interaction. In *2019 International Conference on Computing, Communication, and Intelligent Systems (ICCCIS)*, pages 306–311. IEEE, 2019.

[47] Jicheng Xia and William K Durfee. Experimentally validated models of o-ring seals for tiny hydraulic cylinders. In *ASME/BATH 2014 Symposium on Fluid Power and Motion Control*. American Society of Mechanical Engineers Digital Collection, 2014.

[48] Emma Treadway, Zhenyu Gan, C David Remy, and R Brent Gillespie. Toward controllable hydraulic coupling of joints in a wearable robot. *IEEE Transactions on Robotics*, 34(3):748–763, 2018.

[49] Emma Lea Treadway. *Perception, analysis, and control of parasitic effects in active and passive physical human-robot interaction.* PhD thesis, 2019.

[50] John P Whitney, Matthew F Glisson, Eric L Brockmeyer, and Jessica K Hodgins. A low-friction passive fluid transmission and fluid-tendon soft actuator. In *2014 IEEE/RSJ International Conference on Intelligent Robots and Systems*, pages 2801–2808. IEEE, 2014.

[51] Michael B Binnard. *Design of a small pneumatic walking robot*. PhD thesis, Massachusetts Institute of Technology, 1995.

[52] Alexander Gruebele, Samuel Frishman, and Mark R Cutkosky. Long-stroke rolling diaphragm actuators for haptic display of forces in teleoperation. *IEEE Robotics and Automation Letters*, 4(2):1478–1484, 2019.

[53] Bellofram rolling diaphragm design manual (2009). `http://www.atcdiversified.com/Diaphragm/PDF/design_manual.pdf`.

[54] Malcolm J McPherson. Introduction of fluid mechanics. In *Subsurface Ventilation and Environmental Engineering*, pages 15–49. Springer, 1993.

[55] James M McDonough. Lectures in elementary fluid dynamics: physics, mathematics and applications. 2009.

[56] Matti Linjama et al. Digital fluid power: State of the art. In *Proceedings of The Twelfth Scandinavian International Conference on Fluid Power, Tampere, Finland*, 2011.

[57] Rudolf Scheidl, Matti Linjama, and Stefan Schmidt. Is the future of fluid power digital? *Proceedings of the Institution of Mechanical Engineers, Part I: Journal of Systems and Control Engineering*, 226(6):721–723, 2012.

[58] Zhenyu Gan, Katelyn Fry, R Brent Gillespie, and C David Remy. A novel variable transmission with digital hydraulics. In *2015 IEEE/RSJ International Conference on Intelligent Robots and Systems (IROS)*, pages 5838–5843. IEEE, 2015.

[59] Shinichi YOKOTA and Kotarou AKUTU. A fast-acting electro-hydraulic digital transducer: a poppet-type on-off valve using a multilayered piezoelectric device. *JSME international journal. Ser. 2, Fluids engineering, heat transfer, power, combustion, thermophysical properties*, 34(4):489–495, 1991.

[60] Riccardo Amirante, Giuseppe Del Vescovo, and Antonio Lippolis. Flow forces analysis of an open center hydraulic directional control valve sliding spool. *Energy Conversion and Management*, 47(1):114–131, 2006.

[61] Samir F Moujaes and Rayavarapu Jagan. 3d cfd predictions and experimental comparisons of pressure drop in a ball valve at different partial openings in turbulent flow. *Journal of Energy Engineering*, 134(1):24–28, 2008.

[62] Arthur Akers, Max Gassman, and Richard Smith. *Hydraulic power system analysis*. CRC press, 2006.

[63] H Uehleke and T Werner. Flow of fluids through valves, fittings, and pipe (tp-410 (us edition)). *Arch Toxicol*, 34:289–308, 1975.

[64] Faisal MM Al-Ghathian and Muafag S Tarawneh. Friction forces in o-ring sealing. *American Journal of Applied Sciences*, 2(3):626–632, 2005.

[65] Samuel M Felton, Dae-Young Lee, Kyu-Jin Cho, and Robert J Wood. A passive, origami-inspired, continuously variable transmission. In *2014 IEEE International Conference on Robotics and Automation (ICRA)*, pages 2913–2918. IEEE, 2014.

[66] K Koyanagi, Yasuhiro Kakinuma, H Anzai, K Sakurai, and T Oshima. Stabilizing output of an electrorheological gel linear actuator. *Journal of intelligent material systems and structures*, 22(15):1685–1692, 2011.

[67] Matti Linjama, Hannu-Pecka Vihtanen, Ari Sipola, and Matti Vilenius. Secondary controlled multi-chamber hydraulic cylinder. In *The 11th Scandinavian International Conference on Fluid Power, SICFP*, volume 9, pages 2–4, 2009.

[68] Saeed Hashemi, Steven Sobojinski, and William K Durfee. Low-friction antagonist hydraulic transmission using long-stroke rolling diaphragm cylinders. In *ASME/BATH 2017 Symposium on Fluid Power and Motion Control (pp. V001T01A073-V001T01A073). American Society of Mechanical Engineers*, 2017.

[69] B Stojanović, L Ivanović, and M Blagojević. friction and wear in timing belt drives. *Tribology in industry*, 32(3):33–40, 2010.

[70] EE Klaus and JA O'brien. Precise measurement and prediction of bulk-modulus values for fluids and lubricants. 1964.

[71] B Bonsen, TWGL Klaassen, KGO Van de Meerakker, M Steinbuch, and PA Veenhuizen. Analysis of slip in a continuously variable transmission. In *ASME International Mechanical Engineering Congress and Exposition*, volume 37130, pages 995–1000, 2003.

[72] Minh Tri Nguyen, Tri Dung Dang, and Kyoung Kwan Ahn. Application of electro-hydraulic actuator system to control continuously variable transmission in wind energy converter. *Energies*, 12(13):2499, 2019.

[73] Jianjun Hu, Bo Mei, Hang Peng, and Zihan Guo. Discretely variable speed ratio control strategy for continuously variable transmission system considering hydraulic energy loss. *Energy*, 180:714–727, 2019.

[74] Micklem Guebeli, JD Micklem, and CR Burrows. Maximum transmission efficiency of a steel belt continuously variable transmission. In *International Design Engineering Technical Conferences and Computers and Information in Engineering Conference*, volume 9372, pages 329–334. American Society of Mechanical Engineers, 1992.

[75] Song Jinchun and Wang Changzhou. Modeling and simulation of hydraulic control system for vehicle continuously variable transmission. In *2008 3rd IEEE Conference on Industrial Electronics and Applications*, pages 799–803. IEEE, 2008.

[76] Rico H Hansen, Morten M Kramer, and Enrique Vidal. Discrete displacement hydraulic power take-off system for the wavestar wave energy converter. *Energies*, 6(8):4001–4044, 2013.

[77] GS Payne, AE Kiprakis, M Ehsan, W H S Rampen, JP Chick, and AR Wallace. Efficiency and dynamic performance of digital displacement$^{\text{TM}}$ hydraulic transmission in tidal current energy converters. *Proceedings of the Institution of Mechanical Engineers, Part A: Journal of Power and Energy*, 221(2):207–218, 2007.

[78] John J Pippenger and Tyler G Hicks. *Industrial hydraulics*. 1979.

[79] Trevor M Hunt, T Hunt, ND Vaughan, and N Vaughan. *The hydraulic handbook*. Elsevier, 1996.

[80] Jicheng Xia and William K Durfee. Analysis of small-scale hydraulic actuation systems. *Journal of mechanical design*, 135(9), 2013.

[81] Herbert E Merritt and Victor Pomper. Hydraulic control systems. *Journal of Applied Mechanics*, 35(1):200, 1968.

[82] ND Manring and Greg R Luecke. Modeling and designing a hydrostatic transmission with a fixed-displacement motor. 1998.

[83] Karl-Erik Rydberg. *On performance optimization and digital control of hydrostatic drives for vehicle applications*. Number Monograph. 1983.

[84] Triet Hung Ho and Kyoung Kwan Ahn. Modeling and simulation of hydrostatic transmission system with energy regeneration using hydraulic accumulator. *Journal of mechanical science and technology*, 24(5):1163–1175, 2010.

[85] Stanley H Chan, Ramsin Khoshabeh, Kristofor B Gibson, Philip E Gill, and Truong Q Nguyen. An augmented lagrangian method for total variation video restoration. *IEEE Transactions on Image Processing*, 20(11):3097–3111, 2011.

[86] Bjørn Skaare, Bo Hörnsten, and Finn Gunnar Nielsen. Modeling, simulation and control of a wind turbine with a hydraulic transmission system. *Wind Energy*, 16(8):1259–1276, 2013.

[87] Yajun Fan, Anle Mu, and Tao Ma. Study on the application of energy storage system in offshore wind turbine with hydraulic transmission. *Energy Conversion and Management*, 110:338–346, 2016.

[88] Esfandiar Shafai, Michael Simons, Ulrich Neff, and Hans P Geering. Model of a continuously variable transmission. In *Advances in Automotive Control 1995*, pages 105–113. Elsevier, 1995.

[89] Yunfeng Liu, Yunshan Zhou, Jiande Wang, Daohai Qu, and Feitie Zhang. Hydraulic system control for a hybrid continuously variable transmission based on an electric oil pump. *IEEE Transactions on Vehicular Technology*, 67(11):10398–10410, 2018.

[90] Zhenyu Gan, Haoyue Tang, Emma Treadway, Richard Brent Gillespie, and Christian David Remy. Modeling and experimental evaluation of a variable hydraulic transmission. *IEEE/ASME Transactions on Mechatronics*, 25(2):750–761, 2020.

[91] Xuan Bo Tran, Nur Hafizah, and Hideki Yanada. Modeling of dynamic friction behaviors of hydraulic cylinders. *Mechatronics*, 22(1):65–75, 2012.

[92] Jun-hui Zhang, Di Wang, Bing Xu, Min-yao Gan, Min Pan, and Hua-yong Yang. Experimental and numerical investigation of flow forces in a seat valve using a damping sleeve with orifices. *Journal of Zhejiang University-SCIENCE A*, 19(6):417–430, 2018.

[93] Matti Linjama and Matti Vilenius. Digital hydraulics. *Tampere University of Technology (TUT), Department of Intelligent Hydraulics and Automation (IHA)*, 2008.

[94] A Esposito. A simplified method for analyzing hydraulic circuits by analogy. *Machine Design*, 41(24):173, 1969.

[95] PE E Shashi Menon. *Piping calculations manual*. McGraw-Hill Education, 2005.

[96] Brian Silowash. *Piping systems manual*. McGraw Hill Professional, 2009.

[97] Crane Co. *Flow of fluids through valves, fittings, and pipe*. Number 410. Crane Company, 1988.

[98] Daniela Rus and Michael T Tolley. Design, fabrication and control of soft robots. *Nature.*, 521(7553):467, 2015.

[99] William R Ferrell. Remote manipulation with transmission delay. *IEEE Transactions on Human Factors in Electronics.*, (1):24–32, 1965.

[100] Raphael Deimel, Marcel Radke, and Oliver Brock. Mass control of pneumatic soft continuum actuators with commodity components. In *2016 IEEE/RSJ International Conference on Intelligent Robots and Systems (IROS)*, pages 774–779. IEEE, 2016.

[101] Manuel G Catalano, Giorgio Grioli, Edoardo Farnioli, Alessandro Serio, Cristina Piazza, and Antonio Bicchi. Adaptive synergies for the design and control of the pisa/iit softhand. *The International Journal of Robotics Research.*, 33(5):768–782, 2014.

[102] Zhe Xu and Emanuel Todorov. Design of a highly biomimetic anthropomorphic robotic hand towards artificial limb regeneration. In *2016 IEEE International Conference on Robotics and Automation (ICRA)*, pages 3485–3492. IEEE, 2016.

[103] Ronan Hinchet, Velko Vechev, Herbert Shea, and Otmar Hilliges. Dextres: Wearable haptic feedback for grasping in vr via a thin form-factor electrostatic brake. In *The 31st Annual ACM Symposium on User Interface Software and Technology*, pages 901–912. ACM, 2018.

[104] Darwin G Caldwell, Gustavo A Medrano-Cerda, and Mike Goodwin. Control of pneumatic muscle actuators. *IEEE Control Systems Magazine.*, 15(1):40–48, 1995.

[105] Panagiotis Polygerinos, Zheng Wang, Kevin C Galloway, Robert J Wood, and Conor J Walsh. Soft robotic glove for combined assistance and at-home rehabilitation. *Robotics and Autonomous Systems*, 73:135–143, 2015.

[106] Panagiotis Polygerinos, Kevin C Galloway, Emily Savage, Maxwell Herman, Kathleen O'Donnell, and Conor J Walsh. Soft robotic glove for hand rehabilitation and task specific training. In *2015 IEEE international conference on robotics and automation (ICRA)*, pages 2913–2919. IEEE, 2015.

[107] Erika Rogers. Human-robot interaction. *Berkshire Encyclopedia of Human-Computer Interaction.*, page 328, 2004.

[108] Dónal P Holland, Evelyn J Park, Panagiotis Polygerinos, Gareth J Bennett, and Conor J Walsh. The soft robotics toolkit: Shared resources for research and design. *Soft Robotics.*, 1(3):224–230, 2014.

[109] Panagiotis Polygerinos, Zheng Wang, Johannes TB Overvelde, Kevin C Galloway, Robert J Wood, Katia Bertoldi, and Conor J Walsh. Modeling of soft fiber-reinforced bending actuators. *IEEE Transactions on Robotics.*, 31(3):778–789, 2015.

[110] Kevin C Galloway, Panagiotis Polygerinos, Conor J Walsh, and Robert J Wood. Mechanically programmable bend radius for fiber-reinforced soft actuators. In *2013 16th International Conference on Advanced Robotics (ICAR)*, pages 1–6. IEEE, 2013.

[111] Mark Gilbertson, Darrin Beekman, Biswaranjan Mohanty, Saeed Hashemi, Sangyoon Lee, James D Van de Ven, and Timothy M Kowalewski. Force analysis and modelling of soft actuators for catheter robots. In *ASME 2016 Dynamic Systems and Control Conference*. American Society of Mechanical Engineers Digital Collection, 2017.

[112] A Hošovskỳ, J Pitel', K Židek, M Tóthová, J Sárosi, and L Cveticanin. Dynamic characterization and simulation of two-link soft robot arm with pneumatic muscles. *Mechanism and Machine Theory.*, 103:98–116, 2016.

[113] Z Ge Joey, Ariel A Calderón, and Néstor O Pérez-Arancibia. An earthworm-inspired soft crawling robot controlled by friction. In *2017 IEEE International Conference on Robotics and Biomimetics (ROBIO)*, pages 834–841. IEEE, 2017.

[114] ELANGO Natarajan, Mohd Faudzi, Ahmad Athif, Viknesh Malliga Jeevanantham, Muhammad Razif, Muhammad Rusydi, Mohd Nordin, and Ili Najaa Aimi. Numerical dynamic analysis of a single link soft robot finger. In *Applied Mechanics and Materials*, volume 459, pages 449–454. Trans Tech Publ, 2014.

[115] Fionnuala Connolly, Conor J Walsh, and Katia Bertoldi. Automatic design of fiber-reinforced soft actuators for trajectory matching. *Proceedings of the National Academy of Sciences.*, 114(1):51–56, 2017.